EFFECT OF SILVER NANOPARTICLE COATINGS ON MYCOBACTERIAL BIOFILM ATTACHMENT AND GROWTH: IMPLICATIONS FOR CERAMIC WATER FILTERS

by

Curtis James Larimer

BS in Engineering Physics, University of Pittsburgh, 2008

Submitted to the graduate faculty of

Swanson School of Engineering in partial fulfillment

of the requirements for the degree of

Doctor of Philosophy

University of Pittsburgh

2013

UNIVERSITY OF PITTSBURGH
SWANSON SCHOOL OF ENGINEERING

This dissertation was presented

by

Curtis James Larimer

It was defended on
July 19th, 2013

and approved by

John Barnard, Ph.D., Professor, Department of Mechanical Engineering and Materials Science
Jung-Kun Lee, Ph.D., Assistant Professor, Department of Mechanical Engineering and Materials Science
Judith Yang, Ph.D., Professor, Department of Chemical and Petroleum Engineering
Qing Ming Wang, Ph.D., Professor, Department of Mechanical Engineering and Materials Science
Dissertation Director: Ian Nettleship, Ph.D., Associate Professor, Department of Mechanical Engineering and Materials Science

EFFECT OF SILVER NANOPARTICLE COATINGS ON MYCOBACTERIAL BIOFILM ATTACHMENT AND GROWTH: IMPLICATIONS FOR CERAMIC WATER FILTERS

Curtis James Larimer, PhD

University of Pittsburgh, 2013

Silver is a natural, broad-spectrum antibacterial metal and its toxicity can be enhanced when surface area is maximized. As a result, silver nanoparticles (AgNP) have been investigated for use in novel water treatment technologies. The hypothesis of this work is that deposited AgNPs can enhance water treatment technologies by inhibiting growth of planktonic bacteria and biofilms. This was investigated by evaluating the antibacterial efficacy of AgNPs both in solution and as deposited on surfaces. AgNPs were found to be toxic to three species of environmental mycobacteria, *M. smegmatis*, *M. avium*, and *M. marinum* and the level of susceptibility varied widely, probably owing to the varying levels of silver that each species is exposed to in its natural environment. When cultured in a AgNP enriched environment *M. smegmatis* developed resistance to the toxic effects of both the nanoparticles and silver ions. The resistant mutant was as viable as the unmodified strain and was also resistant to antibiotic isoniazid. However, the strain was more susceptible to other toxic metal ions from $ZnSO_4$ and $CuSO_4$.

AgNPs were deposited on silicon wafer substrates by vertical colloidal deposition (VCD). Manipulating deposition speed and also concentration of AgNPs in the depositing liquid led to a

range of AgNP coatings with distinctive deposition lines perpendicular to the motion of the meniscus. Experimental results for areal coverage, which was measured from SEM images of AgNP coatings, were compared to Diao's theory of VCD but did not show agreement due to a stick-slip mechanism that is not accounted for by the theory. Durability of AgNP coatings is critical for antibacterial efficacy and to mitigate the risks of exposing the environment to nanomaterials and it was measured by exposing AgNP coatings to liquid flow in a flow cell. Durability was improved by modifying processing to include a heat treatment after deposition.

Finally, the antibiofilm efficacy of deposited AgNPs was demonstrated by culturing *M. smegmatis* on porous membrane filters and Si substrates that were coated with AgNP. In both cases AgNP inhibited biofilm growth with an effect that was concentration or areal coverage dependent.

TABLE OF CONTENTS

LIST OF TABLES

LIST OF FIGURES

1.0 INTRODUCTION

And I wish to give an account of the other kinds of waters, namely, of such as are wholesome and such as are unwholesome, and what bad and what good effects may be derived from water; for water contributes much towards health.

–Hippocrates. From *On Airs, Waters and Places*, ca. 450 BC [1]

The importance of water to human health has been known for more than two millennia. Hippocrates, the "father of modern medicine," recognized the effects of water and only used clean water or wine to treat his patients [1]. More than two thousand years passed until Dr. John Snow identified a single water pump on Broad Street in London as the cause of a deadly cholera outbreak in 1854. Although he recognized the disease as waterborne and pioneered the field of epidemiology in the process, another two decades passed until Dr. Robert Koch identified the "invisible killer" as a bacillus of cholera bacteria through microscopic examination [2]. Since that era great advances have been made in medicine, the technology of disease prevention, and water treatment, but cholera still causes 100,000 – 130,000 deaths per year as of 2010 [3].

Coincidentally, Hippocrates also foresaw the beneficial and anti-disease properties of silver. He recommended treating ulcers by sprinkling them with "the flowers of silver alone, in the finest powder." Perhaps because Hippocrates lived in an era still skeptical of medicine or perhaps because of his somewhat inexact methods (he also recommended treating wounds with

lead) [1] the effect of silver on health has taken much longer to be understood scientifically. In fact, certain antibacterial and antiviral mechanisms of silver are still unexplained [4].

Recent developments in nanotechnology have reinvigorated interest in silver as an antibacterial in water treatment. The ability to make a powder of silver more fine than Hippocrates could have possibly imagined has once again made silver a popular alternative to antibiotics and other bactericides. Silver has been used to make drinking vessels and wash basins for centuries. However, the rarity of the noble metal made it a luxury of the privileged elite since at least the era of Hippocrates. Use of silver for water treatment would still be limited by cost if the large amounts of silver once used were still required. However, when made into nanoparticles with diameter less than 100 nanometers miniscule volumes of the noble metal can be used to treat large volumes of water. This is an important consideration given the cost of silver and a demand for treated water that grows exponentially both with population and economic development.

In fact, silver nanoparticles (AgNPs) have recently become a focal point for research and development of new, low-cost water treatment technologies. In colloidal suspension they have shown strong antibacterial ability against planktonic bacteria, even at low concentrations [5]. However, treating water with nanoparticles suspended in solution may be as wise as treating ulcers with lead powder. Though silver has generally been considered harmless to human health in small amounts [6] the long term health and environmental impacts of nanoparticles are unknown [7-9]. Nonetheless, the powerful ability of silver to clean water is unique and should be further investigated.

The purpose of this research is to identify applications for silver nanoparticles and to engineer solutions that advance the provision of clean water with minimal risk to human health

or the greater environment. The following pages will focus on one application in particular – antibacterial surfaces coated with silver nanoparticles – with an emphasis on the use of this material in low-cost ceramic water filters and other water distribution systems like showerheads. Surfaces often serve as a host to bacterial biofilms, a life stage in which they form complex colonies that are more suited to persist in the environment than individual planktonic cells. As a result, surfaces are both a target niche and a suitable location to attach nanoparticles to prevent the growth of bacteria from biofilms in drinking water. In this study the bacterial genus of interest is Mycobacterium, a group of bacteria that consists of opportunistic human pathogens and readily forms biofilm. This research will investigate the effect of antibacterial silver nanoparticle coated surfaces on the attachment and growth of biofilm.

2.0 MOTIVATION FOR THIS RESEARCH

2.1 NOVEL WATER TREATMENT TECHNOLOGIES

In 2000, the United Nations set forth a challenge, the Millennium Development Goals (MDGs), in which they aimed to halve the proportion of people who lack access to an improved water source[*] by 2015 [10-12]. The provision of clean water is an important step to reducing the burden of waterborne disease. According to the World Health Organization (WHO) more than 3900 children under the age of five die from a waterborne disease each day. Remarkably, much of the world is on track to meet the MDG goal for water access, with the notable exception of sub-Saharan Africa [12].

However, even if this goal is met there will remain a large, under-served population. Forecasts of population growth suggest that already overburdened infrastructure will have to serve an additional 784 million people worldwide to meet the MDG target by 2015 [12]. Furthermore, while access to an improved water source decreases the likelihood contracting a water-borne illness, it does not eliminate the risk. In many cases an "improved water source" may still confer waterborne disease. This is especially true in large urban population centers.

[*] An improved water source is defined to include public taps or standpipes, protected dug wells, protected springs, rainwater collection, or a piped household water connection located inside the user's dwelling, plot or yard, but not to include unprotected dug wells, unprotected springs, water trucks, surface water (river, lake, pond, etc.), or bottled water, the supply of which is considered unstable.

The number of cities with populations greater than 10 million has risen from 1 to 19 from 1950 to 2000, an indication of the significant worldwide trend towards urbanization. The burden of population growth in these urban areas has provided a significant infrastructure challenge. As the population urbanizes, municipal water utilities struggle to meet the demand for treated drinking water [13]. Large urban centers in the developing world are often plagued by intermittent flow and contamination (Figure 1). Additionally, water quality in municipal systems has suffered because the growth of water treatment systems cannot keep pace with burgeoning populations [14].

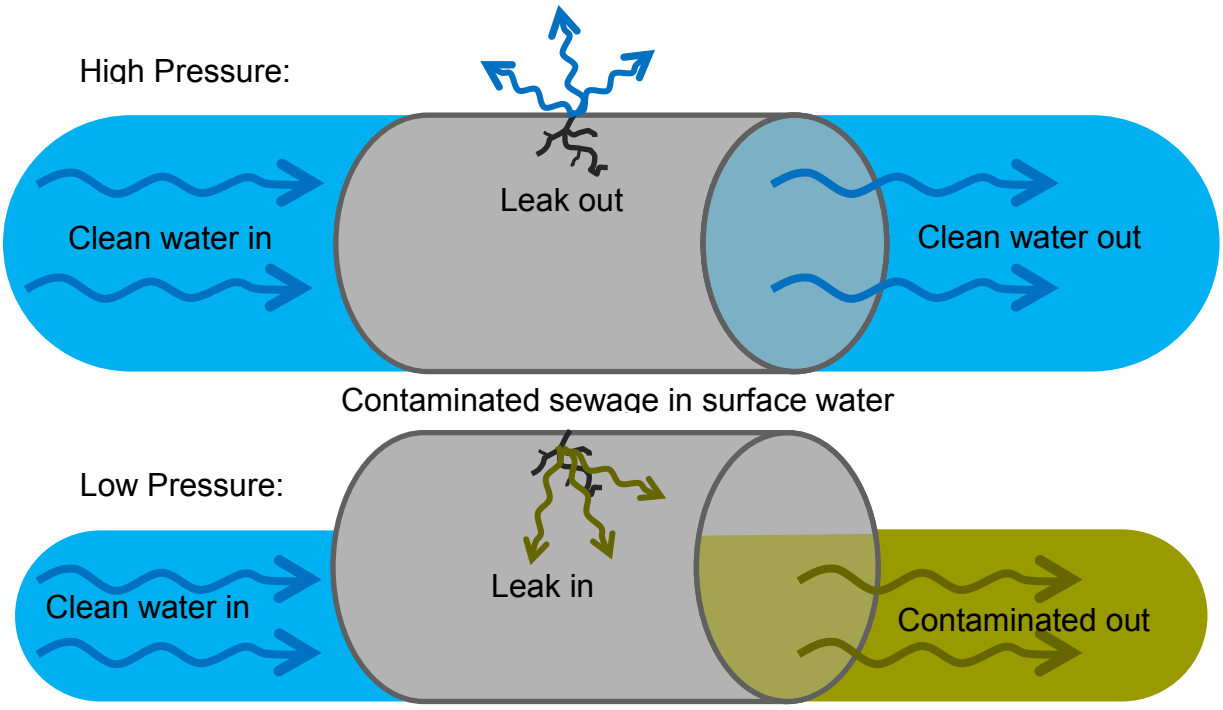

Figure 1: Low pressure in municipal water distribution systems leads to contamination as surface water more easily enters the piped system.

The WHO has identified several point-of-use technologies that can be used to bridge the shortage of infrastructure: chlorination, solar disinfection, filtration, combined flocculation and disinfection, boiling, and safe storage. Ceramic and sand filters have been identified as the best

solutions that provide sustainable and long-lasting benefits over the other alternatives [15]. Safe storage is, of course, a critical component of any water treatment technology.

The low-cost ceramic filter emerged as a water treatment option in response to the devastation caused by Hurricane Mitch in Nicaragua in 1998. The filters can typically be made by potters in the area where they will be used with mostly local materials [16]. Sawdust or another fine-grained fugitive phase is mixed with green clay before firing. During firing the sawdust burns out leaving large pores which help to effectively reduce the thickness of the filter and increase its permeability [15, 17]. The clay is formed into a shape that resembles a plant pot that sits in the open top of a plastic 5-gallon bucket. Raw water is added from the top and the filtered water is collected in the bucket, which is fitted with a spout [16]. See Figure 2 below.

Figure 2: Ceramic filter element in a 5 gallon bucket.

In order to increase antibacterial efficacy each filter can be treated with silver nanoparticles after it has been fired. The nanoparticles are dispersed in water and deposited either by painting this nanofluid on the filter's surface or by submerging the filter in the fluid and drying it in air. The application of silver has been proven to reduce bacteria in effluent water [17-19].

However, the method of antibacterial efficacy of this technology has not been fully elucidated in the scientific literature and as a result the filter's design has not been optimized. Water filters should be evaluated by five key metrics: 1) antibacterial efficacy, which is paramount to all others, 2) flow rate, 3) effective lifetime, 4) cost, and 5) design or application. Each of these criteria can be improved through the application of silver nanoparticles. The flow rate, effective lifetime and antibacterial efficacy are all limited by the growth of bacterial biofilms on the interior of the filter. This research is motivated by the need understand and improve a key deficiency in current filter processing - the deposition of silver onto the ceramic surface. Also, the effect of deposited silver nanoparticles on biofilm and the durability of nanoparticle films are of particular interest.

An important constraint in the design of ceramic filters and antibacterial surfaces is the need to maintain low cost and simplicity. The cost of water treatment is especially important in the developing world. Also, because the filters are generally made near where they will be used, the materials and processes must be widely available and relatively simple. Following these criteria will ensure that the antibacterial surfaces created will be feasible and sustainable in a wide variety of applications.

2.2 ANTIBACTERIAL SURFACES

Removing environmental bacteria from drinking water is, of course, not the only application for an antibacterial surface. This research is also motivated by the need for antibacterial surfaces in the human environment. A key stumbling point in modern medicine is the conundrum of nosocomial or hospital-acquired infections [20], a problem that is exacerbated

by the devastating effect of biofilm growth [21, 22]. Infections are also a confounding problem in the application of biomedical implants. When an implant is introduced into the body the success of the implant hinges on the coin-flip result of what microbiologists call the "race for the surface," wherein the surface of the implant is seeded by healthy tissue/bone and is accepted or it is seeded by bacteria that form a biofilm that is so impenetrable to antibiotics that rejection is almost a foregone conclusion [23].

To be effective against infection silver must be toxic to bacteria, and to be useful in human environments silver must also be non-toxic to human cells. As a component of drinking water silver has relatively few known health impacts. The most serious is a condition known as argyria, which arises from prolonged exposure to high concentrations of silver. Argyria causes a permanent blue discoloration of the skin, but otherwise has little negative effect. Only extreme cases of silver exposure are lethal [6]. The WHO estimates that approximately 5 µg/l of silver can safely be present in drinking water. This amount can rise to 50 µg/l when silver is used as an antibacterial in the water treatment process, because the slight risks of this higher amount of silver are overwhelmed by the benefit of removing pathogenic contaminants. The estimated daily consumption of silver is 7 µg per person. Only a small portion, from 0-10%, of the silver is absorbed. The no observed adverse effect level (NOAEL) of silver consumed orally is 10g in a person's lifetime. A level of 100 µg/l would yield less than half of the NOAEL over a 70 year lifetime [24].

Silver has been used in medical implants with some success [25] and a simple deposition method for silver nanoparticles that creates a durable coating could make this process less expensive and more viable in large scale.

3.0 BACKGROUND

3.1 LOW COST WATER FILTRATION

Motivation for this research stems from the desire to advance the development of low-cost ceramic filters for use in the developing world, though ceramic filters are also used in municipal water treatment and this work will apply to them. Ceramic filters can typically be made by potters in the area where they will be used with mostly local materials [16]. During processing, sawdust or another fine-grained fugitive phase is mixed with the green clay before firing. During firing this phase burns out leaving large pores which help to effectively reduce the thickness of the filter and increase its permeability. This increase in permeability increases the through filter flow rate and makes such filters feasible [17, 18]. The clay is formed into a shape that resembles a plant pot that sits in the open top of a plastic 5-gallon bucket. Raw water is added from the top and the filtered water is collected in the bucket, which is fitted with a spout [16]. See Figure 2.

In order to increase antibacterial efficacy each filter is treated with silver nanoparticles after it has been fired. The nanoparticles are dispersed in water and deposited either by painting this nanofluid on the filter's surface or by submerging the filter in the fluid and drying it in air. The application of silver has been proven to reduce bacteria in effluent water [18, 26].

Little is known about the effective lifetime of this type of ceramic filter. No formal study has examined how long it can be safely used; however, field research into the use and efficacy of

ceramic filters has shown that flow rate diminishes over time as a result of biofilm that grows on the interior surface of the filter. Furthermore, the NGOs that distribute these filters often encourage users to scrub the filter to restore flow rates [17, 19].

Preliminary research on this filter material demonstrated that silver nanoparticles are concentrated at the surface of the filter, rather than being evenly distributed throughout the porous microstructure, because of the dynamics of the drying process (see sections 6.1 and 7.1) [27]. The implication of this is that scrubbing of a filter to remove biofilm growth may also lead to removal of silver because the ceramic is quite friable – small pieces easily break off from the surface under low or moderate pressure. Thus, the growth of biofilm both diminishes the flow rate of ceramic filters in the short term and may reduce their efficacy in the long term.

3.2 BACTERICIDAL ACTIVITY OF SILVER

There are several metals with bactericidal properties, the most noteworthy of these being silver. Silver exhibits an oligodynamic effect, which is the ability to inactivate bacteria even in very small concentrations. Silver is toxic to a broad spectrum of bacteria while maintaining limited negative health impacts for humans. The antibacterial mechanism of silver is complex and until recently was not fully described. Typically, metal ions must enter the cell to cause damage, though cobalt-chromium nanoparticles have been shown to cause DNA damage across a cellular barrier [28].

To enter the cell metal ions may pass the chemiosmotic gradient across the membrane of bacteria or by a slower, more specific uptake process that cells activate in times of need [29]. Once inside the cell, metal ions can exert toxicity on bacteria by multiple biological pathways

simultaneously. There are five main categories of these pathways. In substitutive metal-ligand binding one metal ion can replace another at the binding site of a molecule, interrupting the biological function of that molecule. Next, reduction/oxidation reactions of metal ions with –SH thiol groups like glutathione can increase the ratio of the oxidized thiol groups and induce oxidative stress. Third, toxic metals can induce a chain of reactions that result in highly reactive oxygen species, which are destructive to all cell functions. Metal ions can also interfere with membrane transport processes by occupying binding sites or interfering with a membrane potential usually reserved for an essential nutrient. Finally, the proton motive force of the cell membrane can be interrupted by siphoning electrons from the respiratory chain [29, 30].

Silver ions can induce reactive oxygen species production through a metabolic cascade and iron misregulation. The ion can also increase membrane permeability through disruption of disulfide bond formation and misfolded protein secretion. This multi-faceted mechanism leads silver to be an effective broad spectrum antibacterial [31].

The proposed mechanisms of AgNPs and ionic silver are similar, via attachment to phosphate and sulfur groups contained in the cell membrane, which profoundly alters cell permeability, membrane protein signaling, transmembrane electron transfer, and respiratory processes, effectively inactivating bacteria [32-38]. AgNPs inhibit bacteria at concentrations in the micromolar range while silver ions are effective in the nanomolar range [33, 39]. Additionally, Ag-NPs can freely permeate the cell wall and accumulate to toxic levels in the cytosol by disrupting DNA polymerization [35, 40, 41].

Silver is the most obvious choice as a starting point for this work given the established benchmark of the material as a bactericide. Furthermore, use of AgNPs as bactericidal agents has

shown promise [5, 32, 35, 42-46] given the higher surface-to-volume ratio and the potential for nanoscale activity effects, which will be discussed below.

3.3 REACTIVE PROPERTIES OF NANOSCALE MATERIALS

Nanostructured materials have several features that make them excellent candidates for water purification and surface protection. Most obviously, the increase in surface area to volume ratio increases their reactive ability per unit weight of material, requiring substantially less material for a given application. This benefit has already been discussed for silver. In the nano-range, many materials also exhibit enhanced reactive properties, which can lead to reduced treatment time, more effective treatment, and higher selectivity.

Reactivity deviations from bulk material behavior are generally attributed to 'confinement' effects. These include the so-called 'shape-catalytic' effect stemming from steric hindrances arising at the nano-range, special electrostatic effects at nanostructured material interfaces, and reaction enhancement from increased surface defects [30]. Basically, the higher amount of surface atoms in such materials result in the added advantage of the appearance of unique reactivity behavior of atoms confined to the nanoscale surface. Confinement can also reduce aggregation, ensuring that the high surface areas the nanoscale enables are fully utilized [31].

Drawbacks of nanotechnology, besides toxicity risks, include difficulty to produce homogeneously structured materials and the requirement of high purity chemical precursors, especially in the case of chemical synthesis methods. The precursors and processing of nanoparticles can make them expensive to make. However, given that current silver NP

requirements for antibacterial action are less than 0.01vol% [32], the volume of silver needed will be low. The small concentration of AgNP required also mitigates potential issues with material aggregation; although special care must be taken during synthesis and material re-use collection to address this.

Overall, the use of material at the nanoscale has the potential to exhibit unique properties that are not necessarily predicted by the known behavior of the bulk. The utility of AgNPs as a bactericidal agent has already been well demonstrated and thus there is an expectation that a submonolayer surface coating of silver nanoparticles will similarly exhibit favorable reactive properties.

No conversation of nanomaterials is complete without an overview of the potential risks. The same highly reactive properties that make nanoparticles so interesting may also lead them to cause health [47-52] or environmental [9, 52-55] problems. Nanomaterials in general may confer risks and there are risks associated specifically with silver. In general nanoparticles are highly active because they approach the length scale at which specific physical or chemical interactions occur [52]. Furthermore, the scale of nanomaterial interactions often exceeds current abilities to observe and understand them using classical toxicological techniques [50]. Nanomaterial properties have necessitated a new toxicological science. In many cases nanomaterials haven been proven to show no cytotoxicity [9, 49]. And in fact nanomaterials existed in the environment long before the ability to engineer synthetic nanomaterials arose [56-59]. Taken individually or in small numbers nanomaterials are probably safe in biological and environmental systems. However, in high density the risks must be carefully observed. Though nanomaterials are typically diffuse in nature they are often accumulated through bioconcentration [60].

The toxic effects of silver arise perhaps from its rarity in the environment [29]. Relatively low exposure of living cells to silver in normal ecosystems provides few opportunities to evolve resistance or other defense mechanisms. Bioaccumulation of silver in soil is rather low except in areas near silver mines [61]. The concentrations of silver in seawater are also typically very low [62]. As mentioned above silver is toxic to bacteria and has limited negative health impacts for humans. Cytotoxicity (damage to cells) and genotoxicity (damage to genetic information) of silver were evaluated using changes in cell morphology, cell viability, metabolic activity, and oxidative stress. Silver and AgNPs can cause cell damage to mitochondria but only in very high doses [63, 64]. In general human cells can more easily resist AgNPs due to their complexity. Human cells have a nuclear membrane that helps protect against damage to DNA [65]. Also, in a larger context humans can exclude toxins, including silver nanoparticles, through the action of the liver [66].

3.4 IMPORTANCE AND CHALLENGES OF BIOFILMS

The prevalence of bacteria in the form of biofilm in the natural and engineered environment can be problematic and damaging. Biofilm is an important life stage of bacteria. While bacteria are often found in the natural environment and transported in the planktonic state, they preferentially live on surfaces, where they form complex communities [9]. For decades bacteria were only studied in the planktonic state or as colonies in nutrient-enriched agar plates. Biofilm has only been studied intensely recently [10].

3.4.1 Environmental Biofilms

Like any other living thing bacteria need a system to protect them to survive. Vulnerable as individuals, bacteria seek refuge in communities in order to persist in the environment. The ability to form biofilm has been observed in the fossil records and bacteria take this form to survive [67]. As a result, biofilms are ubiquitous in the environment. Many natural systems are either dependent on or influenced by biofilms, and the effect of biofilms ranges from beneficial to disastrous. For example, biofilms in wetland systems help to filter toxins. Biofilms exist at the air water interface in ponds. They also form in high shear conditions like a swiftly flowing stream. They form on the hard surfaces of rocks and minerals but also the soft surfaces of plant roots and animal intestinal systems. Bacteria in biofilms are remarkably adaptive and durable [67-69].

3.4.2 Biofilms in the human environment

For many, biofilm is one of the first things one sees in the morning and one of the last things one sees at night because the plaque removed when brushing one's teeth is a simple biofilm. The human oral microbiome is unique because teeth are one of the few surfaces in the body that does not have a built in mechanism of shedding and replacement. As a result, bacteria can readily colonize the tooth's surface. Biofilms that originate on the teeth can cause disease [70]. Some studies show that biofilm is damaging and causes negative side-effects like discoloration and halitosis [71] while others claim that bacterial biofilms on the teeth prevent colonization of more serious pathogens [70]. But biofilms are not always so harmless, either when they are in the body or other parts of the human environment.

Biofilms often have undesirable consequences. For example, biofilms that persist in air conditioning units can spread disease [72]. Fouling of cooling towers or other heat exchangers by biofilms can disrupt industrial processes [73]. Biofilms can also have a devastating impact in health, where they been linked to infections in female hygiene products [74] and other health related devices. Biofilms are also serious hurdles to the successful implementation of biomedical implants. When a foreign object is implanted in the body a phenomenon called the "race for the surface" occurs wherein the surface of the object is healthily colonized by tissue or bone or seeded with bacteria, infected and almost certainly rejected [23].

Infection can also occur when the biofilm does not originate within the body. A patient can develop infections from biofilms elsewhere in the hospital environment. Biofilms have been found in water circulation systems in dental chairs [75]. Cystic fibrosis patients are at risk of infection from methicillin-resistant staphylococcus aureus (MRSA) that is capable of forming biofilm [76]. Biofilms can also form in showerheads, where they enrich opportunistic pathogens. In a 2009 study, Feazel, et al. examined the bacterial communities in dozens of showerheads. They found among the plethora of harmless microbes a striking number of non-tuberculous mycobacteria including some from the pathogenic Mycobacterium Avium Complex (MAC). In showers, there is also an added risk that bacteria can be aerosolized and inhaled [77].

Biofilm has also been leveraged for its advantageous properties. Trickling filters in waste treatment plants are essentially biofilm reactors. The microbial layer sits atop a fixed bed of porous media and can absorb or adsorb organic contaminants. Slow sand filters, another low-cost water treatment alternative, develop a living layer of biofilm called a 'schmutzedecke' that functions in the same manner as the trickling filter. The biologically active layer significantly increases the antibacterial efficacy of the filter.

3.4.3 Biofilm Structure

Biofilm is characterized by three stages of development: attachment, colonization and growth. During the attachment phase, free-floating bacteria come into contact with a surface. Within minutes they can become firmly attached, though some bacteria release and reenter the bulk liquid. During the colonization phase bacteria produce a slimy matrix of extracellular polymeric substances (EPS) which provides a desirable niche for more bacteria. EPS is a mixture of high molecular weight polysaccharides and proteins. In the growth phase biofilm expands through the addition of various bacteria from the surrounding environment. In nature biofilm is rarely formed by a single bacterial species. Instead, a variety of species form complex communities. The growth phase is also characterized by the release of both individual bacteria or by the sloughing off of pieces of biofilm in order to colonize elsewhere [7-12].

3.4.4 Biofilm Resistance

Biofilms are more resistant to antibiotics and other bactericides than planktonic bacteria, and biofilm is more robust and pervasive as a result. In the environment bacteria are able to withstand a flux of toxins through chemical, physical, and physiological defense mechanisms. The susceptibility of bacteria to antimicrobials depends on the nature of the bacteria, the antimicrobial agent and the environment. Studies have shown that environmental determinants dictate the nature of biofilm in some species of bacteria, such as *V. cholerae* [78]. Antibiotics are less effective in biofilms because of poor penetration, lack of nutrients, and formation of persister cells. In addition, genetic variation in response to stresses contributes to resistance [30, 79].

Against toxic metal ions biofilms have adapted to develop resistance in a slightly different way. The biochemical mechanisms of toxic metals can be broken down into five main categories. Substitutive ligand binding occurs when metals bind to proteins in place of essential inorganic ions. Redox reactions with sulphur groups can interrupt thiol and disulphide groups and impair protein folding. Catalytic or Fenton-type reactions can produce reactive oxygen species (ROS). Transport of metal ions can compete with and inhibit normal membrane transport processes, which exacts an energetic cost. Finally, electrons can be siphoned from bacterial transport in the respiratory chain to reduce metal ions, essentially starving the microbial cells [30].

Each of the above processes assumes that the biofilm has already passed the attachment and colonization phases. The natural defenses of a mature biofilm are multiple and robust. However, biofilm may be more vulnerable during the attachment phase, when the constituent microbes more closely resemble planktonic bacteria. Considerably less research has been focused in this stage. Surfaces that have been treated with an antibacterial species may resist attachment and colonization of biofilm. They have been employed to create antibacterial surfaces in commercial products like socks [80] and washing machines [81] and in ceramic water filters [18]. These surfaces have been proven to reduce planktonic bacteria in effluent water. However, little is known about the effect of deposited AgNPs on the growth of biofilm.

3.4.5 Use of flow cell to culture biofilm *in vitro*

The primary tool for investigation of biofilm is the flow cell. The efficacy of antibiofilm techniques has been measured by *in vitro* [68, 73, 82-84] and *in vivo* [22, 71, 74, 75, 77, 85] studies. Biofilms are often observed in laboratory experiments through the use of flow cells and

other flow reactors [85]. In such reactors biofilms are grown by flowing nutritive media through a cell designed to facilitate qualitative and quantitative observation [83]. Flow cells are often designed for a specific experimental purpose such as observation in a microscope [73], assessment of physico-chemical properties [86], observation of flow dynamics [87], the use of electrochemical probes [88] and more. Efficacy of antibiofilm strategies can be measured by any of these methods.

A flow cell is a chamber that provides conditions for biofilm growth in a controlled environment where biofilm structure to be observed and probed. It consists of a reservoir for sterile input media, tubing, the test chamber, a pump and an effluent reservoir. The pump is used to control both the shear force across the biofilm surface and the flow of nutrients into the test chamber. The characteristics of the chamber depend on the type of biofilm to be grown and the method of analysis [73, 83, 86].

Biofilm structure is often probed in a flow cell with optical microscopy. Standard bright-field light microscopy is used to elucidate attachment and surface properties of biofilm. Confocal laser scanning microscopy has been used to reconstruct biomass distribution in 3-D [86]. However, this method is limited by the thickness and opacity of the biofilm. It is also a time-consuming and expensive method. Such advanced imaging techniques are necessary to probe fine structure of biofilm, but a faster, cheaper method is desirable to measure biomass and volume of the biofilm.

Investigation of the efficacy of antibacterial coatings requires accurate quantification of the extent of biofilm growth as well as the viability of the cells therein. The standard method for measuring viable cells in biofilm is to remove the biofilm from the surface, disperse the bacteria

in buffered media and count the colony forming units (CFU) [89]. This method is standardized and reasonably accurate but it is time consuming and requires destruction of the biofilm.

Another method for quantifying biofilm is weighing biomass. In this standard method an ultrafilter is dried to a constant weight, and then the biofilm is removed from its environment, dispersed in water and filtered. The filter is dried again and its mass is measured. The filter will trap bacteria in its fine pores and the difference between the dry weight pre and post-filtration will represent the biomass that was present. This method is often used in conjunction with viable cell count to calculate the ratio of viable cells to biomass, a measure of biofilm health [86, 89]. Again, this method is time consuming and requires destruction of the biofilm, which prohibits measuring the growth of a biofilm over time.

3.5 MYCOBACTERIA

Mycobacterium is a genus of actinobacteria that is characterized by the waxy properties of the cell wall. The genus includes several famous pathogens, such as *M. tuberculosis* and *M. leprae*, which cause tuberculosis and leprosy, respectively, in mammals. *M. ulcerans*, another pathogenic species, is among the most pervasive bacterial infections in West Africa today. Other important species of mycobacteria are *M. avium*, *M. marinum* and *M. smegmatis* (Figure 3). These are part of a larger group of non-tuberculous mycobacteria that are environmental bacteria pertinent to this study. *M. smegmatis* is of particular interest in biofilm research because it is non-pathogenic, it is a so-called "fast grower" and it forms biofilm easily. Cultures of smegmatis can be prepared in 24-72 hours while *M. marinum*, for example, can take up to three weeks.

Finally, *M. smegmatis* actively and easily forms biofilm [90, 91]. The majority of experiments for this research will be carried out with *M. smegmatis*.

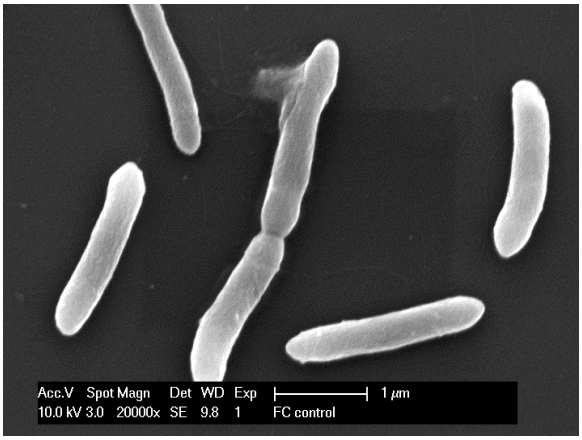

Figure 3: *M. smegmatis* bacteria

M. avium is another species of interest. As the name suggests *M. avium* is primarily associated with birds but can infect mammals, including humans. The *mycobacterium avium* complex (MAC) contains opportunistic pathogens that result in infections prevalent in AIDS patients and others with compromised immune systems [92]. Mycobacterial biofilms exist in nearly every water distribution system [93]. Genomic analysis of MAC infections from AIDS patients has conclusively determined that the bacteria originate in hospital water systems [94]. The primary infection routes are oral and aerosol [95]. Point-of-use treatment could alleviate the risk of infection for AIDS patients, but the high flow rates needed for showerheads and taps often prohibit the implementation of point-of-use filters with pores sufficiently small to physically remove bacteria.

M. marinum is a species of mycobacteria that is associated with fish and is an opportunistic pathogen. Generally non-pathogenic, *M. marinum* can lead to infection in people who have high exposure to fish. The bacterium enters abrasions on the skin and causes skin lesions. It is usually transmitted to humans through swimming pools and fish tanks although such

cases have become rare with improved cleaning technology [96, 97]. *M. marinum* is of particular interest in this research because it is primarily an aquatic bacteria and due its genetic proximity to both TB, with which it shares 85% of genes, and ulcerans, which is 99.8% genetically similar [97]. As a result *M. marinum* can serve as a safe laboratory proxy for far more dangerous pathogens. In addition, *M. marinum* is a waterborne species so it will share defense mechanisms with other bacteria that live in aquatic environments.

3.5.1 Susceptibility of mycobacteria to silver

Mycobacteria are susceptible to silver. In hospital warm water systems copper and silver ions have been used to kill mycobacteria. However, those treatments were less effective against mycobacteria than against legionellae [98]. Unfortunately, most studies of silver susceptibility have been carried out on planktonic bacteria. Mycobacterial biofilms have been found in point-of-use activated carbon water filters. When the filters are consequently treated with silver ions the mycobacteria developed resistance to silver through mutation and variation of gene expression [99]. A portion of this work will be devoted to showing that mycobacteria can also mutate to develop resistance to silver nanoparticles.

Resistance to any toxic metal ion can be attributed to three possible mechanisms: expulsion of toxic ions through efflux, segregation into complex compounds and reduction to a less toxic oxidation state. In practical terms, silver cannot be easily reduced by most cells. Complexation is metabolically costly in comparison to efflux. Because of the high metabolic cost, complexation is only efficient for low concentrations of ions. On the other hand, bacteria can be caught in a futile cycle of uptake and efflux so the lower cost of efflux only holds if the toxin is complexed by the larger bacterial population, which is not usually the case. In high

concentrations of silver efflux is more successful if the gene for the fast and unspecific chemiosmotic transporter is diminished by mutation, thus reducing uptake [29]. Usually, such tolerance results in slower growing and less viable cells. Slow growing mutant bacteria are then easily overgrown by non-mutants when cultured together.

3.6 DEPOSITION OF NANOPARTICLES

3.6.1 Surface properties of nanoparticles

Surface deposition of nanoparticles from a liquid is principally governed by particle-particle interactions and particle-interface interactions. In aqueous systems dispersion and electrostatic interactions generally determine interparticle potential. Most particles acquire surface charges in polar fluids such as water. The polarity and magnitude of surface charge is determined by the isoelectric point (IEP) and the pH of the liquid. When a particle is in a fluid with pH higher than the IEP the surface is deprotonated ($M\text{-}O^-$ for the case of metal oxides covered in surface hydroxyl species) and when the pH is lower than the IEP the surface is protonated ($M\text{-}OH_2^+$). For example, the IEP of silica is 1.7 to 3.5 at 25 °C, so the surface charge of silica in water (pH 7) will be negative. The magnitude of the charge is determined by the material properties and the difference between the IEP of the particle and the pH of the liquid. Varying the pH can modify the surface charge on the particles. Surface charge of particles in aqueous systems is called the zeta potential (ζ).

The Derjaguin, Landau, Verwey and Overbeek (DLVO) theory governs the stability of a particle in solution. The total potential energy function is a balance of competing contributions, as shown in equation (1).

$$V_T = V_A + V_R + V_S \quad (1)$$

Here, V_T is the total potential energy function, V_A is energy from the attractive van der Waals force, V_R is the energy from the electrical double layer repulsive force, and V_S is the potential energy due to the solvent, which is usually negligible in comparison to the other two. The van der Waals force is proportional to the inverse of the separation distance, D, between the particle and the surface. The repulsive force is proportional to $\zeta^2 e^{-\kappa D}$, where ζ is the zeta potential, and κ is a function of the fluid. Because of the balance of forces there is a potential energy barrier before the primary minimum where attachment in energetically favorable, as demonstrated in Figure 4. When the zeta potential, or surface charge, is lowered, the barrier to attachment is also lowered.

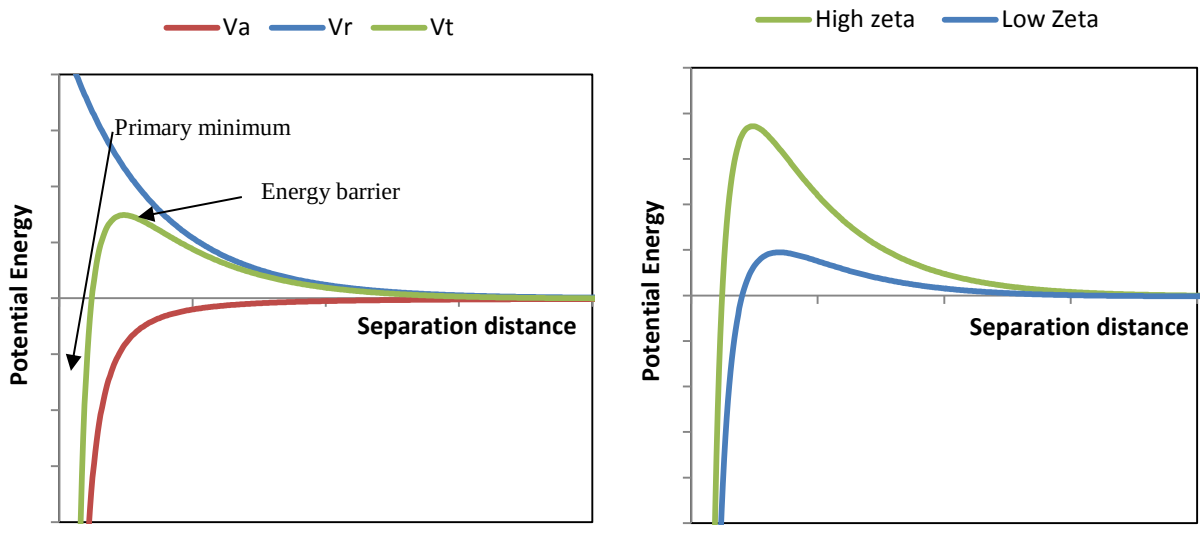

Figure 4: Diagram of the DLVO theory with the two principal contributions to the total potential energy (left) and energy curves for high and low zeta potential (right)

The IEP of silver is approximately 3.5 so the surface of silver nanoparticles is also negative in water with neutral pH [100]. Small silver nanoparticles are notoriously difficult to stabilize in water because of a low primary maximum in the interparticle potential [101]. As such, AgNPs are routinely stabilized with a soluble polymer called casein. Casein is a natural protein extracted from bovine milk [102]. The polymer aids and preserves dispersion by absorbing to the nanoparticle surface and producing a strongly repulsive interaction. Casein forms a micellular structure in which the hydrophobic portions of the molecule are folded inward and the hydrophilic portions folded outward. In such a configuration the casein micelle itself resembles a nanoparticle. The hydrodynamic radius of such a micelle is roughly 120 nm. When interacting with much smaller metal nanoparticles (e.g. r = 10 nm) the micelle can surround itself with nanoparticles as seen in Figure 5 [103]. The surface charge of the larger nanoparticle cluster can still be determined by the surface properties of the metal nanoparticle.

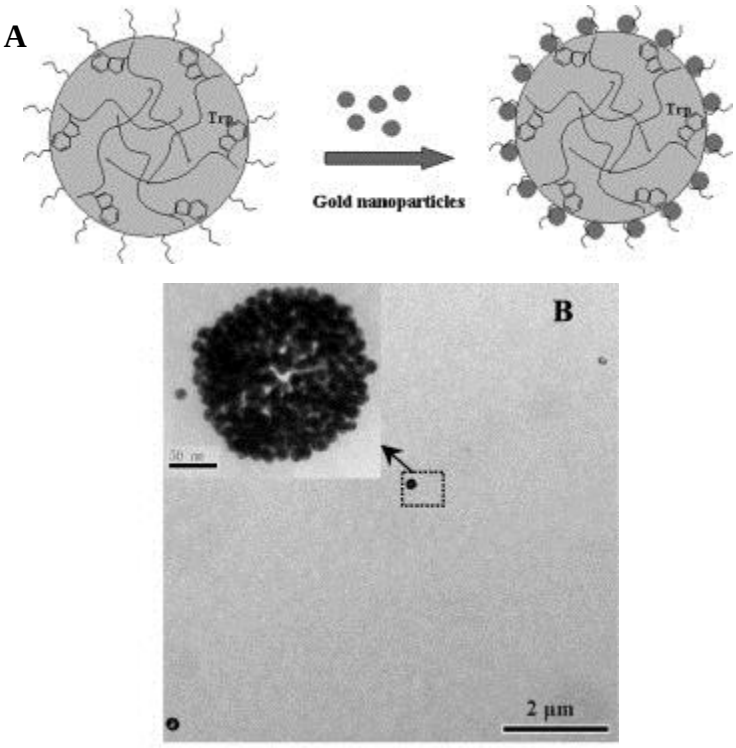

Figure 5: A) Micellular structure of nanoparticles gold nanoparticles with casein. B) Gold nanoparticles (d = 14 nm) surround a casein micelle to form a larger (d = 250 nm) cluster [103]

Particle-interface interactions can also be understood through DLVO. The surface charge of an interface is also determined by IEP and liquid pH. When a particle and surface have opposite charge there is no barrier to attachment so deposition is governed by diffusion and electrostatic attraction. This can occur when pH of the liquid falls between the IEP of the particle and the surface.

Deposition is more difficult and more interesting when an electrostatic repulsion exists between a surface and a colloidal particle. The barrier to surface deposition can be overcome in ways that allow for greater control over the dynamics of deposition and hence the morphology of resulting surface deposited nanoparticle films. Such surface deposition techniques will be discussed below.

Just as surface deposition and colloidal stability are governed by electrostatics so is desorption. Nanoparticles that do not easily attach to surfaces tend to also easily desorb. As discussed above one important quality of antibacterial surface coatings is durability. Durability can be enhanced by modifying colloidal chemistry[104], heat treatment [105], exposure to ultraviolet light [106], coating with a protective polymer [107].

3.6.2 Mechanisms Of Self-Assembly

While precise control of the spatial organization of nanoparticles and other nanoscopic building blocks over multiple length scales has been a bottleneck in the bottom-up generation of nanomaterials, self-assembly of such structures is routine in nature [108]. The basic principle of self-assembly is that all the information required to build the final structure is contained within the component parts, and encoded according to the laws of physics [109]. A general definition of self-assembly is the spontaneous organization of materials through noncovalent interactions

(hydrogen bonding, Van der Waals forces, electrostatic forces, interactions, etc.) with no external intervention [110]. It is noteworthy that self-assembly of objects ranging from nanometer to millimeter in size occurs through weak interactions [111]. Other physical interactions that have been shown to influence self-assembly are hydrophobic, colloidal and capillary, convective and shear, magnetic, electrical and optical forces [112].

A primary goal of research in self-assembled materials is to synthesize building blocks with the correct form through control of the properties that influence susceptibility to the forces described above. In nanomaterials, the influence of the surface, its chemistry and properties, is paramount [108]. Chemical control of charge, hydrophobicity, hydrophilicity, and functionality allows for command over the attractive and repulsive forces between nanomaterials and their surroundings [112]. It is this principle that allows for spontaneous self-assembly over multiple length scales to create integrated structures with emergent function and utility.

3.6.3 Evaporation Induced Self-Assembly

One tool that has been used to direct self-assembly is a liquid interface during drying [109, 110, 112-114]. For example, mesophases in thin films have been produced by drying of a homogenous solution of soluble silica and surfactant prepared in ethanol/water solvent. Preferential evaporation of ethanol concentrates the film in surfactant and silica. The progressively increasing surfactant concentration drives self-assembly of silica-surfactant micelles and their further organization into liquid crystalline mesophases [110]. Also, PbSe nanocrystals capped with oleic acid have been organized into ordered arrays by directed aggregation during drying. Aggregation is a phase separation that is triggered by the increase of interaction between nanoparticles when a good solvent (hexane or chloroform) is replaced by a

poor solvent (air) [113]. The presence of a liquid-vapor or liquid-liquid interface serves as a nucleating surface that causes ordered domains to grow [110].

3.6.4 Vertical Colloidal Deposition

An alternative to complex organic self-assembly is the more simple method for evaporation induced self-assembly, known as vertical colloidal deposition (VCD), which has been investigated vigorously [115-122]. While VCD is not currently suitable for assembly of complex 3-D structures, it is a capable method for assembly of 2-D particle arrays, and the synthesis does not require complex chemical preparation. VCD proceeds at room temperature and at atmospheric pressure by immersing a substrate vertically in a low-viscosity, colloidal suspension and then gradually exposing it to air by slowly removing the suspension (Figure 6) [117]. When the suspension is removed by evaporation the process is known as evaporation-induced VCD.

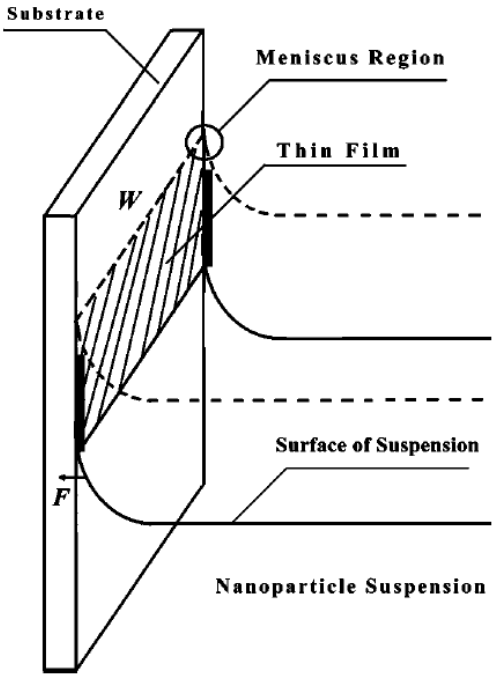

Figure 6: Schematic of Vertical Colloidal Deposition for nanoparticle thin film synthesis [115]

Similar to evaporation in organic solutions of nanoparticles discussed above, VCD creates a thin film in the meniscus region where particles are subject to interfacial forces at the solid-liquid-gas interface. The effect that these forces have on particle deposition can be controlled by careful selection of fluid concentration, evaporation speed, temperature, viscosity, particle size, and particle attachment affinity [115]. According to the theory of VCD posited by Diao, et al., the areal density of a deposited film can be described by equation (2):

(2) $$N = \frac{\psi \theta k_B T C}{6\pi r \eta v}$$

Where N is the areal density, ψ is the probability that a particle is adsorbed upon contact with the substrate, θ is the wetting angle of liquid on the substrate, k_B is Boltzmann's constant,T is the temperature of the system, C is the concentration of nanoparticles in the fluid, r is the radius of the nanoparticles, η is the viscosity of the colloidal suspension, and v is the speed of the moving meniscus [115]. See Figure 7.

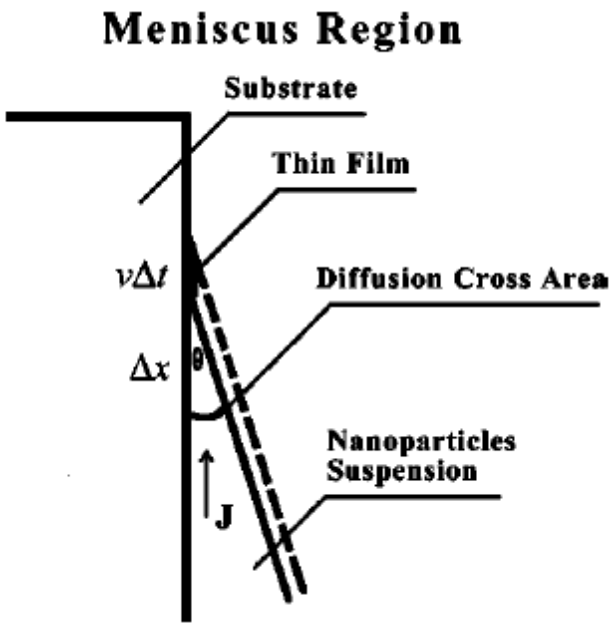

Figure 7: The meniscus region during VCD [115]

When the deposition is less than one monolayer the adsorption coefficient is linearly related to concentration, $\psi = KC$, where K is a constant based on the surface, particle and fluid properties. Thus, the areal density for sub-monolayer coverage is

(3) $$N_{submono} = \alpha_{submono} \frac{C^2}{v}$$

The constant $\alpha_{submono}$ is dependent on the conditions and properties of the deposition. When the coverage is greater than a monolayer the total areal density will be the sum of equation 1 and the areal density of a single layer.

(4) $$N_{multilayer} = N + N_{mono}$$

In the case where areal density is measured as a percentage of the area covered with particles $N_{mono} = 1$. The condition for sub-monolayer deposition is

(5) $$\frac{v}{C^2} \geq \frac{2rK\theta k_B T}{3\pi\eta}$$

Evaporation is not a necessary condition for this process, but merely provides a means for the motion of the solid-liquid-gas interface in the meniscus region. The formation of patterns in evaporation induced nanoparticle arrays is inextricably linked to the dynamics of dewetting at the nanoscale [109]. Deposition of nanoparticles has been demonstrated with non-evaporative removal of the solution [121] and, similarly, when the substrate is slowly pulled from the solution, a process known as dip coating [123]. Non-evaporative methods maintain the mechanism of evaporation-induced self-assembly while allowing for greater control of deposition speed and suspension concentration. VCD may also imitate the mechanism for deposition of silver nanoparticles by drying.

3.6.5 Current Limitations of VCD

It is possible for VCD to be used for synthesis of the advanced materials discussed above, but current limitations of the method must first be overcome. Repeatable processes that produce structures with minimal defects will be required for self-assembly of nanomaterials [124]. For materials with optical properties, defects or formation of domains have an enormous influence on diffraction properties [120]. Highly ordered colloidal crystals of polystyrene microspheres have been produced with minimum defects (Figure 8) [121], but this type of structure becomes much more difficult to produce with nano-sized particles. Furthermore, long range order has not been observed in submonolayer deposition. Rather than uniform monodisperse patterns, particles tend to aggregate into ordered rafts [124]. VCD theory described by Diao, et al. [115] does not account for lateral particle aggregation that is readily observed in submonolayer colloidal deposition – it is essentially a 1-dimensional model.

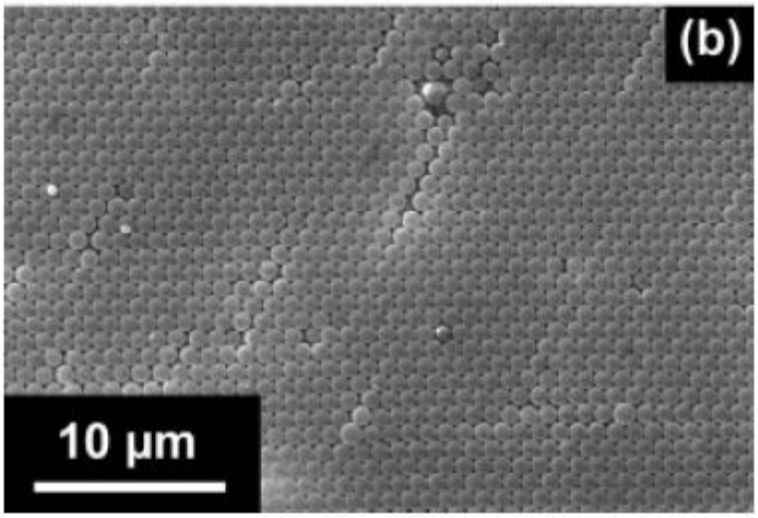

Figure 8: Ordered colloidal crystal of micron sized particles made by VCD [121]

In addition, relatively little work has been done to confirm Diao's theory with nano-sized particles. Prevo and Velev deposited gold nanoparticles with VCD and measured UV reflectance of the coatings but did not measure functional dependencies of speed or concentration to confirm Diao's theory for nanoparticles [125]. Lack of sufficient theoretical modeling is a hindrance to full understanding of the mechanisms involved in VCD. In order to provide greater control over VCD it will be necessary to identify the functional dependencies of the parameters laid out in Diao's theory for 2-dimensions and in the nano-range for particle size.

3.6.6 Coffee Stain Deposition

Comparably, a large amount of work has been done to elucidate the deposition of nanoparticles on horizontal surfaces. As drops of liquid dry on a surface, nanoparticles are deposited at the drying edge, just as in VCD, and this leads to the familiar coffee stain pattern [126]. It is believed that capillary flow [127], particle-particle interaction [128], and irregularities in the meniscus [129] all play a role in aggregation of nanoparticles during drying. These factors,

however, can produce controllable patterned structures [130]. A key to further control of structures self-assembled by VCD is differentiation of the mechanisms of lateral aggregation and more a thorough theoretical model that can describe these effects.

When a drop of coffee dries on a solid surface it leaves a dense ring around the perimeter (see Figure 9). The coffee stain is one of the most common depositions of particles by drying. The contact line becomes pinned to its initial position and capillary flow directs particles to the contact line where they are preferentially deposited. The mechanism of deposition in this case is in some ways similar to VCD. [126]

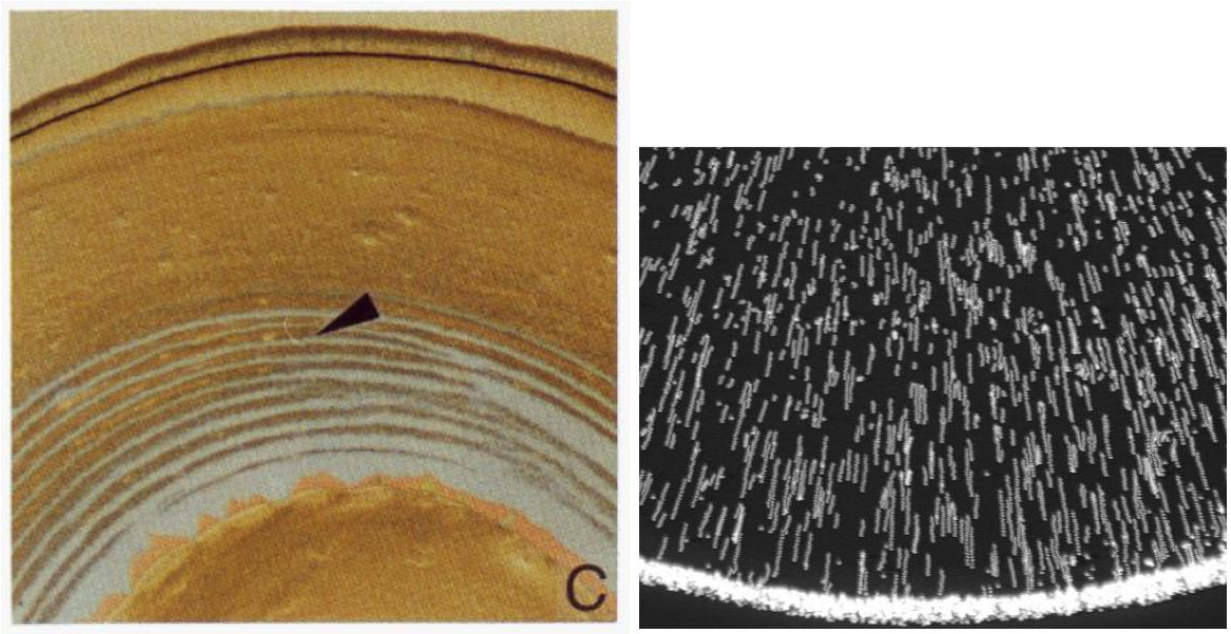

Figure 9: Stripe formed by the stick slip mechanism during drying of a droplet of a nanofluid (left) [131]. The motion of particles in a drying drop moving toward the pinned mensiscus [126].

When a suspension drop dries on a surface it is common to form a series of stripes. As liquid evaporates from the drop the volume diminishes and the contact line with the surface must recede in order to maintain surface tension balance at the triple interface between drop, surface, and air. Evaporation causes convective flow towards the air/liquid interface and the motion of the droplet further directs flow to the contact line. Since the particle flow is viscous, the flow

creates friction at the contact line that causes it to “stick.” Eventually, the friction is overcome by the forces of surface tension and the contact line “slips” to a new equilibrium point. During the “slip,” energy is dispelled at the contact line by discharging particles from inside the droplet. The particles form particle array films. The mechanism that forms lines in suspension drying patterns is known as the stick-slip mechanism. [131] Such mechanisms are likely at work in VCD and should be accounted for in theoretical treatment of the process.

4.0 HYPOTHESES

Deposited silver nanoparticles can enhance water treatment technologies by inhibiting growth of planktonic bacteria and biofilms.

This hypothesis will be investigated in six chapters, each with its own sub-hypothesis:

1) Deposition of silver nanoparticles in ceramic filters is controlled by drying dynamics.
2) Silver nanoparticles are toxic to environmental mycobacteria in planktonic exposure.
3) Silver nanoparticles will induce mutation to resist toxic susceptibility to silver when concentrated in the growth environment of mycobacteria.
4) An idealized deposition system can control morphology of AgNP surface coating by exerting control over drying conditions and concentration.
5) The durability of AgNP surface coatings can be improved with post deposition heat treatment without sacrificing antibacterial efficacy.
6) AgNP surface coatings inhibit growth of bacterial colonies when deposited on the surface of a membrane filter and can also prevent biofilm growth in real world flow conditions and such protection is not diminished by heat treatment.

5.0 OBJECTIVES

The objectives of this research are:

1) To determine the spatial distribution of AgNPs in porous ceramics.
2) To confirm the antibacterial effect of silver on several species of environmental mycobacteria in the planktonic state.
3) To show that silver resistance can arise in bacteria cultured in silver enriched environments.
4) To deposit AgNPs by VCD and test the functional dependence of several parametric variables to confirm existing theory in the regime of nano-sized particles and suggest a mechanism for the observed morphology.
5) To test the durability of silver nanoparticle films deposited by VCD and to investigate the effect of post-deposition heat treatment on durability.
6) To characterize the antibacterial effect of deposited silver nanoparticles on mycobacteria biofilm growth *in vitro*.

In section 6.0 these aims will be further discussed and experimental methods will be described for each.

6.0 METHODS AND MATERIALS

6.1 SEGREGATION OF SILVER IN LOW-COST CERAMIC WATER FILTERS [27]

Interest in the deposition of nanoparticles and the effect on biofilm was spurred by investigation of the properties of silver treated ceramic filters. In order to better understand and improve the role of silver in the bactericidal mechanism of such filters, the distribution of silver through the microstructure of the ceramic was investigated [27].

First, in order to understand the distribution of silver in a porous filter the microstructure of the material must be determined. The filter materials used in this study were porous ceramic tiles (~1cm thickness) made from a green body mixture of clay (kaolinite) and sawdust. The sawdust, a fugitive phase, burns out during firing to the sintering temperature (960^{o}C). The resulting material is a solid, though friable, porous ceramic with approximately 50% pore volume. The porosity and density of the ceramic were measured by the Archimedes method. The microstructure of this ceramic material was characterized by scanning electron microscopy (SEM) (Phillips XL-30).

After firing, each ceramic was treated with silver nanofluid by a soak-and-dry method. It was first immersed in silver nanofluid (0.22 or 2.2 g/l colloidal silver nanoparticles dispersed in deionized water). The choice of nanofluid concentration (0.22 g/l) reflects the standard concentration recommended in a guide of filter production distributed by Potters for Peace [16]. A higher concentration (2.2 g/l) was used to facilitate observation of silver in the ceramic

structure. The mean silver particle size was examined by photo correlation spectroscopy (Horiba LB 550). After the ceramics were immersed in the fluid, the container was sealed in a desiccator and evacuated before being allowed to soak for 24 hours to remove all the air trapped in open porosity. The samples were removed from the fluid and dried thoroughly on a glass dish in an oven at 50^{o}C.

Qualitative local chemical analysis was conducted using energy dispersive spectroscopy (EDS) to determine the presence of silver in the microstructure. Cross-sections were coated in palladium and examined in SEM in a wide magnification range (25x to 12,800x). EDS spectra were collected at regular intervals through the thickness of the filter. In an EDS spectrum the peaks for palladium, a coating used to control surface charging, and silver nearly coincide. The contribution to the spectra from each of these elements was determined using halographic peak deconvolution, a feature of the EDAX software used to collect the data.

External surfaces of the samples and unpolished through-thickness cross-sections were examined by digital optical microscopy (Keyence VHX-600K). Topological images of the external surfaces of the sample were produced by manually collecting a through-focus series of images over a range of 350 μm which were then reconstructed digitally into a 3-D image. Topological images were used to analyze the distribution of silver on the external surfaces.

After being treated with silver some samples were dried at room temperature. The weight of the sample was continuously recorded until drying was complete. The results were compiled into drying curves – plots of the rate of drying versus the moisture content of the ceramic sample.

A controlled drying experiment was performed in order to determine when the segregation of silver to the ceramic surface occurred. The ceramic was treated with the suspension containing 2.2 g/l of silver, and after impregnation half of the wet sample was

wrapped in wax film so that evaporation could not occur from the external surfaces of this part of the sample. The material was then allowed to dry at room temperature. The coloration of each surface was observed to determine the degree to which silver had segregated.

A drying curve was compiled to determine how much of the liquid absorbed into the porous ceramic dried from the surface. Samples were soaked in water and held under a light vacuum overnight to remove all trapped air. Then the weight of the sample was measured as the sample dried. The moisture content of the sample was plotted against time and the phases of drying were identified.

6.2 ANTIMYCOBACTERIAL EFFICACY OF SILVER NANOPARTICLES [132]

The bactericidal effect of silver nanoparticles is well-known and widely reported in the literature (see section 3.2). However, the effect has never been demonstrated and quantified with mycobacteria. In order to demonstrate the surface protective properties of deposited nanoparticles it is first necessary to confirm that the nanoparticles are toxic to the bacteria in question. Most of the studies of metal toxicity, including nanoparticles, are conducted on relatively few, fast-growing waterborne bacteria including *Pseudomonas aeruginosa* [133] and non-pathogenic strains of waterborne pathogens such as *E. coli* [45]. However, due to structural differences in the cell envelope mycobacteria are at times more resistant to bactericides and antibiotics [90, 91]. Furthermore, the bactericidal effect can vary widely among bacterial species, as will be demonstrated. It is desirable to show that AgNPs are toxic to mycobacteria in planktonic culture before moving on to show that they can also inhibit biofilm.

6.2.1 Susceptibility of planktonic mycobacteria to silver

The bacteria investigated here are *M. smegmatis*, *M. avium*, and *M. marinum*. *M. smegmatis* (MC^2155) was grown in Difco Middlebrook 7H9 broth containing 10% Albumin-Dextrose and 0.05% Tween-80 at 37 °C on a shaking table. *M. avium* and *M. marinum* were provided by Delphi Chatterjee. Both species were grown in Difco Middlebrook 7H9 broth containing 10% Middlebrook OADC Enrichment and 0.05% Tween 80.

In the case of plate growth, *M. smegmatis* was grown in petri dishes containing Difco Middlebrook 7H10 agar containing 10% Albumin-Dextrose at 37 °C. *M. avium* was plated on Difco Mycobacteria 7H11 agar containing 10% Middlebrook OADC Enrichment at 37 °C. *M. marinum* was plated under the same conditions as *M. avium* but was grown at room temperature (27 °C).

AgNPs were commercially purchased (Collargol, Argenol Laboratories, Spain) and are fully dispersible in water. The particle size as measured from TEM images is 12.6 ± 5.7 nm [134]. The morphology of the particles is equiaxed and selected area diffraction confirmed that the particles are metallic silver. The nanoparticles were mixed in deionized water and dispersion was aided through high energy ultrasonication for 15 minutes.

Stock solutions of AgNP were prepared and were subsequently added to 5 ml 7H10-ADC media to achieve concentrations of 6.25, 12.5, 25, 50, and 100 µM. Each concentration of silver enriched media was inoculated with *M. smegmatis* (~10^6 CFU) from a saturated culture. The amount inoculated (10 µl) was plated to count CFU. Samples were incubated on a shaker at 37 °C for 48 hours. Ten-fold dilutions from each sample were grown on agar plates and incubated until CFUs could be counted. The experiments were carried out in triplicate.

The toxicity of AgNP on *M. avium* and *M. marinum* was carried out by preparing concentrations of each by ten-fold dilution from saturated cultures. Agar plates were enriched with a range of AgNP concentrations (0-860 µM). Bacteria were inoculated on the plates in ten-fold dilutions. The plates were incubated in the conditions described in above. Plates were incubated until CFUs could be counted. The assay was carried out in triplicate.

Percent survival was calculated by dividing the CFUs counted from each concentration by the CFU from the inoculating volume. Values over 100% indicate bacterial growth while below 100% indicates a reduction from the initial bacterial load.

The effect of silver and silver nitrate was also measured over a time series for smegmatis only. For these experiments, 2.5 ml of 7H10-ADC media was added to a tube with 0.5 ml of silver nanofluid or nitrate from the stock solution (0.22 g/l). Half of this mixture - 1.5 ml - was removed and diluted with 1.5 ml of media, effectively reducing the concentration of silver by half. This dilution was done four times, resulting in tubes of 1.5 ml solutions with descending amounts of silver - 0.25 ml, 0.125 ml, 0.0625 ml, 0.03125 ml, and 0.015625 ml. From a saturated culture, 2 µl of smegmatis was added to each tube. The tubes were then placed on an agitating table in a 37 °C room. The bacterial counts were collected at 0 hours, 7hr, 13hr, 24hr, 31hr, 37hr, and 48hr. At each time, 100 µl was removed from each tube and mixed with 900 µl of sterile media. A sample amount of 10 µl was removed and plated on a 7H10-ADC boiled agar plate. Successive 10-fold dilutions were also plated. These plates were incubated at 37 °C for 2-3 days until bacterial colonies could be counted.

To ensure that the effect of AgNPs does not merely derive from the presence of silver ions in the as received AgNP nanofluid, the AgNPs were purified by washing using a 10 kDa ultrafilter according to a procedure described in the literature [135]. The purified nanoparticles

were then re-dispersed in water equal to the original volume. Appropriate volumes of purified nanofluid and unpurified nanofluid were added to 7H10 media and toxicity was measured as described above.

6.3 MUTATION OF MYCOBACTERIA IN RESPONSE TO SILVER NANOPARTICLE EXPOSURE

In hostile environments bacteria adapt to survive. When exposed to concentrations of silver near the minimum bactericidal concentration (MBC) bacteria may develop resistance to the large amount of bactericide in their environment through genetic mutation or variation in gene expression. The MBC is defined as the lowest concentration required to completely kill the bacteria. Silver resistant mutants of *M. smegmatis* were prepared by attempting to culture MC^2 155 in silver enriched agar plates.

6.3.1 Assay for isolation of silver nanoparticle resistant mutants

Beginning with the stock concentration (0.22 g/l) silver nanofluid was added to agar plates in descending concentrations of silver in successive experiments. Cultures were prepared in petri dishes containing Difco Middlebrook 7H10 agar containing 10% Albumin-Dextrose at 37^oC. Silver nanoparticles were added to the 7H10 plate media in various concentrations before the agar was dried. MC^2 155 bacteria were cultured on the silver enriched plates at 37 °C for 72 hours. When the concentration of silver was high it was completely toxic and no bacterial colonies survived. Eventually, some bacterial colonies survived when the concentration was lowered to 125 µM. Bacteria from surviving colonies were isolated and cultured independently.

Four different *M. smegmatis* isolates were extracted and subsequently grown in 7H9 broth containing 10% Albumin-Dextrose and 0.05% Tween-80 at 37^{o}C. These additives were added to all 7H9 growth media unless otherwise noted. For the purpose of identification the strains were named Ag-r^{1}, Ag-r^{2}, Ag-r^{3}, and Ag-r^{4}. In preliminary experiments all four strains and the unmodified MC^{2} 155 were cultured on agar plates with 7H10 media that had been mixed with AgNPs (540 µM) and $AgNO_3$ (13 µM). Subsequent experiments were carried out using only Ag-r^{1}. To avoid confusion the unmodified strain of *M. smegmatis* will be referred to as MC^{2} 155.

6.3.2 Comparison of Ag-r^{1} and MC^{2} 155 response to silver exposure in planktonic state

Ag-r^{1} bacteria were then re-exposed to AgNPs and $AgNO_3$ alongside the unmodified MC^{2} 155 strain to determine if the strains mutated to confer resistance to silver. Stock cultures of both MC^{2} 155 and Ag-r^{1} were grown in 7H9 growth media on a shaking table until the optical density was 0.3 to 0.5 as measured on a spectrophotomer (Jenway 6320D). In the case of plate growth, cultures were prepared in petri dishes containing Difco Middlebrook 7H10 agar containing 10% Albumin-Dextrose (ADC) at 37^{o}C.

Stock solutions of AgNP were prepared and were subsequently added to 7H10-ADC media to achieve concentrations of 6.25, 12.5, 25, 50, and 100 µM. In addition, silver nitrate was added to the same media making the concentrations 1.25, 2.5, 5, 10, and 20 µM. For both AgNP and $AgNO_3$ 5 ml of each concentration was added to 15 ml sterile test tubes in triplicate. Controls were prepared with 5 ml 7H10-ADC. From a saturated culture 10 µl of MC^{2} 155 was added to half of the tubes while the other half was inoculated with an equal volume of Ag-r^{1}. The samples were incubated on a shaker at 37 °C for 48 hours. After the incubation period the growth

of bacteria was observed by comparing the number of colony forming units per milliliter (CFU/ml) in each tube to the CFU in the inoculating load.

To measure CFU a 100 µl sample of the culture in question was added to 900 µl of ADC with 0.05% Tween-80. This culture was subsequently diluted in the same media in a ten-fold series. Three 10 µl samples from each tube in the series of dilutions were added to an agar plate with 7H10-ADC growth medium. After incubation at 37 °C for 72 hours bacterial colonies are visible. In less dilute spots the colonies merge into a large mass of bacteria. When dilute enough separate colonies can be counted. CFU is then calculated multiplying the number of separate colonies by the dilution factor of the spot as shown in equation (6).

(6) $$CFU = (counted\ colonies) \cdot (dilution\ factor)$$

Plates were photographed to facilitate counting colonies. The experiments were carried out in triplicate and averaged.

Growth in the presence of silver was expressed by calculating survival percentage according to equation (7)

(7) $$\%\ survival = \frac{experimental\ CFU}{inoculating\ CFU} \cdot 100$$

such that a percentage over 100% indicates growth over the number of inoculating bacteria. When cultured without silver or any other toxin bacteria can grow by upwards of 100,000% in 48 hours. Any survival percentage below the growth in the control indicates growth inhibition. When the survival percentage dips below 100% this is indicative of bacterial killing. Survival percentages were compared for MC² 155 and Ag-r¹ to establish whether Ag-r¹ can in fact resist the toxic effect of silver.

Silver resistance was also measured by observing optical density of planktonic cultures in a time series. First, planktonic cultures of MC² 155 and Ag-r¹ were prepared in growth medium

(7H9-ADC) with 20 µM AgNP, 2 µM $AgNO_3$ and negative controls. The cultures were incubated at 37 °C

Optical density was measured on a spectrophotomer (Jenway 6320D) at wavelength 600 nm. When optical density is less than 0.4 absorbance units (AU) it correlates to the cell density in the culture. Samples that had OD greater than 0.4 AU were diluted in a sterile medium that was prepared and incubated along with the experimental cultures. Background OD of bacterial cultures was removed by calibrating the spectrophotometer against a sterile control medium that was prepared alongside the bacterial culture. When dilution was necessary to measure OD the background sample was likewise diluted. OD was measured at the time intervals of approximately 8, 24, 34, 48, and 58 hours. OD for MC² 155 and Ag-r¹ were plotted on a logarithmic scale versus time and the growth rate (µ) and doubling time (t_d) were measured according to standard methods [136].

Next, the susceptibility of Ag-r¹ to isoniazid (INH) was measured and compared to the susceptibility of MC² 155. INH is a first line antibiotic used in treatment of tuberculosis – a disease caused by mycobacteria *M. tuberculosis*. The mechanism of action of INH is to couple with enzymes in the cell to create a complex that inhibits synthesis of mycolic acid and releases radicals that are damaging to cell function. Growth media were prepared with various concentrations of INH from 20 µg/ml to 0.31 µg/ml. This concentration was chosen because the minimum inhibitory concentration of INH on MC² 155 reported in the literature is 1-10 µg/ml. [137, 138] From saturated cultures of MC² 155 and Ag-r¹ 10 µl of bacteria were added to 10 ml of growth media in sterile 15 ml tubes. The cultures were incubated at 37 °C on a shaker for 48 hours. OD was measured at the conclusion of the incubation period.

Finally, the susceptibility to other toxic metals was measured to determine if silver resistance conferred a type of "core" resistance. Planktonic cultures of MC² 155 and Ag-r¹ were prepared with $ZnSO_4$, $CuSO_4$, $CoCl_2$, and $CaCl_2$. See Table 1 for the concentrations used. The concentration range for each metal ion was determined in preliminary experiments to establish a window of interest where susceptibility of the bacteria ranged from total toxicity to total resistance. As described above cultures were mixed in sterile tubes and incubated at 37 °C, CFU were counted, and survival percentage was calculated. Also, with select concentrations of $CuSO_4$ and $ZnSO_4$ separate cultures were prepared and the optical densities were measured and compared to controls. These CFU counting and OD results were compared to equal experiments with AgNP and $AgNO_3$.

Table 1: Concentrations of metal ions and nanoparticles for planktonic experiments

Metal ion source (Method)	Concentrations (µM)
AgNP	100, 50, 25, 12.5, 6.25
$AgNO_3$	20, 10, 5, 2.5, 1.25
$ZnSO_4$ (CFU)	8000, 4000, 2000, 1000
$CuSO_4$ (CFU)	320, 160, 80, 40
$CoCl_2$ (CFU)	2400, 1200, 600, 300
$CaCl_2$ (CFU)	2400, 1200, 600, 300
$AgNO_3$ (OD)	2
AgNP (OD)	20
$ZnSO_4$ (OD)	1000
$CuSO_4$ (OD)	250

6.4 VCD OF NANOPARTICLE FILMS

In order to better understand and improve the deposition of silver in ceramic filters an experiment was designed to replicate the deposition of silver by drying in a more simplified

geometry. Vertical colloidal deposition reduces the more complex porous microstructure to two dimensions. Diao's theory of VCD, as discussed above, states that areal density of deposited particles is proportional to particle concentration squared (C^2), and inversely proportional to deposition speed (v) as seen in equation (3) above. In equation (2) other factors that control areal coverage in VCD are the probability that a particle is adsorbed upon contact with the substrate (ψ), the wetting angle of liquid on the substrate (θ), the temperature of the system (T), the radius of the nanoparticles (r), and the viscosity of the colloidal suspension (η). In order to accurately apply the theory of VCD to deposition experiments each of these factors must be measured or estimated before completing theoretical calculations and comparing them to experimental results.

6.4.1 Preparation of nanofluids with AgNPs

Silver nanoparticles used in this research are commercially available (Argenol Laboratories, Spain). The nanoparticles are dried and delivered as a lustrous grey/blue powder. The nanoparticles from this company are specially designed to fully disperse in water. To do so they are coated with a proprietary polymer and electrolyte mixture that includes casein, a common protein found in bovine milk, and silver nitrate, which may be a remnant of the chemical precursors used during synthesis. The powder is approximately 70% silver by weight. It was measured by weight and added to deionized water. When mixed with water the particles immediately begin to disperse and form an orange/brown liquid.

To accelerate and facilitate the dispersal of the nanoparticles in water (especially for the nanofluids with higher concentrations) each nanofluid was sonicated using an ultrasonic horn for 30 minutes (longer for more concentrated fluids), taking care not to raise the temperature of the

liquid so much that evaporation occurred. An ice bath was used when times longer than 30 minutes were necessary.

The nanofluids were relatively stable. They did not aggregate and precipitate quickly. The particles are small enough that they can be maintained in dispersion indefinitely due to the forces of Brownian motion. In practice, the low concentration nanofluids used in this research showed no visible aggregation after several months. For concentrations larger than 5 g/l the particles began to aggregate during use and had to be sonicated to redisperse.

6.4.2 Particle size of AgNP

Particle size was measured by dynamic light scattering (DLS) (Horiba LB-550). A low concentration (0.22 g/l) nanofluid was used. Also, nanoparticles were imaged by TEM and particle size was measured from the resulting images. A small drop of silver nanofluid (2.2 g/l) was placed on a copper grid with graphene supported by lacey carbon (Ted Pella #01895) and allowed to dry thoroughly. The sample was then imaged by TEM (JEOL – 200CX) in bright field and selected area diffraction modes to determine the morphology and chemical makeup, respectively, of the nanoparticles. Images were analyzed in ImageJ to measure particle size.

6.4.3 Substrate wetting angle

Silicon wafer samples were cut with a diamond scribe to a size of 6x30mm, cleaned and then etched with an RCA clean. The RCA clean consisted of adding wafer samples to a bath of ammonium hydroxide, hydrogen peroxide and water in the ratio 1:1:5 for 15 minutes. The RCA solution was heated to 90 °C on a ceramic hot plate. After removal from the etching solution the wafers were rinsed in deionized water, then isopropyl alcohol and dried using compressed air.

Etching removes contaminants an oxidation from the pristine silicon and with time a thermal oxide of silica forms on the surface. This surface is used because it 1) is experimentally reproducible, 2) has a flat topology, and 3) allows for control of wetting angle through the growth of the thermal oxide.

The samples were then covered to avoid accumulation of dust and other contaminants and left in air at room temperature. With time a thin thermal oxide layer of silica grows on the surface. This is the surface of interest. Wetting angle of silicon substrates was measured with a drop shape analyzer with three concentrations of silver nanofluid at various times from 1 to 144 hours post cleaning.

The time was recorded as soon as each sample was dried. Contact angle was measured at various times after completion of etching using drop shape analysis (Kruss DSA100) of a sessile drop on the surface (Figure 10). Multiple drops were measure for each sample and multiple samples were analyzed at each time. Contact angle was measured with three concentrations of silver nanofluid - 0.22 g/l (0.01 vol%), 4.4 g/l (0.2 vol%), and 22 g/l (1.0 vol%).

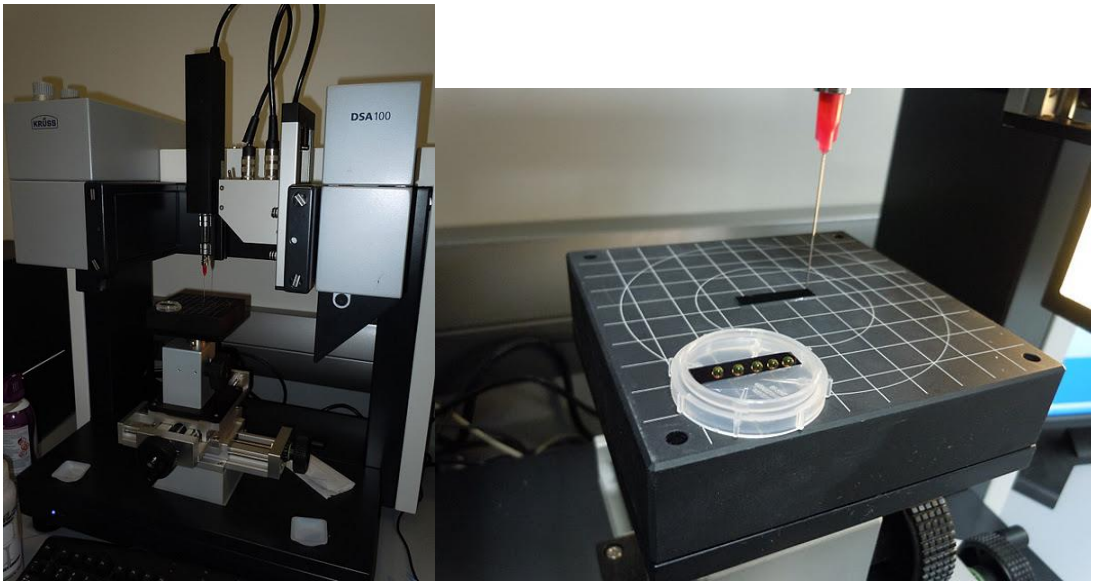

Figure 10: The drop shape analyzer (left) and the deposition stage with a sample and the syringe used to dispense a precise amount of the fluid of interest.

6.4.4 Temperature, viscosity and attachment probability in VCD

Temperature was held constant at 21 °C for all experiments. Because the nanofluids used in VCD experiments are primarily water the viscosity can also be held constant by limiting the volume fraction of nanoparticles. When the volume fraction of nanoparticles is less than 1% the viscosity is unchanged from that of water (1 mPa·s at 21 °C) [139]. In order to limit volume fraction to 1% the largest concentration of AgNPs used was 22 g/l. Coincidentally, this is 100 times larger than the concentration typically used to coat ceramic filters, as described in section 6.1. Particle attachment is difficult to measure. It was estimated to be between 0.6 and 0.8 by Diao, et al. [115]. This range will be used for theoretical calculations below.

6.4.5 Vertical Colloidal Deposition of silver nanoparticles

A dip coater (PTL-MM02, MTI Corp.) was used to deposit silver on silica at several speeds (1-5 μm/s) and concentrations (2.2 – 13.2 g/l). The standard preparation was used for the substrate – RCA etch at 90 °C for 15 minutes. A small volume of nanofluid was added to a glass cuvette, which was then placed in the dip coater, which is shown in Figure 11. A clip designed to hold the top edge of a silicon wafer sample was attached to the dip coater's motor and suspended above the nanofluid. A sample was then attached to the clip and lowered into the nanofluid. A shroud covers the nanofluid, the sample holder and a small volume of water, which is added to maintain humidity, minimize evaporation of the nanofluid and reduce dust contamination.

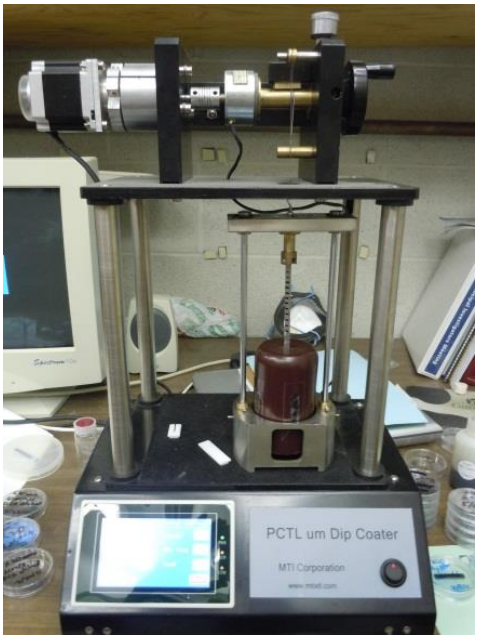

Figure 11: Dip coater for VCD of nanoparticle films.

A digital controller on the dip coater can be used to set the deposition speed. Depositions began at 1 μm/s and increased to 5 μm/s in 1 μm/s intervals. The series of deposition speeds was repeated for each nanofluid concentration. The samples were then labeled and stored.

Imaging of the samples was done on a Keyence Digital Optical Microscope (VHX-600). Optical microscopy was used as a fast way to examine the surface for evidence of deposition. The samples were then mounted on a stem, coated in palladium, and imaged by SEM (Phillips XL-30). Low magnification (200x) images were taken to capture higher scale morphological features on the order of tens or hundreds of microns. High magnification (>10,000x) images were captured to resolve individual nanoparticles and the structures they formed on the surface.

Initially, deposition was attempted with a concentration of silver that is typically used on ceramic filters (0.22 g/l) and at a speed that approximates the speed of a receding meniscus during drying (1 μm/s). However, little silver was deposited at this concentration. The deposition was repeated with higher concentration nanofluids to greater success. Concentration was varied from 2.2 - 13.2 g/l. Speed was varied from 1 - 5 μm/s.

6.4.6 Analysis of deposited films

Qualitative differences between films deposited under various conditions were observed by optical microscopy. To quantify the differences in the areal coverage of each film, the samples were imaged by SEM. The samples were coated with palladium in a sputter coater. A series of images was taken across a wide area of each sample. Positions of the images were chosen randomly. At least 10 images were captured at 200x magnification for each sample, and these images were used to calculate the areal coverage. The images have good contrast between the deposited film (light phase) and the underlying substrate (dark phase) (see Figure 12).

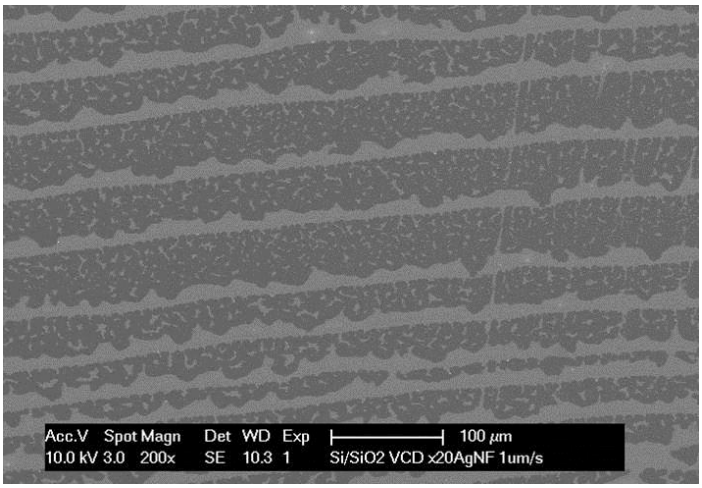

Figure 12: SEM image of a nanoparticle film (light phase) on an etched silicon wafer (dark phase)

Image analysis was performed using a MATLAB script written for the purpose (see Section 1.01(a)(i)Appendix A for the scripts). The program converted the image to binary where the substrate was black and the nanoparticle film was white. The primary function of the program is to determine the threshold between the portion of the surface covered in nanoparticles, which appears as a light phase, and the surface of the silicon wafer, which appears as a dark phase. The threshold was determined between the grayscale levels of the original image

by Otsu's method, which minimizes the variance between the two classes of pixels - foreground and background [140].

This threshold level is then used to convert the greyscale SEM image into a binary image where white represents silver and black represents uncoated surface. Also, noise was removed from the resulting binary image by removing dots of very small area. The area of the sample covered by silver was easily calculated by counting the number of white pixels in the resulting binary image. Figure 13 is the result when Figure 12 is converted to binary. Please note that the scale bar was removed before analysis. The coverage area was represented by a percentage. After parameters of the analysis were determined the MATLAB program was adjusted to process multiple images and produce a table of areal coverage percentages. This program was used to analyze the images (approximately 10) from each experimental condition. The functional dependencies of deposition speed and nanofluid concentration were plotted and compared to theoretical calculations.

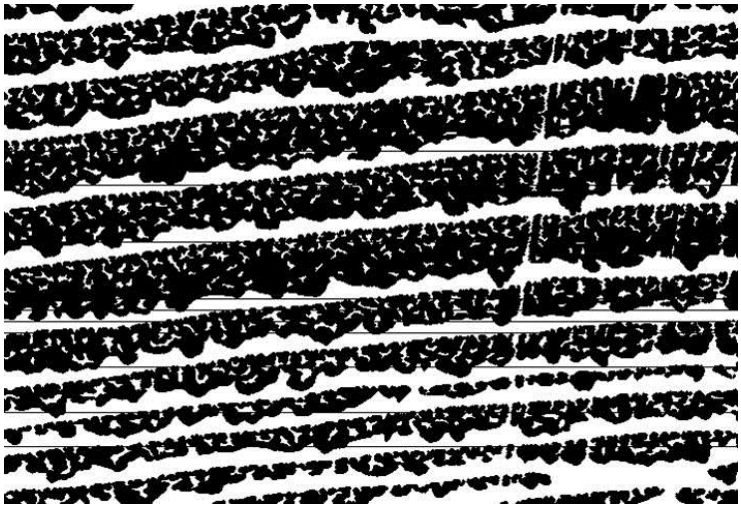

Figure 13: Binary image of a deposited nanoparticle film thresholded from Figure 12.

Binary images like the example in Figure 13 were further analyzed in Matlab to determine the average width of each deposited line and the density of lines in each image.

Random data columns were selected from a series of images. The width of each silver coated part of a column was calculated. Then small patches of deposited AgNPs were filtered from the data to leave only the widths of significant lines. The average width of these lines and the density of lines were then calculated for each deposition condition.

6.5 DURABILITY OF NANOPARTICLE SURFACE COATINGS

AgNPs were observed leeching from the surface of deposited films in preliminary experiments. The loss of AgNPs from the surface is especially apparent when a AgNP coated sample is submerged in water. Orange/yellow discoloration is an indication of leeched particles. Probably, some of the particles in the film are loosely attached and are quickly removed. Leeching of nanoparticles poses risks to the environment and to human health. Thus, durability is one of the most important aspects of engineering an antibacterial nanoparticle film. Again, the methods used to more firmly attach particles to a surface must avoid toxic chemicals and, if possible, be simple enough to apply to a low-cost ceramic filter.

6.5.1 Leeching of AgNPs from coatings in a flow cell

The durability of AgNP coatings deposited by VCD was examined by measuring the loss of nanoparticles from the surface of Si wafer samples in a flow cell. The loss was quantified by measuring the reduction of areal coverage of AgNP in microscopic images and the thickness of AgNP coatings in AFM. First a set of five deposition conditions was chosen so that areal coverage on the surface would range from 10-50%. See Table 2 for a summary of deposition conditions. Five samples were deposited for each condition. One set was analyzed as deposited.

Two sets were subjected to a flow cell as described below and two sets were subjected to heat treatment before being placed in the flow cell.

Table 2: Deposition conditions for durability experiments

Estimated Expected Areal Coverage	Concentration of Nanoparticle Solution (g/l)	Speed of Ascent of Substrate (µm/s)
10%	2.2	4
20%	2.2	3
30%	2.2	1
40%	4.4	1
50%	13.2	1

AgNPs were deposited on etched silicon wafers by the same methods used throughout this work (see section 6.4). The morphology and areal coverage of the films were assessed by optical microscopy (Keyence VHX-600). The films were then loaded into a flow cell apparatus described in similar to the one used for biofilm experiments in section 6.6. Deionized water was flowed across the surface of the deposited films at a flow rate that matched the flow of media in biofilm flow cells (0.06 ml/min) for 72 hours. The samples were then removed and the morphology was again assessed by optical microscopy. The durability of attachment of the particles will be measured by comparing the areal coverage before and after flow across the surface.

The wafers were imaged by optical microscopy at 200x magnification. The resulting color images were transformed using a binary threshold to identify areas of silver deposition. This was done using Keyence software built in with the microscope. At least 10 images were captured for each sample. The areal coverage of silver in each sample was calculated by counting

the white pixels in transformed images using a MatLab script. Two sets of AgNP-deposited samples were heat treated for 15 minutes after initial image analysis. One set was heated to 200 °C and the other was heated to 500 °C on a ceramic hot plate as shown in Figure 14. After heating, the samples were imaged and analyzed again before being subjected to flow in a flow cell.

Figure 14: AgNP deposited wafer samples undergoing heat treatment

A flow cell with six parallel channels was constructed for the purpose of these experiments (see Figure 15). The flow cell consisted of: a jar for influent water, silicone tubing, a peristaltic pump, ¼ inch inner diameter clear PVC tubing to hold the samples, flow locks, a jar for effluent water and various tubing connectors. Deionized water flowed through the channels at a rate of 0.06 ml/min for 72 hours. After completing the flow cycle samples were removed, dried, imaged, and analyzed as before. Areal coverage was compared post deposition, post heat treatment (where applicable), and post flow to determine the extent to which particles leached from the surface.

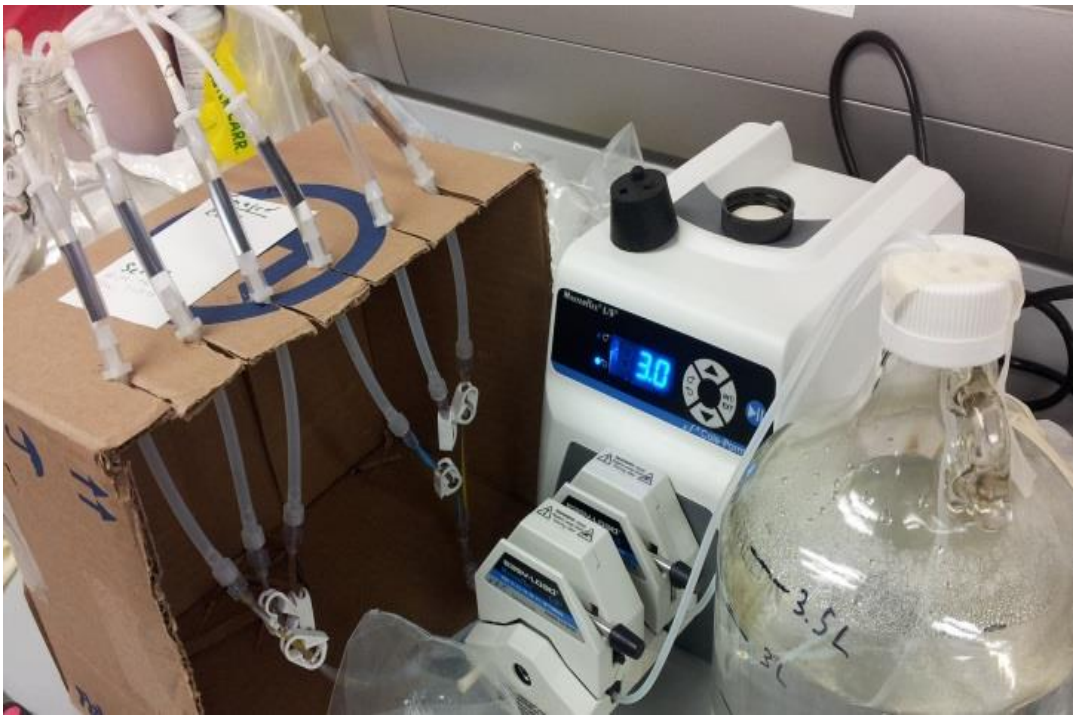

Figure 15: Flow cell for durability experiments

6.5.2 AFM thickness, width and loss

The durability of AgNP coatings on wafer samples that were subjected to flow conditions was also analyzed using atomic force microscopy (AFM). One set of wafer samples with AgNP coatings was analyzed by AFM without the flow condition. Two sets of samples were imaged after heat treatment and flow and two sets were imaged after deposition and flow. Depth profile images were captured in AFM (Digital Instruments D3100) in tapping mode with a standard tip. The AFM data was analyzed by first processing and smoothing using Gwyddion software. Profile contours were then extracted from the data and analyzed in Matlab and Excel to determine the maxima and linewidth of AgNP coatings.

6.6 INHIBITION OF BIOFILM FORMATION BY DEPOSITED SILVER NANOPARTICLES [132]

One of the primary interests of this research is to determine the ability of deposited AgNP coatings to inhibit biofilm growth. A series of experimental protocols was developed for this purpose.

6.6.1 Surface protection of membrane filters

Silver nanoparticles were deposited on microporous track etched polycarbonate membranes (Whatman 7060-1304). The membranes are 13 mm diameter and have 400 nm pores. Membranes are sterile as purchased and were handled and prepared in a sterile hood to prevent environmental contamination. Membranes were coated in AgNP by placing a drop (20 µl) of silver nanofluid (2.2 or 1.1 g/l) on the membrane and allowing it to permeate the pores while drying in air. The membrane became discolored where silver was deposited. Incorporation of silver nanoparticles was confirmed by SEM (Philips XL-30) and energy dispersive x-ray spectroscopy (EDS).

An assay was developed to culture bacteria on the surface of the membranes. A 15 ml reservoir of nutritive media (7H10-ADC) was added to petri dishes. Sterile fibrous cards were stacked in the bath of media so the topmost card sat above the level of the media as depicted in Figure 16. Three membranes (either silver-coated or uncoated) were placed on the card stack in each petri dish. The media, which soaked the cards thoroughly, ensures that membranes do not become dry and the capillary effect delivers nutrition to bacteria at the surface of the membrane. Approximately $6x10^5$ *M. smegmatis* (10 µl) from a saturated culture were spotted at the center of each membrane. CFU in the seeded bacteria was counted by plating dilutions from the saturated

culture at the same time as inoculation of the membranes. In these experiments the bacteria are larger than the pores of the polycarbonate membranes so they colonize the surface of the membrane and do not travel through or colonize in the pores or the media reservoir. A lid was placed over the petri dish and the samples were incubated at 37 °C to allow the mycobacteria to grow cultures.

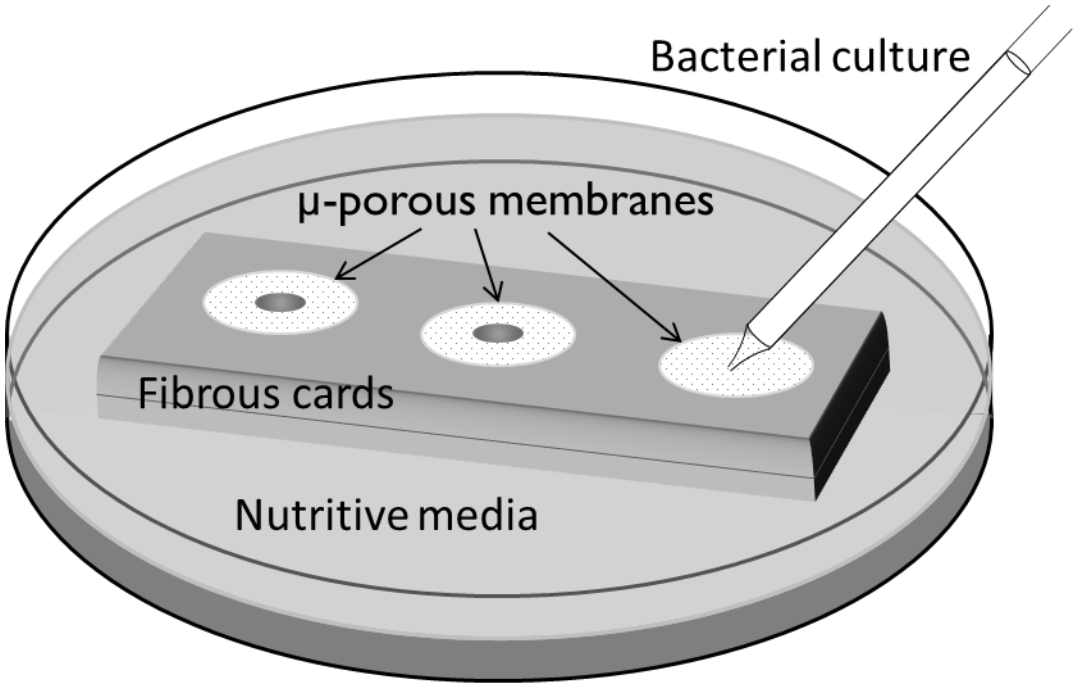

Figure 16: Diagram of membrane toxicity assay. Fibrous cards soaked in nutritive media support porous polycarbonate membranes. Bacteria are cultured on the membrane surface where growth is contained. System contained in sterile 100 mm petri dish [132].

After 72 hours the membranes were photographed, removed and processed for analysis by either microscopy or CFU counting. Preparation for microscopy is described below. To count the CFUs from each membrane samples were transferred to a vial containing 5 ml sterile media (PBS with 0.05% tween 80) and sonicated for 30 minutes to remove bacteria from the surface of the membranes. Dilutions from the vials were cultured on agar plates, as described above. Preliminary work has demonstrated that sonication is sufficient to remove bacteria from the surface of the membranes (unpublished).

Percent survival was calculated by dividing the CFUs counted from each membrane by the CFU from the inoculating volume. Values over 100% indicate bacterial growth while below 100% indicates a reduction from the initial bacterial load.

M. avium was also cultured on silver-coated and control membranes. The conditions for media, culturing and analysis were the same as above. However, as *M. avium* is a slower growing species the membranes were incubated for 6 days before colonies were visible on the control. The samples were then analyzed by counting CFUs as described above. Membranes were also photographed.

Membrane samples with colonies of *M. smegmatis* were examined by electron microscopy. Prior to imaging the samples were fixed in a 5% solution of formaldehyde and dried in air. They were then mounted and sputter coated with palladium. Imaging was performed in secondary electron mode over a range of magnifications from 50x to 25,000x. A series of membranes with 2.2 g/l AgNP coating and negative controls were inoculated as described above. Rather than incubate for 72 hours a pair of membranes (one AgNP coated and one control) were removed at time intervals up to 72 hours. Membranes were removed at 24, 41, 63 and 72 hours. The membranes were fixed in formaldehyde, dried, mounted and imaged by SEM. The resulting images were examined to compare growth over a time series.

Finally, the effect of concentration on *M. smegmatis* cultured on membrane filters was measured. AgNP was diluted from a stock solution (2.2 g/l). In total 12 concentrations were used (see Table 3).

Table 3: Concentrations for membrane experiments

Sample	Dilution factor	Concentration (g/l)
1.	1	2.2
2.	2	1.1
3.	8	0.275
4.	32	0.069
5.	64	0.034
6.	128	0.017
7.	256	0.0086
8.	512	0.0042
9.	1024	0.0021
11.	2048	0.0011
12.	4096	0.00054

A small drop (20 µl) of each concentration of nanofluid was added to a membrane filter. The membranes were placed on fibrous cards in dishes with media as described above. Then MC^2 155 was added to the membranes and the dishes were incubated for 72 hours at 37 °C. At the end of incubation the membranes were carefully removed from the cards and fixed in a 5% solution of formaldehyde for 1 hour. The membranes were then removed, dried and prepared for SEM. After being coated with palladium the samples were imaged at a range of magnifications. Primary imaging was done at 50x so that a large area of each membrane could be imaged. A series of images was collected by scanning in a pattern so that the images could later be compiled into a high resolution picture of the membrane surface. Usually, the total area of each membrane that had any bacterial growth was collected in 6-9 images.

The 50x series of images for each concentration were compiled in Adobe Photoshop. The larger image was then analyzed in ImageJ. This software has built in functions to threshold the images to identify bacterial colonies. The “Analyze particles” function of ImageJ was used to analyze the resulting black and white image to determine the number of colonies, size, and morphology.

6.6.2 Bacterial culture under flow conditions

Preliminary experiments with the flow cell consisted of developing a protocol for culturing a bacterial biofilm under flow conditions. Protocol were established for 1) assembly of the apparatus 2) sterilization of the apparatus 3) preparing biofilm media and inoculum 4) inoculation of bacteria 5) static seeding phase parameters 6) flow phase parameters 7) imaging and quantification of resulting biofilm 8) post experiment sterilization. A full protocol for biofilm experiments in a flow cell is shown in Appendix C.

The flow cell consists of tubing to deliver sterile media from a reservoir to the experimental chamber, where AgNP coated wafers were inoculated with cultures of MC² 155. The experimental chamber is a 7.5 cm section of ¼ inch clear PVC tubing with connectors that can hold a 6x35 mm wafer sample in place. A photograph of the flow cell apparatus is shown in Figure 17. Sterile media is pushed through the flow cell by a peristaltic pump. Flow breakers were added inline before and after the experimental chamber. A flow breaker is designed to ensure that there is not a continuous stream of liquid. This separates the media, which should remain sterile, and the flow cell, which is inoculated with bacteria. A secondary purpose is to remove bubbles that enter the tubing before they reach the flow cell. The flow cell has various tubing connectors and components to ensure that the apparatus does not leak and does not become contaminated during the experiment.

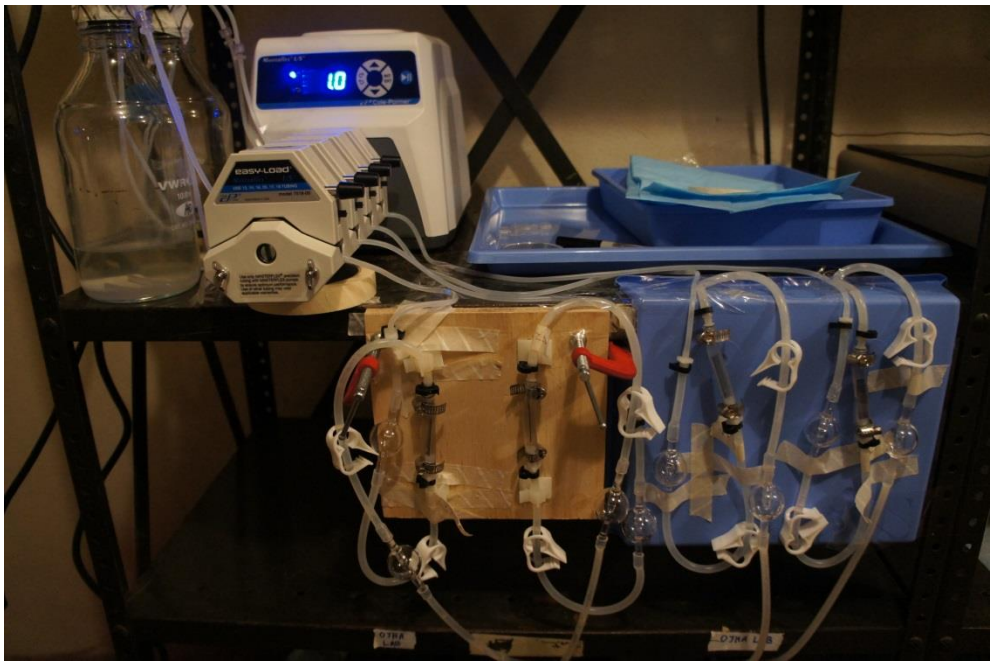

Figure 17: Photo of the flow cell apparatus

Initial test runs were carried out to establish assembly and sterilization procedures. Then three experiments were carried out with *M. smegmatis* bacteria. First, silicon wafer samples (three with deposited silver and a control without) were placed in the four experimental chambers of the flow cell. The AgNP coating deposition conditions are shown in Table 4. The cell was closed and all tubing and connections were attached. The entire apparatus was autoclaved at 121^{o}C. Meanwhile, 2 liters of sterile biofilm media was prepared. The media consists mostly of water, amino acids, and chemical nutrients like potassium and calcium (see Appendix A for recipe). An inoculum was prepared by preparing a saturated smegmatis culture (~10^{8} bacteria/ml).

Table 4: Deposition conditions for biofilm flow cell samples

Sample	VCD deposition speed (μm/s)	VCD concentration (g/l)	Expected areal coverage (%)	Actual Areal coverage (%)
Control	N/A	N/A	0	0
Low coverage	4	2.2	10	6.0
Medium coverage	1	2.2	30	24.2
High coverage	1	13.2	50	45.2

After autoclaving, the flow cell and tubing were connected to the media and waste containers in a sterile hood. Three 20 µl drops of inoculating bacteria were injected into each experimental chamber through the walls of the PVC tubing using a thin needle (25G) and syringe. During the seeding phase the flow cells were left for 1 hour to allow the bacteria to attach to the surface. These attached bacteria provide a seed for growth of biofilm.

The apparatus was then transferred to a 37 °C room and connected to a peristaltic pump with a pump head for each channel. Flow was started to introduce media to the system and to remove air from the tubing and experimental channels. The flow was left unimpeded for 80 hours before the samples were removed for imaging.

Full details of the procedure for removal of biofilm samples are show in Appendix C below. Shortly, the experimental chamber was cut, the wafer samples were removed with tweezers and the samples were immediately placed in a bath of 5% formaldehyde to fix the biofilm structure. After 1 hour, the samples were removed and rinsed in water and alcohol, then dried overnight in air. The samples were then prepared for imaging.

The VHX-600 digital optical microscope by Keyence is a computer controlled optical instrument with a variety of lenses from 5x to 5000x magnification. The working distance (for lenses up to 1000x) is long enough to accommodate the samples to be used in this research. It is a reflection mode light microscope that is suited for opaque samples. The microscope does not require oil immersion or contact. Furthermore, this method can be used to image opaque biofilm or biofilm on opaque surfaces because it is a reflected light technique rather than a transmitted light technique.

Biofilm samples were first imaged by digital optical microscopy at low magnification (x50). At this magnification the full width of each sample is contained in one image. The full

height of each sample was captured by 6-8 vertically scanned images. The individual images were compiled in Adobe Photoshop into a single image of the complete sample surface. Edges were trimmed for analysis.

The extent of biofilm growth in the compiled low magnifications was determined by developing a measure called biofilm growth intensity (BGI). BGI is a measure of both the areal coverage of biofilm and the density and thickness of biofilm. Each compiled image was converted from color to 8-bit grayscale and divided into squares with 500 µm edge length – approximately 700 square blocks for the typical 5 x 35 mm sample (see Figure 18). Each block was comprised of more than 17000 pixels, each with a grayscale level from 0 to 255. The average grayscale intensity for each of these pixels was measured. The averages for each of the 700 blocks were separated in to 10 equally spaced bins, as if to construct a histogram. For example, all blocks with an average grayscale value from 0 to 25.00 were placed in the first bin. Blocks with averages between 25.01 and 51.00 were placed in the second bin and so on.

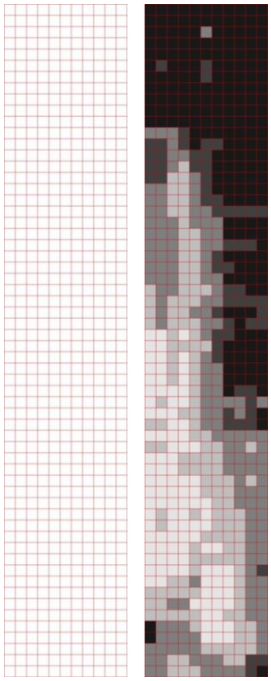

Figure 18: Example of block structure for measurement of BGI

A nominal intensity was then applied to the bins according to Table 5. The number of blocks in each bin was multiplied by the intensity values shown in the table. Zero intensity was chosen as the minimum because many of the blocks with such low grayscale had no evidence of biofilm growth at all. As will be shown higher grayscale values correspond to higher density of biofilm growth. The sum of the intensity level for each bin is summed and divided by the total number of blocks in the image to calculate BGI. An example calculation is shown in Table 5.

Table 5: Intensities and bin counts for each grayscale level in example BGI calculation

Bin	Grayscale	Intensity	Example bin counts	Bin count * intensity
1	0-25	0	0	0
2	25-51	0.10	49	4.9
3	51-77	0.20	55	11
4	77-102	0.30	65	19.5
5	102-128	0.40	153	61.2
6	128-153	0.50	150	75
7	153-179	0.60	127	76.2
8	179-204	0.70	61	42.7
9	204-230	0.80	0	0
10	230-255	0.90	0	0
11	255 exactly	1.00	0	0
		SUM:	660	290.5
BGI = 290.5/660 = .440				

BGI was measured from each sample (control and three AgNP coated) in triplicate experiments. The calculation of BGI was done using a Matlab script shown in Appendix B. The final intensities were averaged and statistical analysis was performed to determine if the amount of silver coated on a wafer sample resulted in a drop in BGI. First, BGI was plotted with areal coverage of silver in a scatter plot. Linear regression was used to calculate the slope and intercept of a linear trend line of the data and to determine if both were statistically significant from 0 with $p < 0.05$.

It was observed that deposited AgNPs as part of the antibacterial coating contributed to the grayscale brightness of some images. An attempt was made to remove this background to show only the intensity from growth of biofilm. This was done by imaging samples that had been placed in a flow cell with water but no bacteria. These samples were also used to measure the durability of AgNP coatings in section 6.5.1. The samples were imaged and analyzed in by the same methods described above. Background was removed by subtracting the BGI of samples with AgNPs only from the BGI of samples with AgNPs and bacterial biofilm. Statistical analysis was also performed on this data.

Finally, one flow cell experiment was conducted with a set of samples that were coated with AgNPs as before and were heat treated before placing in the flow cell. The wafer samples were heated to 200 °C as was done in section 6.5. In the flow cell, the samples were inoculated with MC² 155 and flowed in 37 °C incubation for 80 hours. The samples were prepared and imaged to calculate BGI. Comparing BGI of the heated sample to non-heated samples was used to determine if the heat treatment resulted in changed antibiofilm ability.

After low resolution imaging was completed samples were also imaged in an optical microscope at magnifications up to 1000x. When optical microscopy was completed select samples were coated with Pd and imaged by SEM (Phillips XL-30) in secondary electron mode.

7.0 RESULTS AND DISCUSSION

7.1 SEGREGATION OF SILVER NANOPARTICLES IN LOW-COST CERAMIC WATER FILTERS [27]

In section 6.1 the methods used to analyze the distribution of silver nanoparticles in low-cots ceramic filters were described. The first step was to investigate the microstructure of the ceramic filter material.

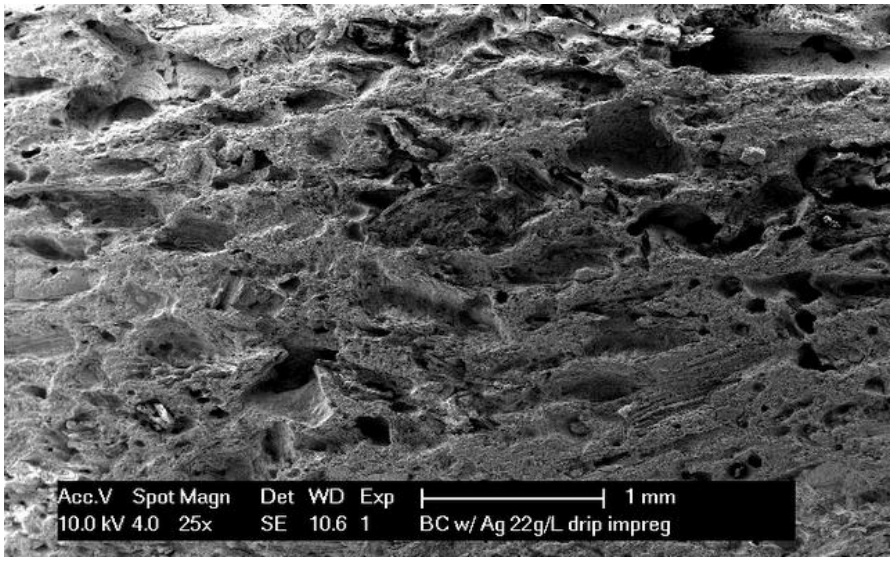

Figure 19: General microstructure of the ceramic filters showing large pore cavities that tend to be surrounded by ceramic containing finer porosity.

Filter materials used in this research have a rigid porous structure. Figure 19 shows a low magnification SEM micrograph of a cross-section through the thickness of the filter. The microstructure of the filter is spatially heterogeneous over long length scales, comparable to the thickness of the filter. The filter contains large pore cavities that range from tens of microns to

over 1 mm in size – much larger than the size of typical bacterial contaminants, as described by a factsheet published by WHO [24]. These cavities were primarily created by the pieces of sawdust that were burnt out during heating to the sintering temperature.

While it is difficult to come to definitive conclusions about connectivity of the pores from the imaging of a cross-section, the large cavities appear to be isolated from one another – probably because sawdust pieces become coated with clay during mixing of the green body. These large pore cavities are interconnected by a matrix of fine porosity produced by partial vitrification of the clay during firing. The Archimedes density measurements confirm that all the porosity is open and the large pore cavities are fully connected to the surface of the sample. The size, distribution, and morphology of the fine porosity in the partially vitrified ceramics should ultimately control permeability and the ability of the filter to remove contaminants by size exclusion.

The silver nanoparticles used in this section were characterized and the results appear in section 6.4. When the samples were examined by SEM, EDS spectra collected in near surface pores usually indicated the presence of silver. Detection of silver at the surface was intermittent and did not suggest the presence of a continuous coating for the samples when treated with low concentration silver nanofluid (0.22 g/l). As EDS measurements were collected through the thickness of the filter the spectra did not indicate silver in the interior of the sample, except in large flaws that were open to the surface. For example, in one sample silver was identified both at the surface and as deep as 50 μm below the surface. However, some EDS spectra collected at the surface did not contain evidence of silver and no spectra collected below 50 μm indicated silver. The data suggest that silver was segregated to the external surfaces of the samples.

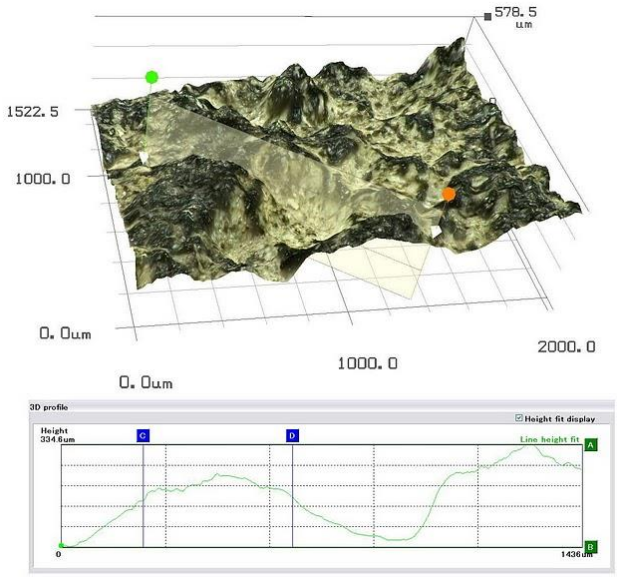

Figure 20: An example of the topology of the external surface of a ceramic sample with silver segregated to the prominent points on the surface.

When the sample was treated with the more concentrated silver suspension (2.2g/l), the external surface of the samples were colored grey by deposited silver and coloration did not extend to the interior. Figure 20 shows an image of an external surface of a sample that was treated with the 2.2 g/l dispersion. The surface shows a series of irregular peaks and valleys which extended to a depth of approximately 300 μm on the highlighted section. More importantly, the imaging showed the grey colored silver is segregated to the peaks on the surface topology with very little discoloration in the valleys.

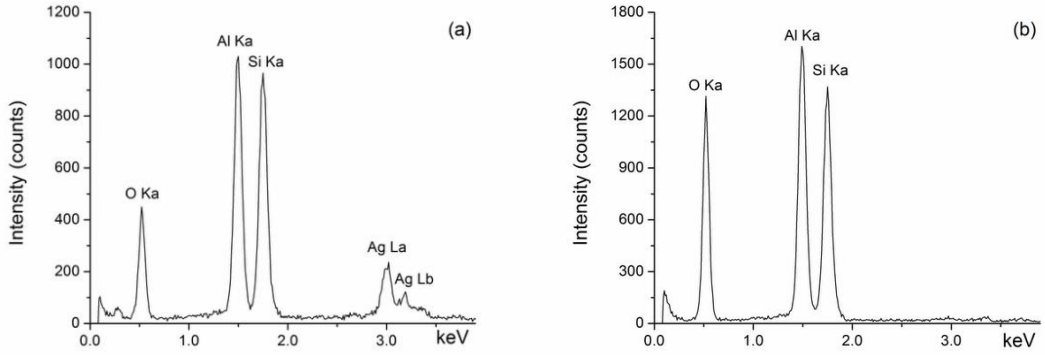

Figure 21: EDS spectra measured at the surface of a kaolin sample impregnated with 2.2 g/l silver nanofluid. The EDS spectrum collected at a prominent point on the surface (a) indicates presence of silver. The EDS spectrum collected in a valley nearby (b) does not indicate silver.

This observation was confirmed with the clear decline of silver in EDS spectra as measurements progressed away from the prominent points on the surface of a sample. Figure 21 shows two EDS spectra, the first was collected at a prominent point of the ceramic surface (a) and the second at a nearby valley (b). The spectra indicate the presence of silver at the prominent point and show no silver at a low point – confirming the segregation observed in Figure 20. The variation in oxygen in these spectra may result from surface contamination or presence of different aluminosilicate phases.

EDS spectra were also collected in a through-thickness cross section of a sample impregnated with higher concentration silver nanofluid. In one example silver was observed at the surface and as much as 180 µm below the surface, but no spectra collected below 180 µm contained any evidence of silver. No silver appeared in spectra collected at the bottom of any of the samples, regardless of concentration of silver nanofluid.

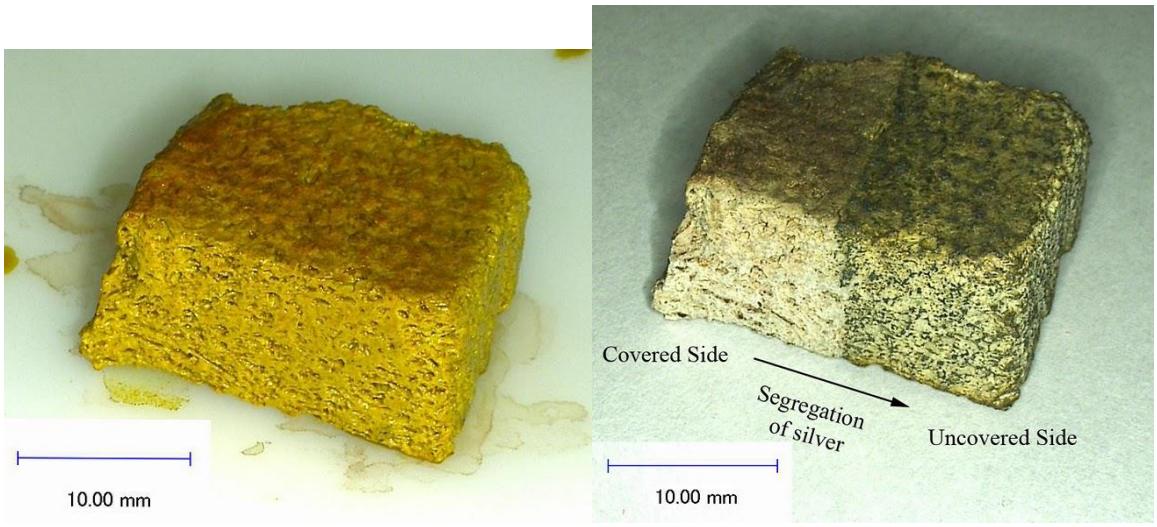

Figure 22: The controlled drying experiment (left) before the sample was partially wrapped and (right) after drying.

It is clear that silver segregates to the exterior surface of the porous ceramic, but it is difficult to determine the role of processing in segregation by observing a sample of the finished product. To further address this question a controlled drying experiment was performed in which the ceramic was treated with the suspension containing 2.2 g/l of silver. After impregnation, the still wet saturated sample (Figure 22 (left)) had a uniform brown/orange color imparted to it by the silver dispersion. Half the sample was wrapped in wax film so that evaporation could not occur from the external surfaces of this part of the sample. The material was then allowed to dry at room temperature. Figure 22 (right) shows that after drying, the external surface that remained unwrapped had the dark grey coloration identified with presence of the silver. The external surfaces that remained wrapped were light in color and showed no such visible evidence of silver. Therefore it can be concluded that the nanoparticles are segregating to the external surfaces from which evaporation takes place during drying.

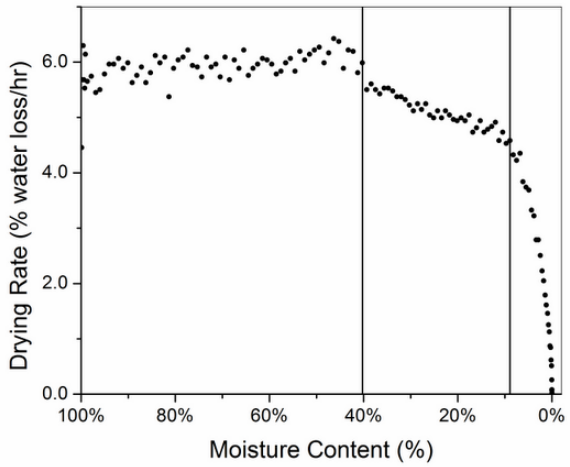

Figure 23: A drying curve (rate of drying vs. moisture content) for a ceramic filter sample. The curve shows the constant rate period and falling rate periods of drying. Note that 90.3% of the drying occurs during the first two periods while water is evaporating from the external surface of the sample.

Figure 23 shows the drying curve of a ceramic filter sample. The drying process follows typical drying behavior as described by Scherer [141], Whitaker [142], Rahaman [143], Schlünder [144], and Belhamri [145]. According to Schündler [146], at high moisture content, evaporation results from 3-D vapor diffusion in the vicinity of the wetted surface of the ceramic. In this constant rate period the moisture content is reduced to 40% in this sample. During the first falling rate period (between 40% and 10% moisture content) evaporation continues at the surface of the porous ceramic because the surface remains connected to liquid in the interior by funicular pathways. Flow towards the evaporating surface drives water and the associated silver nanoparticles away from the interior of the sample. Only at a critical point near 10%, when drying rate declines precipitously, does significant drying occur in the interior of the sample.

The drying curve shows that approximately 90% of the water in the sample evaporates during the constant rate period and the first falling rate period, both of which are surface drying periods. This implies that 90% of the silver that resides in the saturated sample will be transported back to the evaporation surfaces of the ceramic and be deposited there as the water is

removed. This drying behavior explains the mechanism by which silver particles are concentrated at the surface of the ceramic by continuing evaporation.

This microstructural investigation revealed that the processing and impregnation of low cost ceramic filters are not optimal for antibacterial effectiveness. The inclusion of sawdust as a fugitive phase in the clay mixture creates large pore cavities in the microstructure. The treatment with silver by a soak-and-dry method results in strong segregation of the silver nanoparticles to the exterior surfaces of the material. Controlled drying experiments showed that the silver nanoparticles segregated to evaporation surfaces and that the flow during drying may return as much as 90% of the silver to the surface.

7.2 EFFECT OF SILVER ON ENVIRONMENTAL MYCOBACTERIA

7.2.1 Toxicity of AgNP for planktonic mycobacteria

The percent survival of mycobacteria when exposed to silver nanoparticles is shown in Figure 24. Without AgNP in the media *M. smegmatis* grew 274,000% in 48 hours (Figure 24a). Growth was inhibited below 12.5 µM AgNP. Reduction over the seeded bacteria by 98.7% was achieved at 100 µM AgNP. At 200 µM the AgNPs were completely bactericidal; no CFUs were counted. There is a clear correlation between AgNP concentration and antibacterial effect.

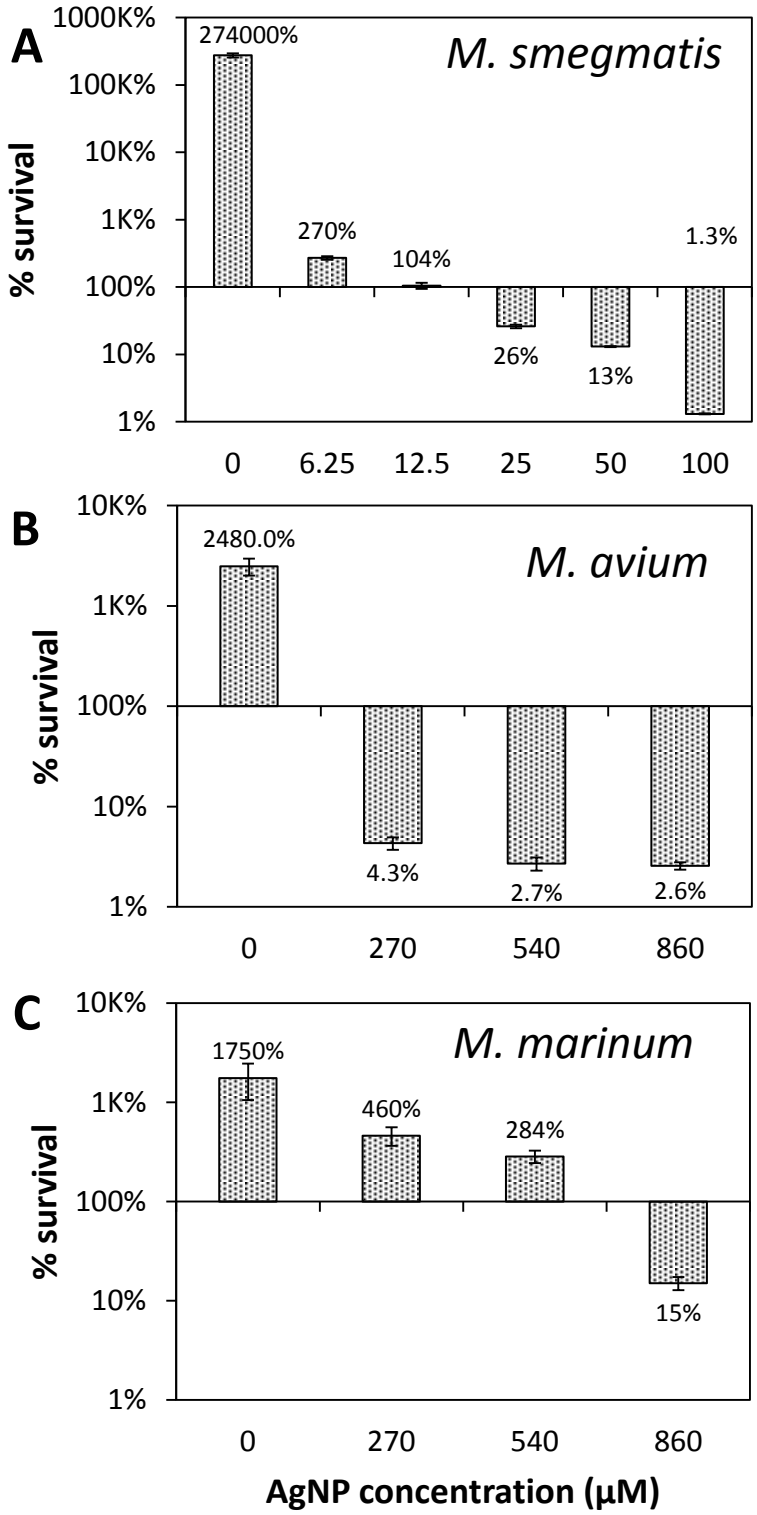

Figure 24: Percent survival of (A) *M. smegmatis* (B) *M. avium* and (C) *M. marinum* when exposed to various concentrations of silver nanoparticles *in vitro* for 48 hours. Error bars show standard error. N=3.

As with *M. smegmatis*, silver was toxic against *M. avium* (Figure 24b). *M. avium* did not reproduce as quickly in the unchallenged negative control, growing 2480% in 48 hours. Still, AgNPs inhibited growth of the mycobacteria. *M. avium* was less susceptible than *M. smegmatis*, requiring a significantly higher concentration (270 µM) to kill more than 95% of the inoculated bacteria. AgNP was completely bactericidal above 1 mM concentration.

M. marinum (Figure 24c) was tolerant to concentrations of AgNP that were inhibitory or lethal against *M. smegmatis* and *M. avium*. *M. marinum* grew 284% in culture with 540 µM AgNP. This concentration was lethal against *M. smegmatis* and reduced *M. avium* by 97.3%. AgNP was bactericidal for *M. marinum* at 860 µM, reducing the inoculating load by 85%.

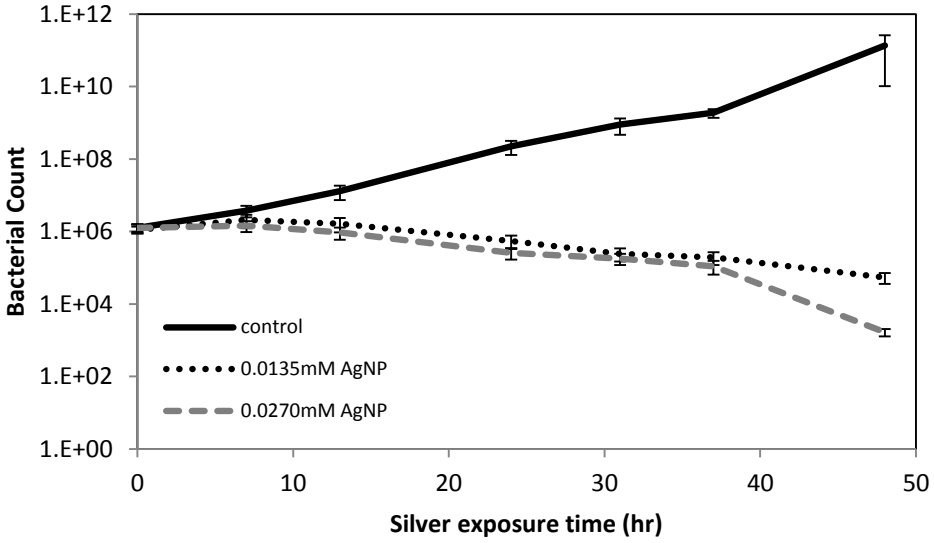

Figure 25: The bacterial count of *M. smegmatis* declines based on the amount of time exposed to silver nanoparticles while the negative control grows exponentially. Error bars show standard error.

M. smegmatis was also exposed to two concentrations of silver and bacteria counts were measured as a function of exposure time for periods up to 48 hours compared to a control with no silver. The results are illustrated in Figure 25. At zero hours (plating bacteria immediately after exposure) these low concentrations of silver do not inhibit bacterial growth. However, over time the control continues to grow exponentially (from ~10^6 bacteria initially to ~10^{11} after 48

hours) while bacterial counts of both cultures suspended in media treated with silver nanoparticles diminished throughout the course of the experiment. Prolonged exposure to silver nanoparticles is, as expected, more lethal to cultures of *M. smegmatis*.

It is possible that silver ions may be present in the AgNP nanofluid as a latent constituent of the chemical precursors used during synthesis. In fact, X-ray diffraction of the nanoparticle powder dried from the nanofluid indicated the presence of silver nitrate crystals in addition to pure metallic silver. In order to ensure that the antibacterial effect of silver nanoparticles is not overwhelmed by the effect of latent silver ions the nanofluid was filtered to purify the nanoparticles which were consequently resuspended in deionized water. Figure 26 shows two plates for wild-type *M. smegmatis*, one treated with purified AgNPs and the other with unpurified AgNPs. Dilutions of wild-type *M. smegmatis* and two silver-resistant strains of *M. smegmatis* were plated and cultured. The unpurified nanoparticles are only slightly more effective at killing all three strains of *M. smegmatis*. The slight disparity may be result from a slightly lower concentration of AgNPs in the purified nanofluid since some nanoparticles were lost during purification. The results indicate that the antibacterial effect of AgNPs is not significantly augmented by the presence of a small amount of silver ions from the precursors used in chemical synthesis. Similar tests were not conducted with *M. avium* or *M. marinum*.

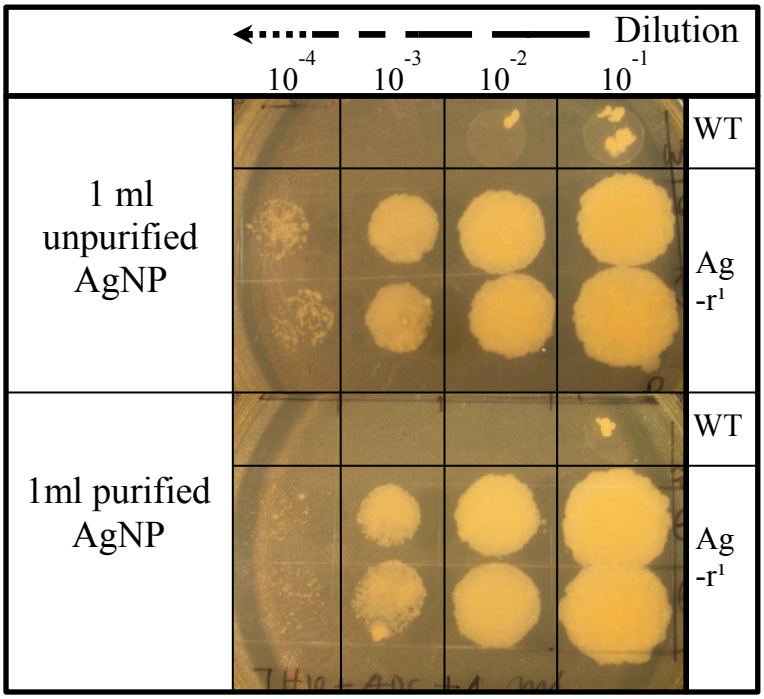

Figure 26: Plates of wild-type and Ag-r[1] smegmatis with purified and unpurified AgNPs

7.2.2 Discussion

This chapter established the toxic effects on silver nanoparticles on mycobacteria. AgNPs had varied efficacy against three species of NTM. *M. smegmatis* was susceptible to AgNPs at 10-fold lower concentrations as compared to *M. avium* or *M. marinum*. The varied response of each species may result from adaptation of each species to silver in their respective environmental niches – the microenvironment in which each species commonly grows in nature. Bacteria exposed to a higher level of silver in their respective environmental niches would naturally evolve genetic adaptations that confer resistance.

M. smegmatis is typically found in soil, where environmental levels of silver are relatively low [3, 37]. The more resistant *M. avium* is a waterborne pathogen whose environmental exposure to silver could be augmented by the presence of aqueous ions [38]. Finally, *M. marinum* is a pathogen of fish, a known center of bioconcentration of silver, which

would enhance silver exposure [39]. Resistance to any toxic metal ion can be attributed to three possible mechanisms: expulsion of toxic ions efflux, segregation into complex compounds and reduction to a less toxic oxidation state. In practical terms, silver cannot be easily reduced by most cells. Complexation is metabolically costly in comparison to efflux. Because of the high metabolic cost, complexation is only efficient for low concentrations of ions. On the other hand, bacteria can be caught in a futile cycle of uptake and efflux so the lower cost of efflux only holds if the toxin is complexed by the larger bacterial population, which is not usually the case. In high concentrations of silver efflux is more successful if the gene for the fast and unspecific chemiosmotic transporter is diminished by mutation, thus reducing uptake [33]. In essence, this is what could have happened to *M. avium* and *M. marinum*. They evolved cell membranes with unusually slow transport across the membrane. Usually, such tolerance results in less viable cells. Both are slower growing than *M. smegmatis*, perhaps in part due to their mutation to resist silver, so they will be easily overgrown by the fast growing *M. smegmatis* when cultured together.

7.3 MUTATION IN ENVIRONMENTAL MYCOBACTERIA IN RESPONSE TO SILVER NANOPARTICLE EXPOSURE

The MC² 155 strain of *M. smegmatis* was cultured in AgNP-enriched agar plates. Surviving colonies were extracted and cultured. These cultures were then re-exposed to silver alongside the MC² 155 strain. The increased resistance to silver was quantified in planktonic experiments as well as by optical density measurements.

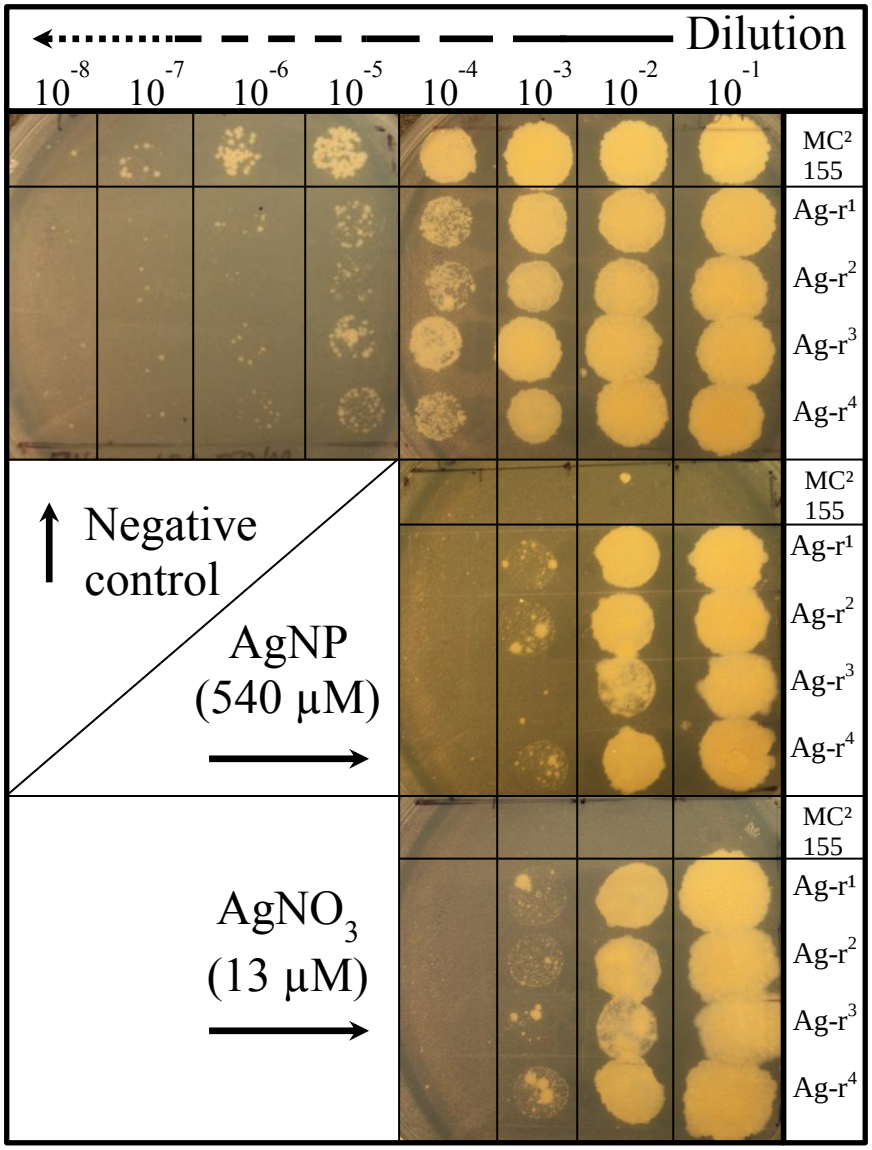

Figure 27: The top row of plates shows 8 dilutions of MC² 155 and 4 mutant strains. The middle plate shows the exposure of all strains to silver nanoparticles (540 µM). The bottom plate shows the exposure all strains to silver nitrate (13 µM). The mutants grow at silver concentrations that cause complete killing of MC² 155.

Figure 27 (top) shows the unfettered growth of all five strains of *M. smegmatis*. The MC² 155 is somewhat more viable than the strains cultured with AgNP. In the plate with AgNPs (540 µM) the wild-type strain was almost completely killed. Likewise, the $AgNO_3$ (13 µM) was lethal to MC² 155. In contrast, each of the mutant strains had surviving colonies at 10^{-4} dilution for both types of silver. To summarize, the mutant strains have been affected by the presence of silver but they show a degree of resistance that is not present in MC² 155.

MC² 155 and Ag-r¹ were re-exposed to AgNP and AgNO3 in planktonic culture. Figure 28 shows that after 48hours Ag-r¹ and MC² 155 both multiplied by approximately 100,000% over the inoculating load of bacteria added to the culture. With AgNP concentration as low as 6.25 µM the MC² 155 strain's growth is severely attenuated while Ag-r¹ was almost unaffected. This trend remains up to 100 µM, when the concentration of AgNP is high enough to kill Ag-r¹.

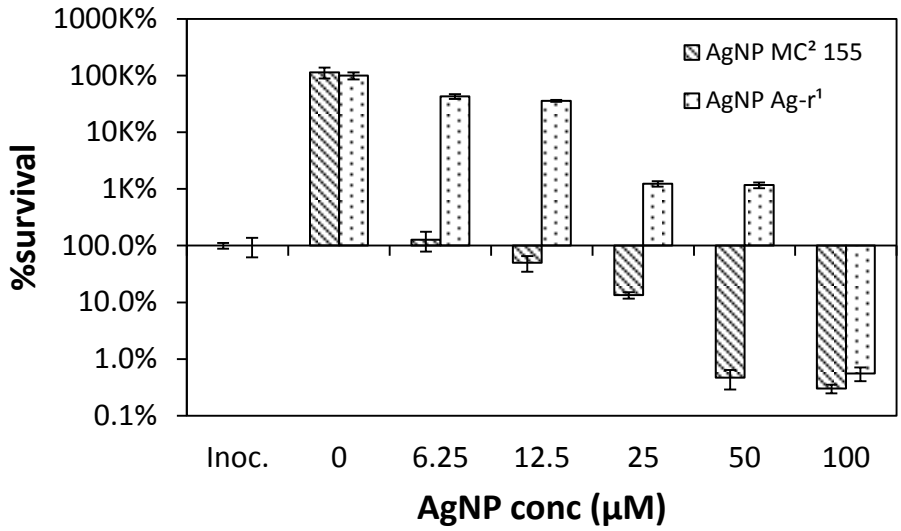

Figure 28: Resistance of Ag-r¹ to AgNP in planktonic culture. SEM error bars. N=3.

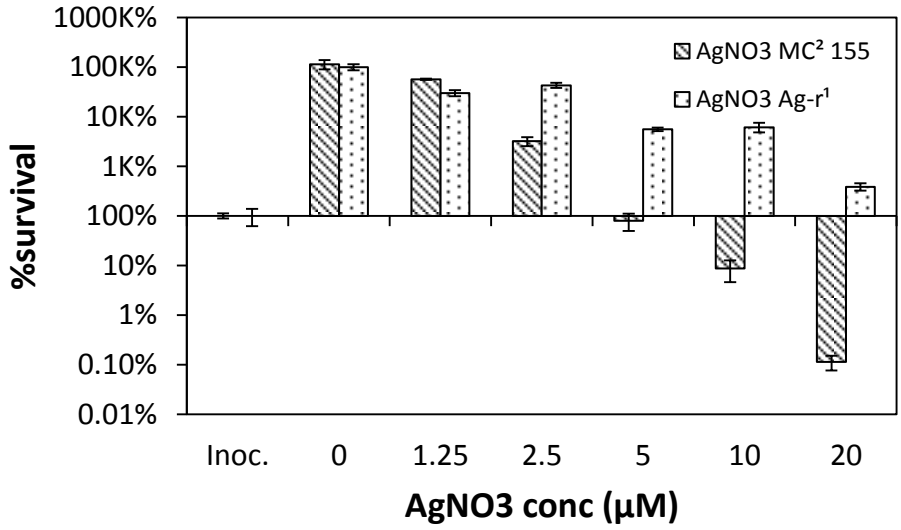

Figure 29: Resistance of Ag-r¹ to $AgNO_3$ in planktonic culture. SEM error bars. N=3.

Interestingly, Ag-r¹ is also resistant to $AgNO_3$ as shown in Figure 29. Concentrations above 2.5 µM were significantly more toxic to the unmodified MC² 155 when compared to Ag-r¹. Even 20 µM $AgNO_3$ did not reduce Ag-r¹ below the bacterial count of the inoculating load.

Additionally, the optical densities (OD) of planktonic cultures of MC² 155 and Ag-r¹ were measured over time series. Figure 30 shows that in 20 µM AgNP the OD of Ag-r¹ grew exponentially after approximately 24 hours. Ag-r¹ also grew exponentially in 2 µM $AgNO_3$. In both cases MC² 155 did not grow and the OD was consistently low up to 58 hours. Both of these experiments showed that Ag-r¹ was resistant to silver when MC² 155 was not.

From logarithmic plots of OD in the exponential growth phase the doubling time was measured. These results are shown in Table 6 and will be discussed below, along with the doubling time of Ag-r¹ and MC² 155 cultured with other toxic metal ions.

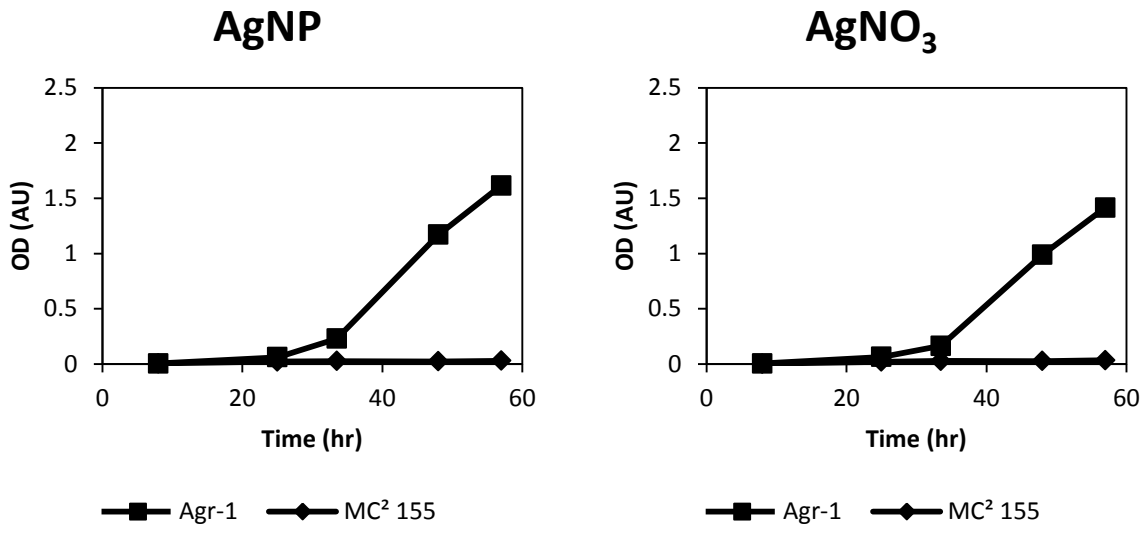

Figure 30: Optical density of MC² 155 and Ag-r¹ with (left) AgNP (20 µM) and (right) $AgNO_3$ (2 µM)

The mutation in MC² 155 that caused silver resistance in Ag-r¹ may also have induced resistance to antibiotics. The susceptibility of Ag-r¹ to isoniazid (INH) was observed by measuring the optical density of cultures with a series of concentrations of the antibiotic. OD

values were used to calculate survival percentage and the results are shown in Figure 31. The OD of each strain of bacteria with cultured in media without INH was fixed at 100%. At low concentrations of INH there was no effect on either strain. In the range 1.25-5 µg/ml MC² 155 is attenuated while Ag-r¹ is relatively unaffected. For example at 2.5 µg/ml INH Ag-r¹ grew to 78.6% of the negative control culture and MC² 155 grew only 4.1%. Above 5 µg/ml the antibiotic was effective against both strains. These results indicate that at least the minimum inhibitory concentration of INH is 4 times higher for Ag-r¹ than for MC² 155. The silver resistant strain is also antibiotic resistant.

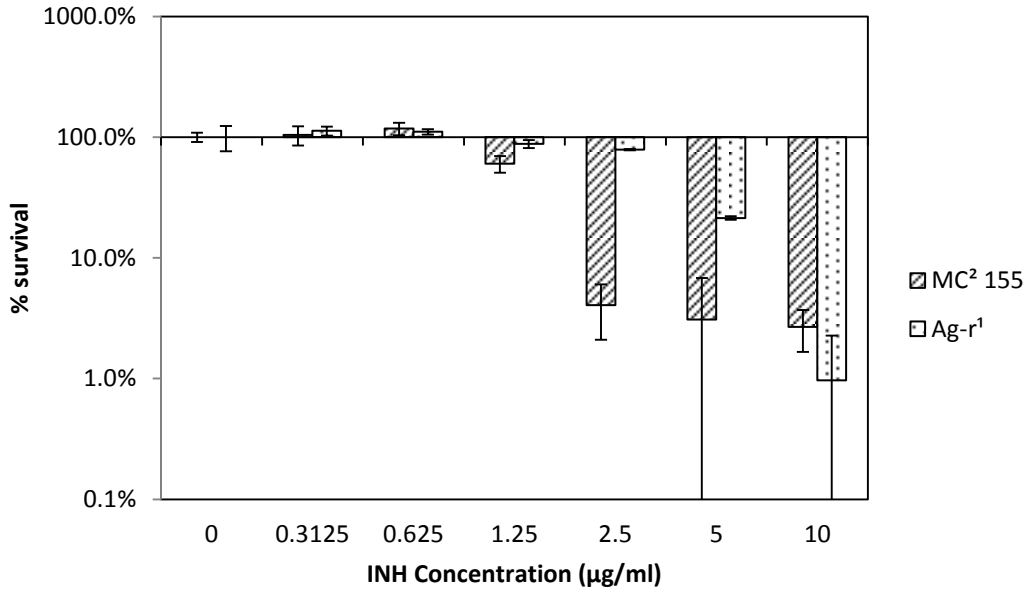

Figure 31: Susceptibility of MC² 155 and Ag-r¹ to antibiotic INH

Finally, Ag-r[1] susceptibility to other toxic metal ions was measured in planktonic culture. Survival percentage was calculated from the CFU of MC[2] 155 and Ag-r[1] cultured with a range of concentrations of CuSO4, $ZnSO_4$, $CoCl_2$, and $CaCl_2$. See Figure 32.

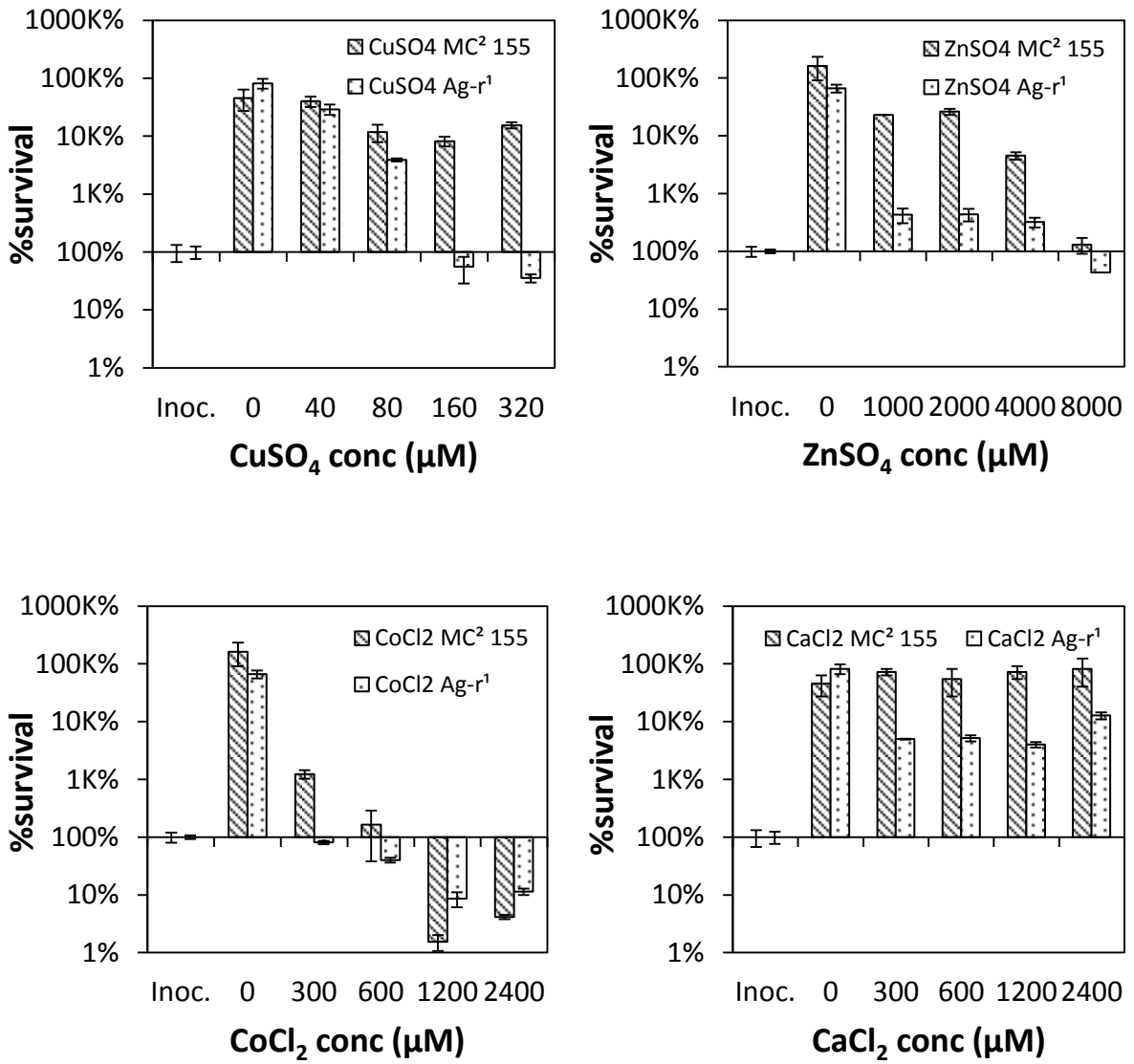

Figure 32: Survival percentages of MC[2] 155 and Ag-r[1] when grown in planktonic culture with CuSO4, $ZnSO_4$, $CoCl_2$, and $CaCl_2$

OD was measured for select concentrations of CuSO4 and $ZnSO_4$ over a time series. From the plots shown in Figure 33 the doubling time of the bacteria in the given growth medium was calculated. Doubling times were compared for both types of silver as well.

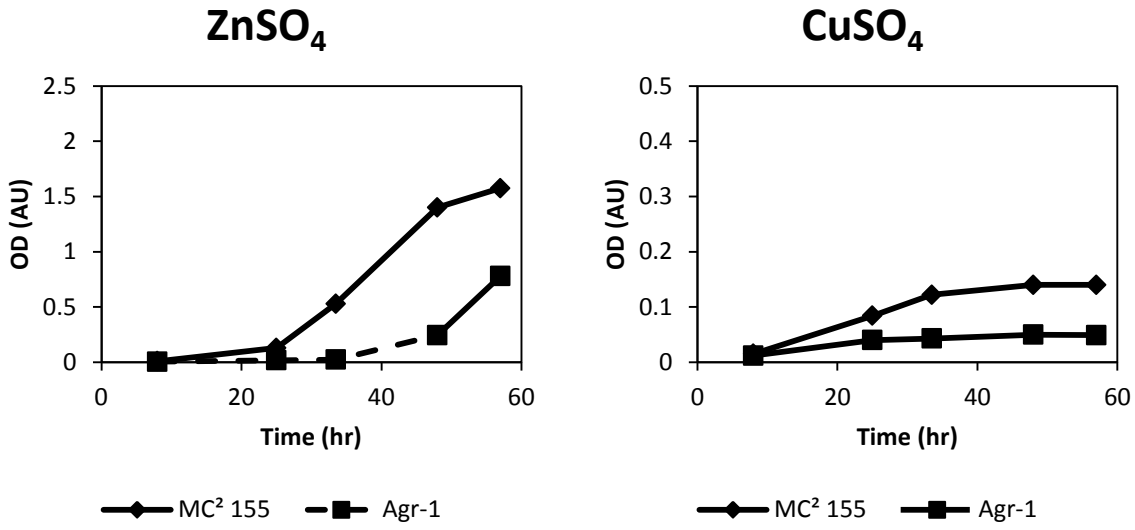

Figure 33: Optical density of MC² 155 and Ag-r¹ with (left) $ZnSO_4$ (1 mM) and (right) $CuSO_4$ (250 µM)

Table 6 shows that MC² 155 and Ag-r¹ had doubling times of 7.4 and 7.7, respectively. The final column of the table shows the growth advantage of Ag-r¹. This was calculated by dividing the doubling time of MC² 155 by the doubling time of Ag-r¹. When this number is greater than 1 Ag-r¹ grows faster than MC² 155 and when it is less than 1 the inverse. The mutant Ag-r¹ strain had a significant growth advantage in both AgNP and $AgNO_3$; however, Ag-r¹ has a growth disadvantage when cultured in $ZnSO_4$ or $CuSO_4$.

Table 6: Doubling times of MC² 155 and Ag-r¹ cultured with toxic metals

	MC² 155	Ag-r¹	Ag-r¹ growth advantage
Control	7.4	7.7	0.96
AgNP 20µM	23.5	10.0	2.34
$AgNO_3$ 2µM	14.8	11.5	1.28
$ZnSO_4$ 1mM	10.0	25.9	0.39
$CuSO_4$ 250µM	18.8	30.1	0.62

The exact mechanism of antibacterial action of silver nanoparticle on mycobacteria and the nature of the genetic changes that confer resistance are still unclear. The genetic studies needed to ascertain genetic changes are beyond the scope of this work. One hypothesis is that the mutation has affected transport across the cell wall, effectively denying access to bactericidal silver. As a test of this hypothesis the silver-resistant mutants were investigated for core resistance to other toxic metals like copper, zinc, etc. Ag-r[1] was did not gain resistance to $CoCl_2$ or $CaCl_2$ and was actually more susceptible to $CuSO_4$ and $ZnSO_4$. However, the MIC of antibiotic INH was significantly higher for Ag-r[1] than for MC[2] 155.

Interestingly, the mutation that led to silver and antibiotic resistance of Ag-r[1] did not significantly impact the doubling time of bacterial cultures under normal conditions. Usually, mutation exacts a metabolic cost that slows bacterial growth. Mutants usually do not survive long because they do not grow as quickly as unmodified strains and thus cannot compete for nutrition. However, in this case Ag-r[1] was highly resistant to silver and otherwise unchanged. Environmental bacteria could develop resistance to silver and a broad spectrum of antibiotics if AgNPs are introduced into their environment in sufficient number.

This work will help to illuminate the antibacterial mechanism of silver. As described above the antibacterial mechanism is complex, multi-faceted and not well understood. In this study environmental mycobacteria that were exposed to silver in the form of nanoparticles were subsequently resistant to silver ions. This result implies that at least in part nanoparticles serve merely as a source for silver ions, which subsequently kill bacteria. If this is the case, antibacterial efficacy will be highly impacted by available surface area and, implicitly, particle size. However, the available lifetime will also be limited by particle size via total volume of silver. Limitations may be imposed on optimum nanoparticle diameter for antibacterial activity

by striking a balance between ion release and volume. To do this, one would first need to study ion release from AgNPs.

7.4 SILVER NANOPARTICLE COATINGS BY VCD

7.4.1 AgNP characteristics measured by TEM and DLS

The silver nanoparticles used in this study are a commercially available variety (Collargol, Argenol Laboratories, Spain), designed to be fully dispersible in water. The particles are coated with a proprietary polymer dispersant that contains caseine, a common protein in milk. The particle size distribution displayed in Figure 34 was measured by the dynamic light scattering method (Horiba Lb-550). The mean diameter of the nanoparticles is 63 ± 3.6 nm.

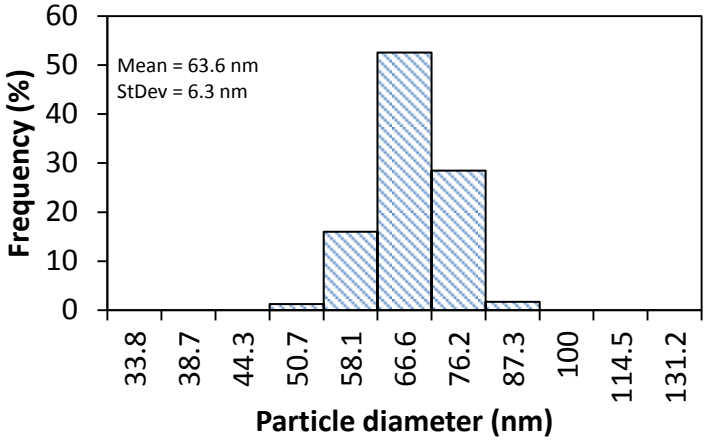

Figure 34: The particle size distribution of the silver measured in aqueous suspension using DLS.

The average particle size was also measured from TEM (JEOL 200CX) images shown in Figure 35. The TEM samples were prepared using a droplet of silver nanofluid (0.22 g/l) which was dried on a copper grid in air. The morphology of the particles is equiaxed and selected area diffraction confirmed that the particles are metallic silver. The nanoparticles were mixed in

deionized water and dispersion was aided through high energy ultrasonication for 30 minutes. Particle size was measured from the images shown in Figure 35 by applying binary threshold and particle analysis algorithms in ImageJ. The mean particle diameter was 21.7 nm and the standard deviation was 20.8 nm, which is consistent with values reported in the literature for nanoparticles from the same manufacturer [134]. The difference between the diameters found by DLS and by TEM is likely due to formation of casein micelles which smaller nanoparticles attach to. It could also result from simple particle aggregation. Neither was explicitly observed in TEM images.

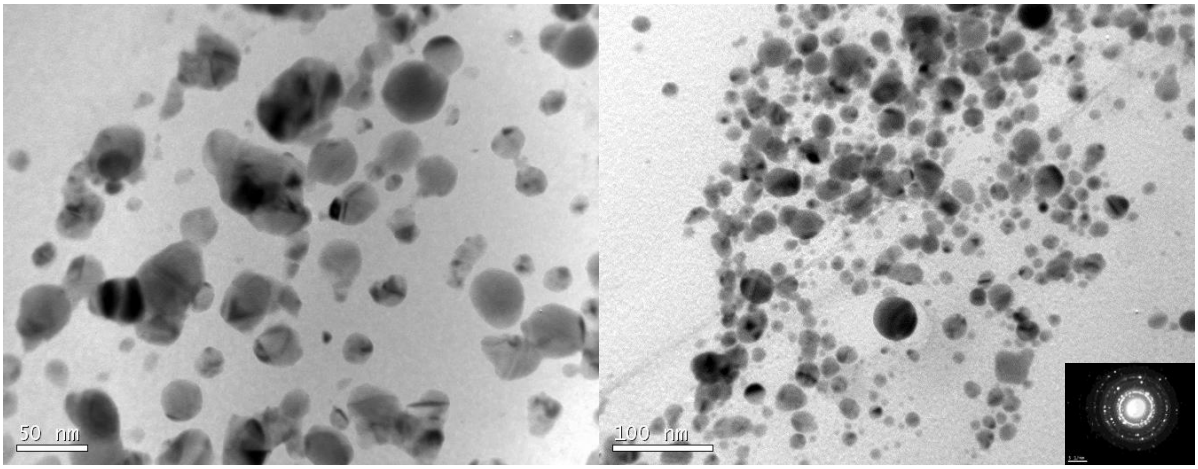

Figure 35: TEM of commercial AgNPs in bright field mode. Selected area diffraction (inset) confirmed these particles are metallic silver.

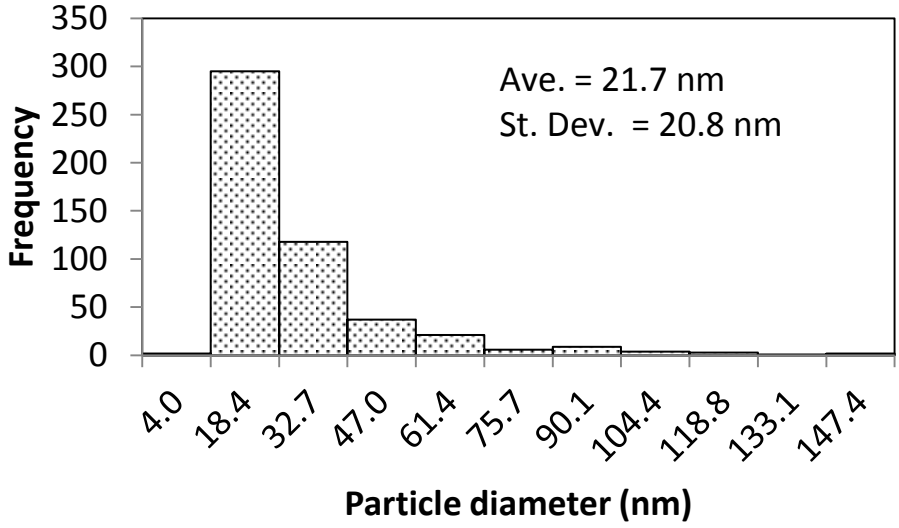

Figure 36: Distribution ofAgNP diameter as measured from TEM images.

7.4.2 Contact wetting angle of RCA cleaned Si wafers

Silicon wafer samples were cut and cleaned by the RCA method described in section 6.4.3. The contact angle of deionized water and three concentrations of silver nanofluid was measured over the course of 6 says after the cleaning process. Contact angle was measured for sessile drops on a drop shape analyzer (Kruss DSA 100). The concentrations of AgNPs were 0.22 g/l, 4.4 g/l and 22 g/l. As indicated in Figure 37, all the wafers were hydrophilic with all three nanofluids with contact angle 7-17° at one hour and it is likely that a thermal oxide layer had not yet formed.

At around 6 hours the contact angle began to rise. This change occurred at the same time for each concentration of nanofluid. The contact angle continued to rise to more than 30 degrees 144 hours. After 10 hours a clear trend emerged with contact angle inversely proportional to AgNP concentration. The 22 g/l nanofluid had lower contact angles at all times. A vertical line was added to the graph at 48 hours, the time at which nanoparticles were deposited by VCD as described in the next section.

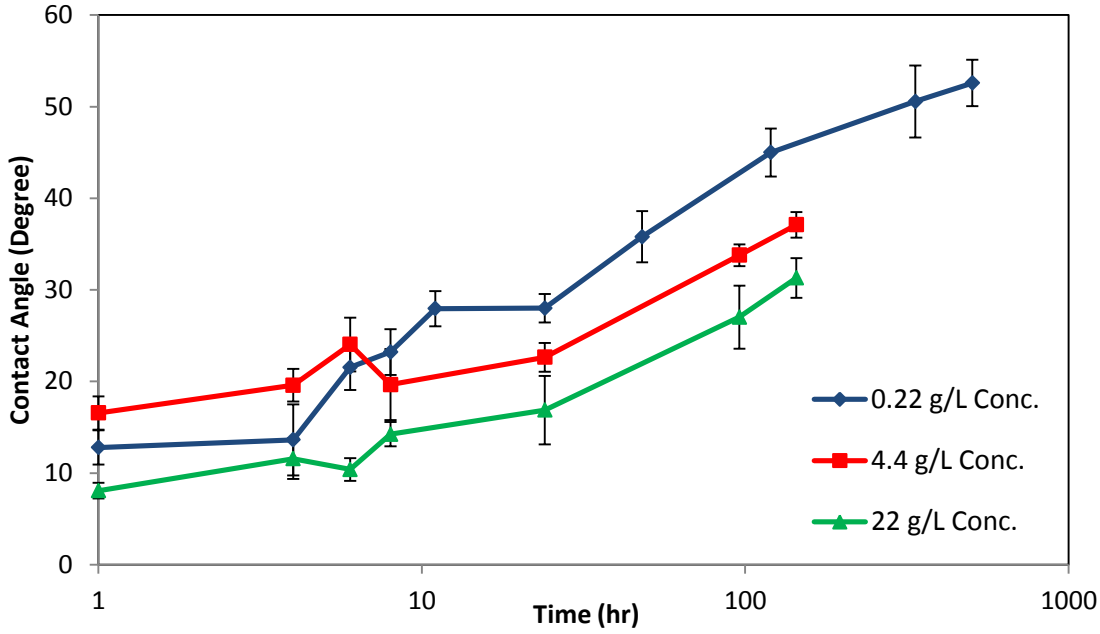

Figure 37: The evolution of contact angle of a RCA etched silicon substrates with time for 3 concentrations of silver nanofluid (0.22, 4.4, and 22 g/l)

Nanoparticles change the contact angle of water with RCA etched substrates. After a few hours the relationship is inversely proportional. The decline in contact angle could result from an attraction between the nanoparticles and the silicon surface. In the literature one study examined the effect of nanoparticles on concentration and found that the particles were directed to the surface, where they changed the interfacial force between the substrate and the nanofluid [147]. However, this effect is not expected here because of the electrostatic repulsion between the particles and the surface. Contact angle can also be changed by ordering of particles on the surface of the drop. This phenomenon has been observed with larger particles but not with nanoparticles [147]. Casein, which is used to aid nanoparticle dispersal, could cause the lower contact angle that has been observed. Casein micelles have a hydrophilic surface. As particles are deposited at the drop's edge they could form a localized zone which is more hydrophilic than the underlying substrate.

The data collected in this experiment was used to calculate areal coverage during VCD. As shown in Figure 41 below, the contact angle can have a significant effect on the areal coverage of a VCD film. Throughout the course of deposition experiments the substrates were prepared approximately 48 hours before beginning deposition so the contact angle would be held at approximately 25-30 degrees. In future experiments the functional dependence of areal coverage on contact angle could be investigated.

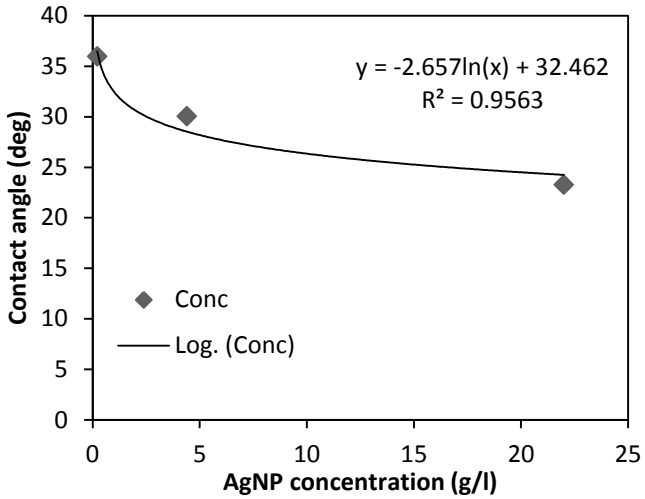

Figure 38: Contact angle of AgNP fluids on Si wafer at 48 hours after RCA clean. In the range of experimental concentrations (2.2-13.2 g/l) contact angle ranges from 25-30°.

7.4.3 Theoretical calculations of areal coverage of AgNP deposited by VCD

Diao's theory of VCD was used to predict areal coverage for the chosen experimental conditions. Combining equations (2) and (3) the areal coverage for submonolayer coverage is

(8) $$N_{submono} = \frac{Kk_BT\theta}{6\pi\eta r} \cdot \frac{C^2}{v}$$

The contact angle, θ, which is to be discussed in detail above, can be held at approximately 25 - 30 degrees in the experimental concentration range of 2.2-13.2 g/l. Boltzmann's constant is $1.38\text{x}10^{-23}\ \frac{m^2 kg}{s^2 K}$. The experiments were carried out at room temperature, 294 K. The radius of the

particles, as measured by dynamic light scattering (Horiba LB-550) is 64±6nm. However, the diameter measured using TEM images was 12.9±1.6 nm. Both values were compared and ultimately the particle size from DLS was used for theoretical calculations. The dynamic viscosity of water at 20°C is $1.002 \times 10^{-3}\ \frac{Ns}{m^2}$. A conversion factor must be applied to change N from mass density $\left(\frac{kg}{m^2}\right)$ to areal coverage (%). To do this some assumptions must be made about the nature of the resulting deposition. It is assumed that the particles on the surface are monodispersed (i.e. they do not form multilayers) and close-packed (i.e. particles cover only 90.7% of the area they occupy). Given these assumptions, the number of particles required to cover one square meter is 7.04×10^{13} and the mass density of 100% coverage is 1.02×10^{-4} kg/m^2. Thus, dividing the mass density by 1.02×10^{-4} kg/m^2 will result in the areal density. Finally, the attachment probability, K, is the only unknown parameter. It is dependent on the properties of the fluid, the particles, and the surface. Diao, et al. determined empirically that $0.6<K<0.8$ and these limits were assumed in the following calculations [115].

When the theoretical results from equation (8) exceeded 100% (i.e. multilayer coverage) equation (4) was used instead, which is presented here in detail.

(9) $$N_{multilayer} = \frac{\psi k_B T \theta}{6\pi\eta r} \cdot \frac{C}{v} + N_{mono}$$

Dividing both sides of this equation by the mass density will again give the areal coverage percentages. In that case, N_{mono} is 1 and values between 1 and 2 represent an incomplete second layer. Obviously, each successive complete monolayer is another integer.

The theoretical areal coverage was calculated and plotted in Figure 39 and Figure 40 using the experimental conditions that were used. Note in Figure 39 that the functional dependency of areal coverage on $1/v$ is linear for the three lowest concentrations because the

areal coverage is exclusively below 100%. Also the highest concentration is linear because areal coverage is exclusively above 100%. That a 22 g/l nanofluid always results in greater than monolayer coverage for this regime of speed is typical for experimental results. Also, the expected deposition for the standard concentration of nanofluid (0.22 g/L) is negligible (≪1%), which is consistent with experimental observations.

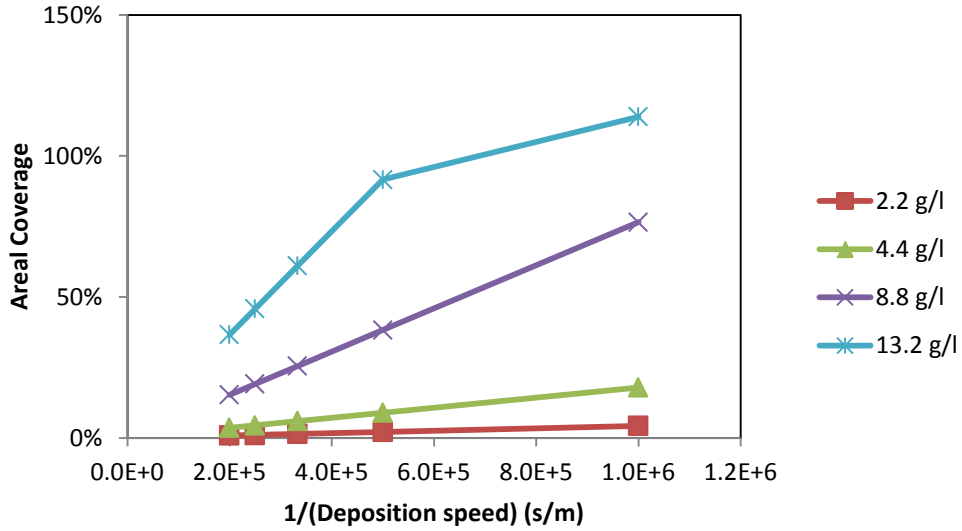

Figure 39: Theoretical calculations of areal coverage for various concentrations of nanofluid (ψ = 0.7)

In Figure 40, note that the relationship of areal coverage to concentration is quadratic up to 100% and then linear thereafter. The deposition of particles is more difficult for multiple layers. These data were compared to experimental results and this can be seen in section 7.4.5.

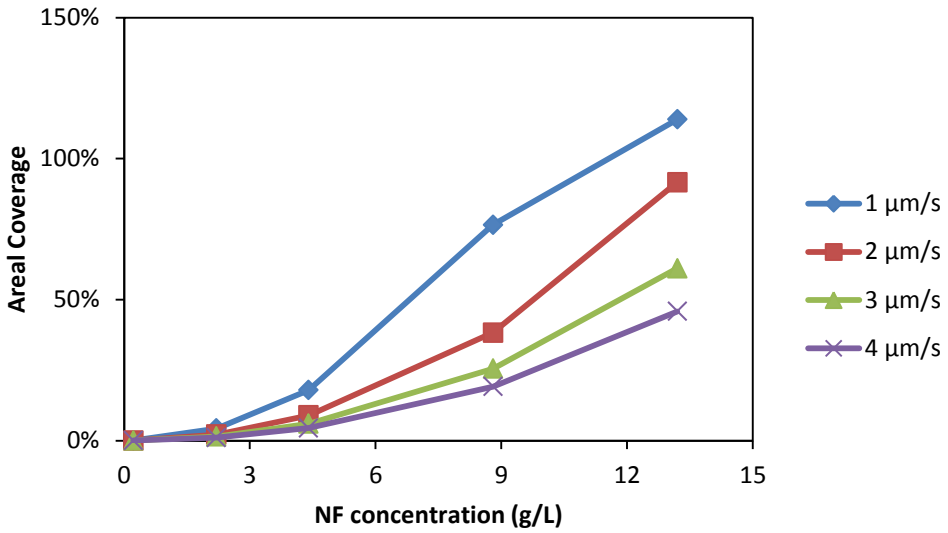

Figure 40: Theoretical calculations of areal coverage for various deposition speeds

As discussed above, Diao's theory of VCD states that areal density of deposited particles is linearly related to the contact angle of the fluid with the surface. VCD is most effective with hydrophilic surfaces where the contact angle is less than 60 degrees. Variation of contact angle of the etched silicon can significantly impact the overall deposition of nanoparticles. See Figure 41.

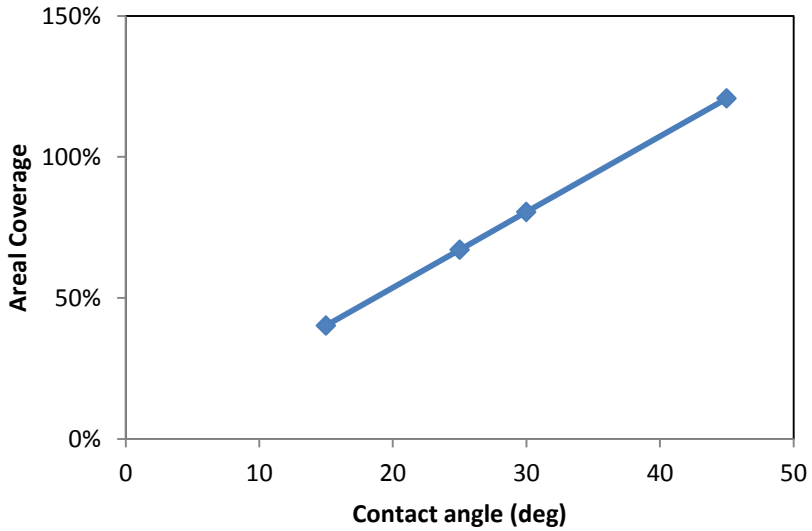

Figure 41: Effect of contact angle on areal coverage of nanoparticle deposition by VCD. Values shown for 1 µm/s, 8.8 g/l.

Finally, the effect of particle size on areal coverage was considered. The two methods used to measure particle size yielded different values: 64 nm for DLS and 12.9 nm for TEM.

Inserting the lower particle diameter into equations (8) and (9) yielded theoretical areal coverage shown in Figure 42. Areal coverage is increased dramatically when particle size is lowered, owing perhaps to the fact that for a given concentration (in volume fraction) the number of particles will be dramatically higher if particles are smaller. Also, smaller particles may be more easily trapped in the meniscus region. Ultimately, theoretical calculations more closely correlated to the theory when the larger particle size was used. It is a reasonable assumption that the small particles seen in TEM are agglomerated around casein micelles and form a structure with 64 nm diameter.

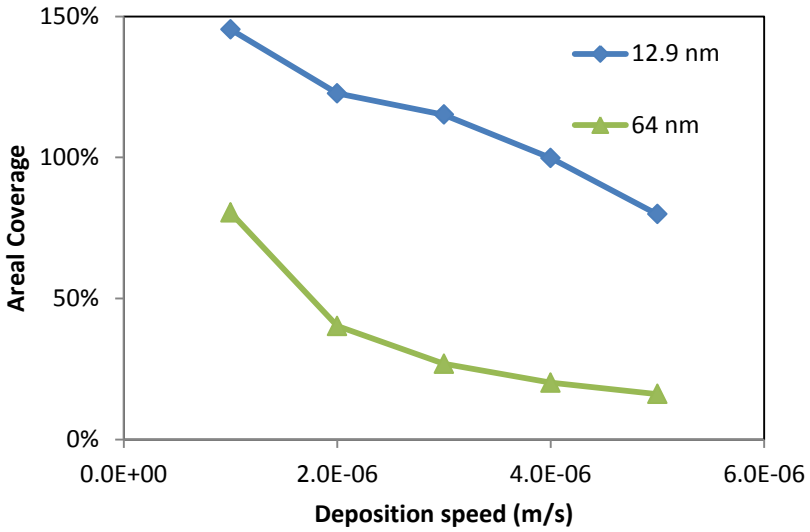

Figure 42: Effect of AgNP size on areal coverage in VCD

7.4.4 Deposition of silver nanoparticles

AgNPs were deposited on etched silicon wafers by VCD. Again, the advantage of depositing by VCD is that the same particle used in experiments with planktonic bacteria. The morphology of the silver coating deposited by VCD is characterized by horizontal lines. This morphology is characteristic of a stick-slip mechanism that is often seen in colloidal crystals and is sometimes known as the "coffee stain phenomenon." [148]. While the thickness, separation

and continuity of stick-slip deposition lines varied they were always present in all depositions in this study (see Figure 43). Within deposition lines AgNPs are densely packed in general. There is some evidence of particle aggregation, as seen in Figure 44, which shows two SEM micrographs of AgNPs on the substrate surface in a sparsely packed region of the coating.

Horizontal lines of nanoparticles have been deposited with discontinuous VCD [149]. In that technique the substrate is held in one position until a line of particles has deposited at the meniscus. The substrate is then moved to a new position quickly so nanoparticles are not deposited during motion. Similar deposition lines could occur if the substrate is lifted using a stepper motor with a large step size. The dip coater used has a step size of 1 μm. By comparison, the deposition lines are separated by 83-200 μm.

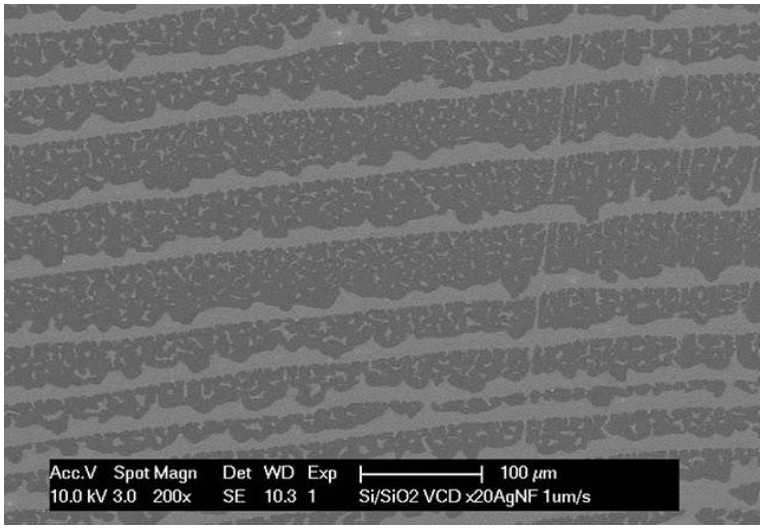

Figure 43: Example of the morphology of a nanoparticle film deposited by VCD

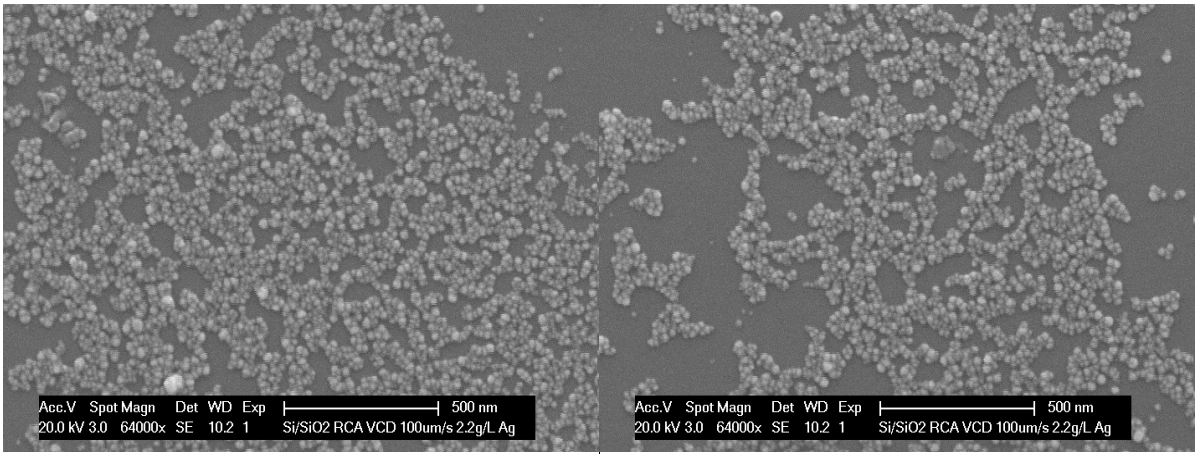

Figure 44: High magnification SEM images of AgNP coating in sparsely packed region

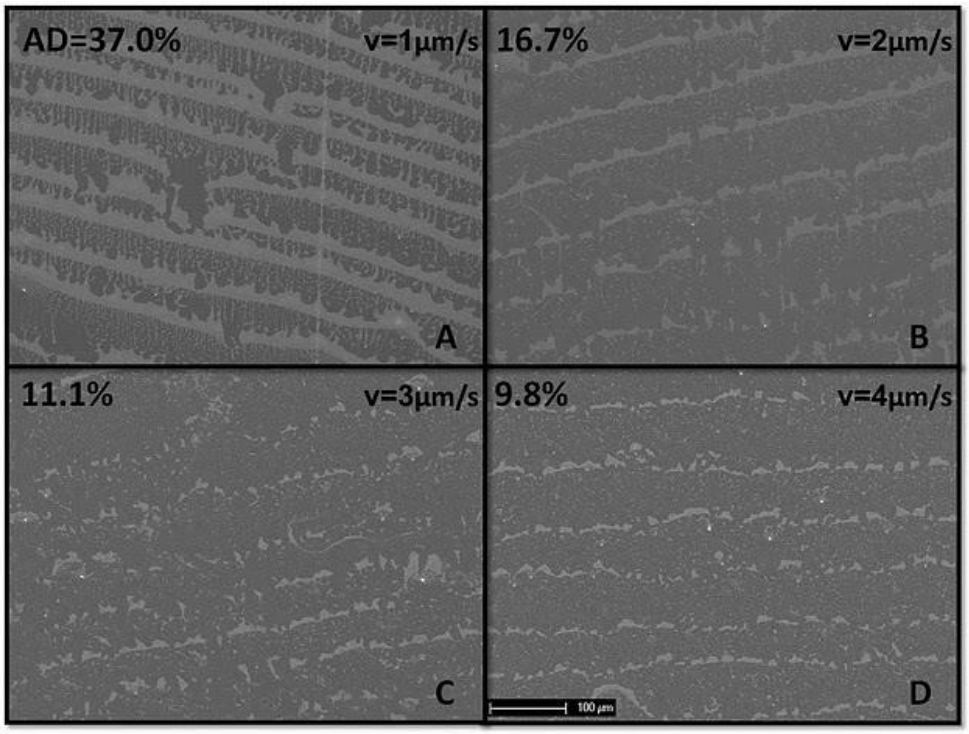

Figure 45: Effect of deposition speed on areal coverage and morphology of nanoparticle films deposited by VCD at A) 1µm/s B) 2µm/s C) 3µm/s D) 4µm/s. Concentration is 4.4 g/l.

The effect of velocity is seen in Figure 45. The characteristic lines are thinner and more spread out. As the velocity increases from 1 to 4 µm/s the areal coverage decreases from 37.0% to 9.8%. This trend is consistent with the inverse relationship predicted by Diao's theory even though it does not accommodate the stick-slip mechanism. The images shown in the figure are representative samples. The percentage shown for each condition is an average over 10 images.

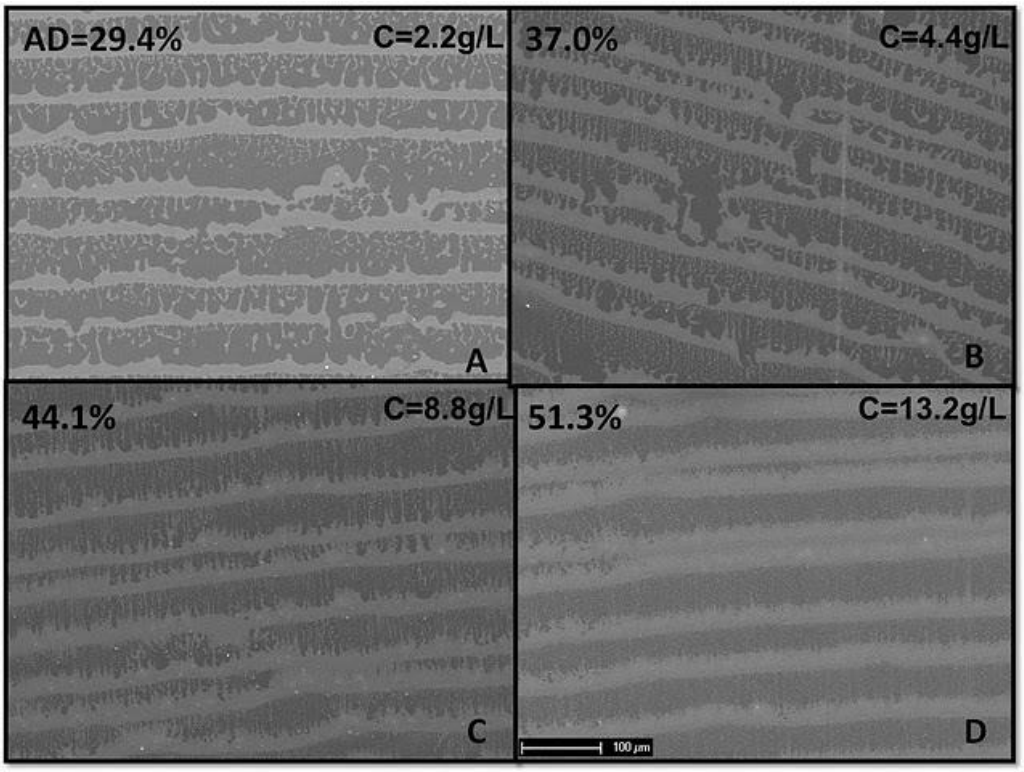

Figure 46: Effect of nanofluid concentration on areal coverage and morphology of nanoparticle films deposited by VCD at A) 2.2 g/l B) 4.4 g/l C) 8.8 g/l D) 13.2 g/l. Speed is 1µm/s.

Figure 46 shows the relationship between areal coverage and nanofluid concentration. The morphology of the deposition lines changes as they become thicker and more closely spaced. As concentration increases from 2.2 g/l to 13.2 g/l the areal coverage increases from 29.4% to 51.3%. This trend is consistent with the proportional relationship predicted by the theory. Again, the percentages in the figure represent an average over 10 images.

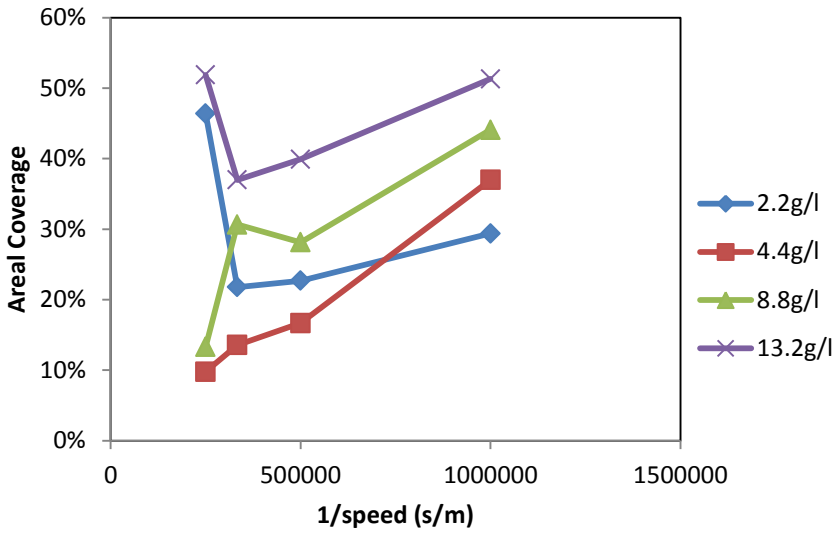

Figure 47: Variation of areal coverage with inverse speed in experimental VCD of silver nanoparticles

Figure 47 shows experimental results for the variation of speed in VCD of silver nanoparticles. There is a generally upward trend for each concentration. However, only the depositions with a concentration of 4.4 g/l showed a well-correlated linear trend. The irregularity of this data at high speeds (left of Figure 47) may indicate a change in the deposition mechanism. As observed in preliminary deposition experiments, high deposition speed leads to classic ring patterns on the surface that indicate separation of small volumes of liquid from the bulk due to the high speed of the moving meniscus. That type of deposition is not VCD.

Figure 48 shows the areal coverage as a function of concentration. Again, there is a general upward trend for most of the data. Since all of the conditions resulted in sub-monolayer coverage the relationship to concentration should be quadratic. It is difficult to ascertain a quadratic trend in the data. Again, the data for the highest speed (4µm/s) is erratic, perhaps owing to a change in deposition mechanism.

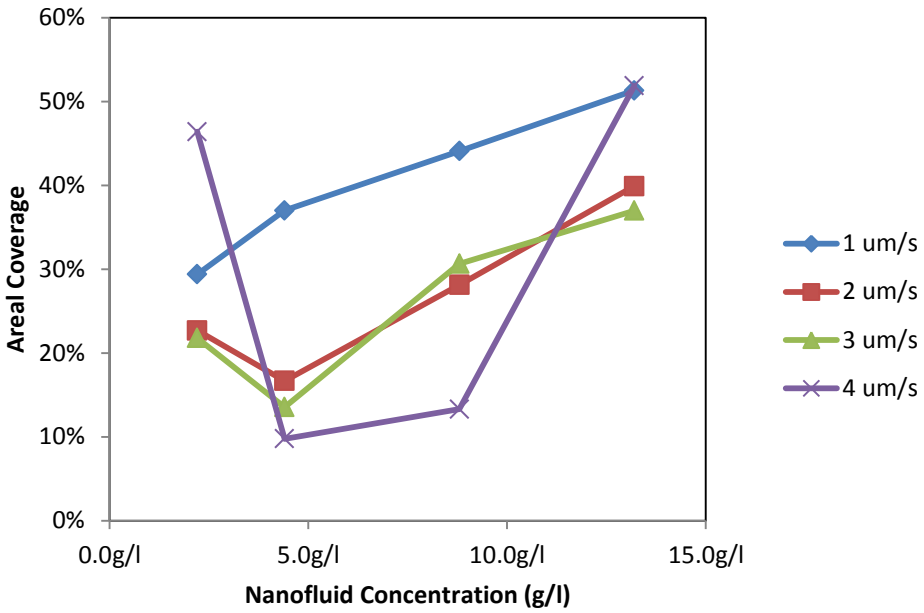

Figure 48: Variation of areal coverage of nanoparticle films deposited by VCD with nanofluid concentration

7.4.5 Comparison of Experimental and Theoretical VCD Results

Experimental data from the previous section were compared to the theoretically calculated results from section 7.4.3. In general, the trends predicted by Diao's theory were correct but the experimental data did not correlate closely the values predicted. The experimental (left) areal coverage was generally lower than the highest values and higher than the lowest predicted by the theory (right) in Figure 49. In Figure 50 data for 4.4 g/l AgNP concentration only are shown. Both the experimental and theoretical values have a linear trend with inverse deposition speed. The attachment affinity assumed for these figures is $\psi = 0.6$.

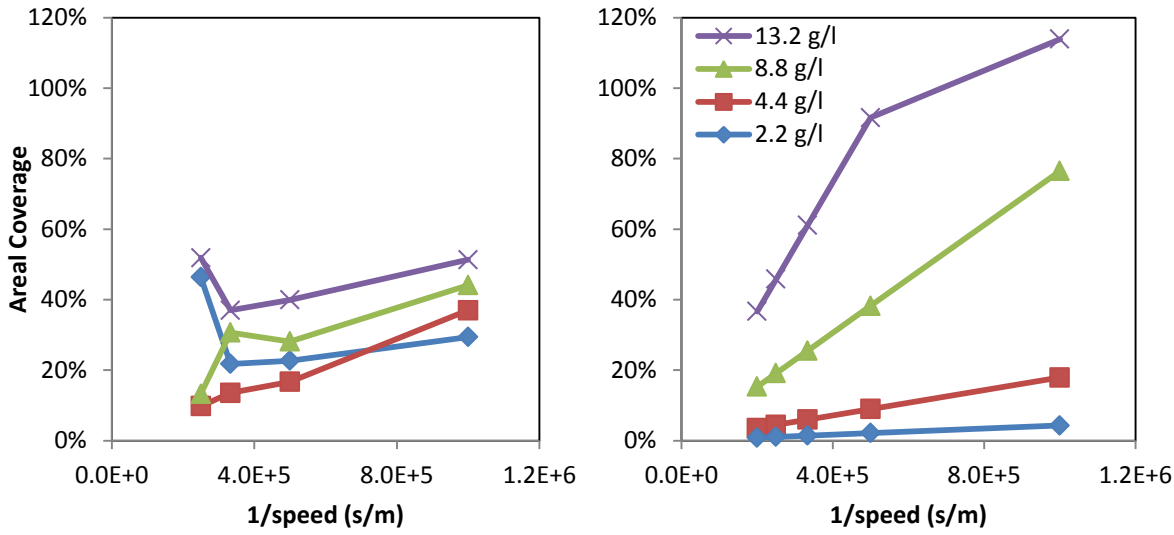

Figure 49: Comparison of experimental (left) and theoretical (right) areal coverage from VCD

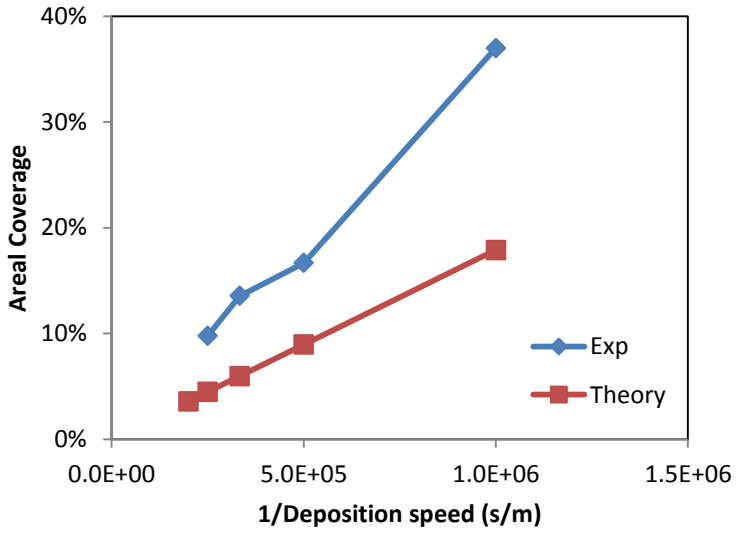

Figure 50: Comparison of experimental and theoretical results for the dependence of areal coverage on inverse speed. Concentration is 4.4 g/l

Figure 51 shows a comparison of the theoretically calculated values for areal coverage and the experimental results. The slope of the trend is only comparable for 4.4 and 8.8 g/l. At the lowest concentration the experimental result is approximately 20% higher than the theoretical prediction. On the other hand, the highest concentration yielded a result that was significantly lower than the predicted value.

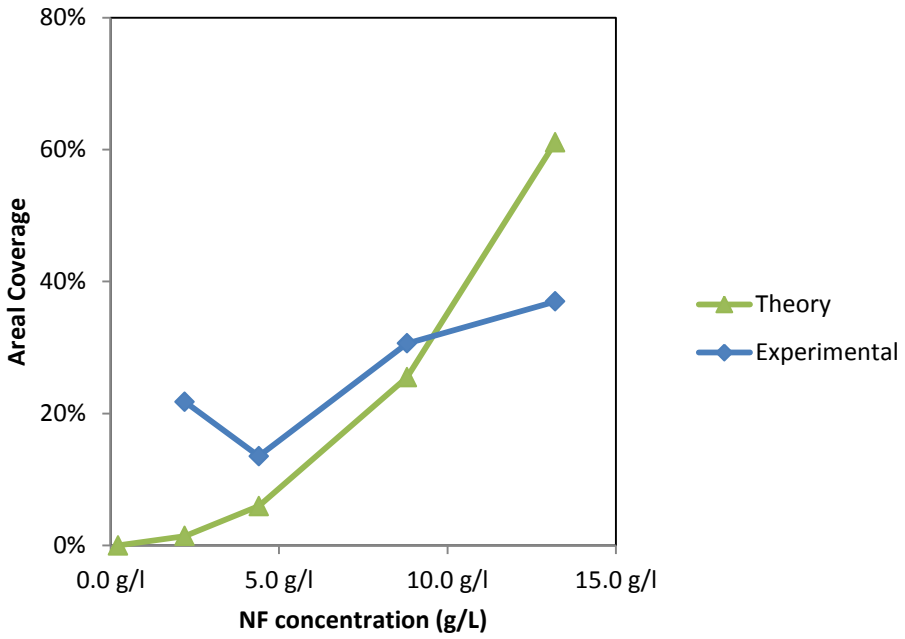

Figure 51: Comparison of theoretical and experimental data for dependence of areal coverage on concentration (speed is 3µm/s)

Although experimental data for areal coverage of VCD coatings did not match Diao's theory, the areal coverage of AgNPs was easily controlled via manipulation of VCD deposition conditions. Specifically, by varying deposition speed between 1 and 5 µm/s and concentration between 2.2 and 13.2 g/l the areal coverage of AgNPs can be varied from 0-50%.

One of the principal reasons that AgNP coatings shown in the experiments above did not match the areal coverage predicted by Diao's theory is the presence of characteristic deposition lines that always appeared perpendicular to the deposition direction. Presence of lines is not predicted by the theory, which favors uniformly dispersed particles. In fact, deposition lines may be a direct result of a stick-slip mechanism that modifies deposition dynamics.

In spite of a modified deposition mechanism, Diao's theory can be used to predict some features of the morphology of deposited lines. Keeping in mind that areal coverage is proportional to nanoparticle concentration (or concentration squared) and inversely proportional

to deposition speed the width and density of lines should also follow these function dependencies. Specifically, the areal density is

$$N = W_l \cdot D_l \tag{10}$$

where N is areal density, W_l is line width, and D_l is line density measured in lines per unit length of the surface. Then line width and line density should be proportional to concentration and inversely proportional to deposition speed.

These functional dependencies were tested by measuring line width and line density in SEM images of AgNP coatings deposited with a range of VCD conditions. As described above these quantities were measured from transformed binary images using a Matlab script. In Figure 52 there are negatively sloped trends for both line width and line density when plotted against deposition speed. This implies an inverse relationship, as predicted. The trends are consistent across a range of concentrations. In general lines were thinner and more spaced with increasing speed.

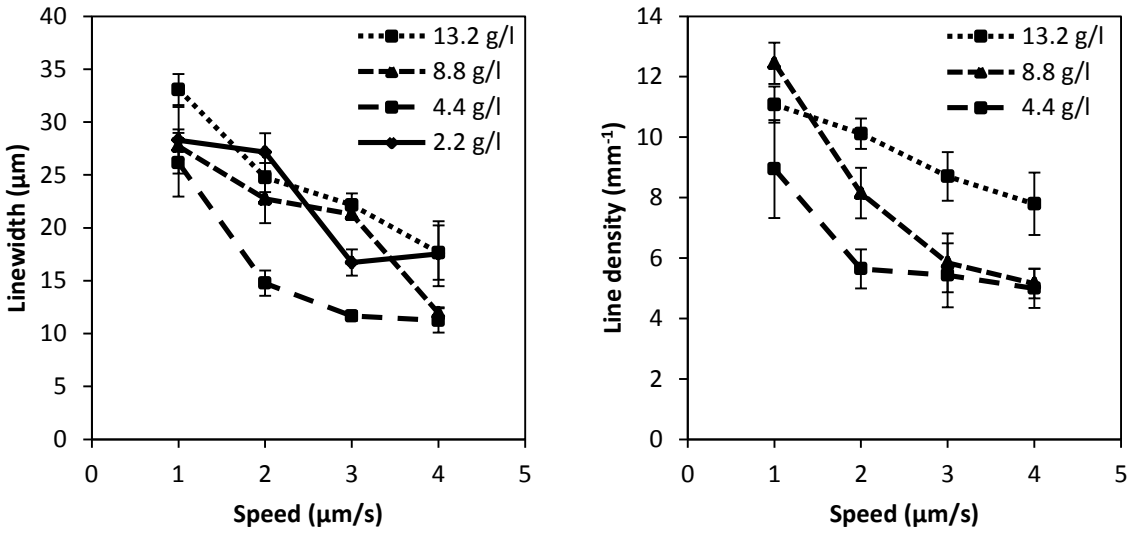

Figure 52: Line width (left) and line density (right) are both inversely proportional to deposition speed across a range of AgNP concentrations. SEM error, N=8.

In Figure 53 the same data are plotted against AgNP concentration. Both line width and line density have positively slopes trends, implying a proportional relationship. Deposition lines became thicker and more closely spaced with increasing AgNP concentration. These observations are consistent with qualitative observations in SEM images. These morphological features may play an important role in the antibacterial or antibiofilm efficacy of AgNP coatings. As discussed above, the first stage of biofilm development is attachment, in which planktonic bacteria land on a surface and attach by excreting extracellular polymeric substance (EPS). It is not clear whether bacteria may more easily attach and replicate on uncoated portions of the sample surface.

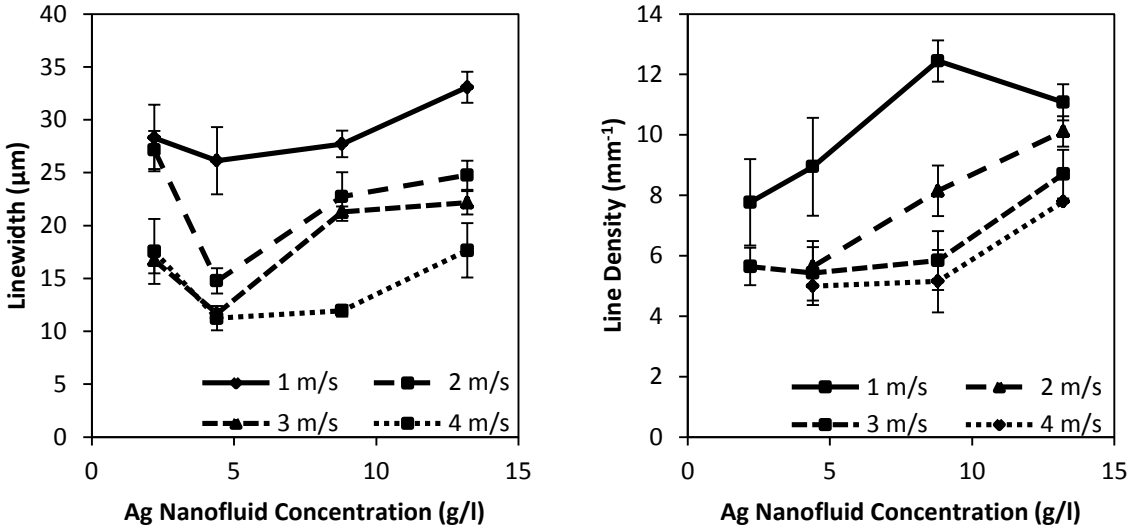

Figure 53: Line width (left) and line density (right) are both generally proportional to AgNP concentration across a range of deposition speeds. SEM error, N=8.

On the other hand, deposited AgNPs may act as a localized source for Ag^+ ions, which inhibit bacterial biofilm growth independently. In that case, AgNP coatings could be optimized to minimize areal coverage as long as the whole surface is protected by the cloud of released silver ions. Clearly, the effectiveness of this ion cloud would depend on the rate of ion release and the spatial distribution of AgNPs. These specific questions may be beyond the scope of this

research. However, morphological control of AgNP coatings has been well established through processing. And the processing techniques and properties evaluated here provide a basis for future research in this area.

7.5 DURABILITY OF AGNP COATINGS DEPOSITED BY VCD

Durability of AgNP coatings deposited by VCD was measured in a flow cell. Samples were imaged by optical microscopy and AFM before and after exposure to flow of 0.06 ml/min deionized water for 72 hours. Durability was quantified by comparing the areal coverage of AgNPs, the thickness of deposited lines and the separation of deposition lines. The morphology of deposited AgNP coatings was also compared in images.

7.5.1 Durability measured by areal coverage from optical microscopy images

Five deposition conditions were chosen with the intention to achieve areal coverage of 10%, 20%, 30%, 40%, and 50%. Five samples were made with each deposition condition and they were divided into sets. Samples were imaged on an optical microscope and the resulting color images were converted into binary black and white by applying a threshold function. Figure 54 shows an example image for the 30% deposition condition and the black and white transformed image. Areal coverage of silver was calculated by divided the area covered by the AgNP coating (white) by the total area of the image. The Si wafer substrate is black.

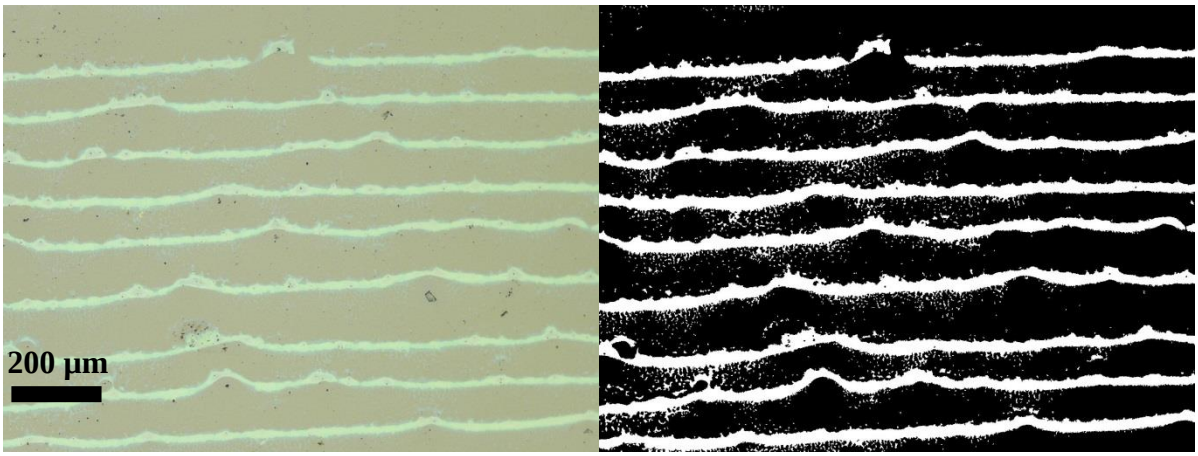

Figure 54: Color and B/W transformed optical image of AgNP coating with ~30% areal coverage

Samples were then subjected to the flow of DI water for 72 hours. Figure 55 shows images of a AgNP coating before and after flow. The loss of AgNPs from the surface is clearly evident in both the color and black and white images. Interestingly, the portions of the AgNP coating that appear to have been removed during flow are the thick areas that are characteristic of the deposition lines created during VCD. Sections of the coating that appear to be thinner, such as the leading and trailing edge of deposition lines were relatively unaffected. Particles deposited in thin layers may attach more firmly because particle aggregates bond more firmly to the substrate surface than each other. Also, the higher profile of thick deposition lines are more subjected to the sheer force of the liquid flow.

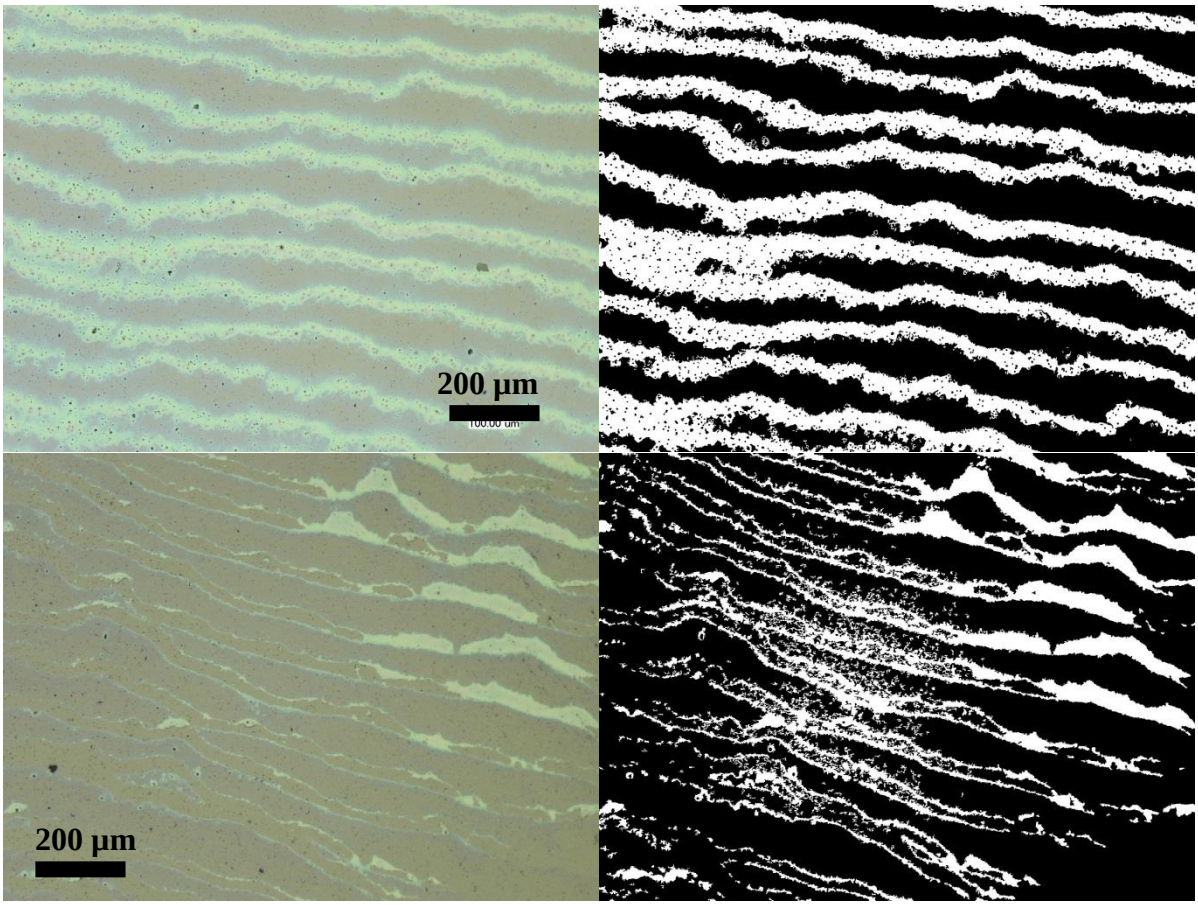

Figure 55: Loss of AgNPs from surface coating ~50% coverage before (top) and after (bottom) flow

Images such as the examples shown in Figure 54and Figure 55 were acquired for all five deposition conditions. The resulting color and black and white images were used to calculate areal coverage before and after flow in a flow cell. Importantly, pre-flow images were taken on the same samples as post-flow images. But the exact same areas of each sample were not selected for imaging. Instead, 10 random areas were selected to acquire a statistically significant mean.

In Figure 56 the areal coverage of all samples is shown before and after flow. First, measured areal coverage percentages were lower than the expected for the 20pct and 40pct samples. This is probably due to some natural variation from sample to sample and the tendency for optical microscopy to underestimate coverage of silver as compared to the method that uses

SEM images. A full comparison of expected and experimental values can be found inTable 7. Several deposition conditions show a significant drop in areal coverage of AgNPs after flow. The highest areal density coating was reduced from 45.2% to just 8.0%. Only the condition nominally referred to as 40pct in the figure did not show a decrease. Interestingly, this deposition condition was the only one to use 4.4 g/l AgNP fluid during VCD. The concentration could influence attachment strength.

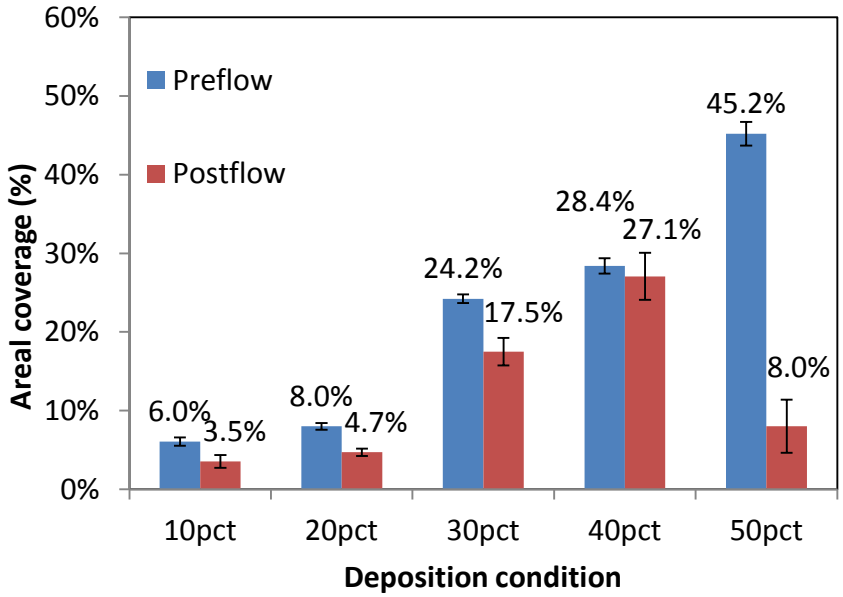

Figure 56: Areal coverage before and after flow cell for various deposition conditions. SEM error bars. N=10.

The decrease in attached AgNPs is troubling because it would leave the surface vulnerable to biofilm growth and also because AgNPs are released into the effluent stream. It is especially startling that such a high proportion of silver was washed from the coating in just 72 hours. Clearly, it would be advantageous to improve durability through processing.

Table 7: Nominal and experimental areal coverage for the deposition conditions for durability experiments

Goal area coverage (also used to name deposition conditions)	Deposition conditions (speed) (AgNP conc.)	Areal coverage (measured by SEM)	Areal coverage (measured by optical microscopy)
10pct	4 µm/s, 2.2 g/l	8.2%	6.0%
20pct	3 µm/s, 2.2 g/l	21.8%	8.0%
30pct	1 µm/s, 2.2 g/l	29.4%	24.2%
40pct	1 µm/s, 4.4 g/l	45.4%	28.4%
50pct	1 µm/s, 13.2 g/l	51.3%	45.2%

Heat treatment was applied to AgNP coatings in an attempt to improve durability. Samples were heated to 200 °C and 500 °C on a hot plate after deposition. Figure 57 shows a comparison of images taken after deposition (pre-flow), after heat treatment to 200 °C, and after flow for 72 hours. Black and white transformed images are also shown below their color counterparts. Heated samples showed a distinct change in color from the lustrous blue seen in the top left of Figure 57. Instead the deposited lines of AgNPs were yellowed. Samples that were heated to 500 °C were noticeably whiter, even to the naked eye. This could have been caused by enhanced oxidation of silver at high temperature.

After heat treatment AgNPs appear to be more durably attached to the surface of the Si wafer substrate as can be seen in the images below. The difference was especially clear for samples with high density AgNP coatings, which lost a significant amount of areal coverage when left untreated. Durability was enhanced at both temperatures.

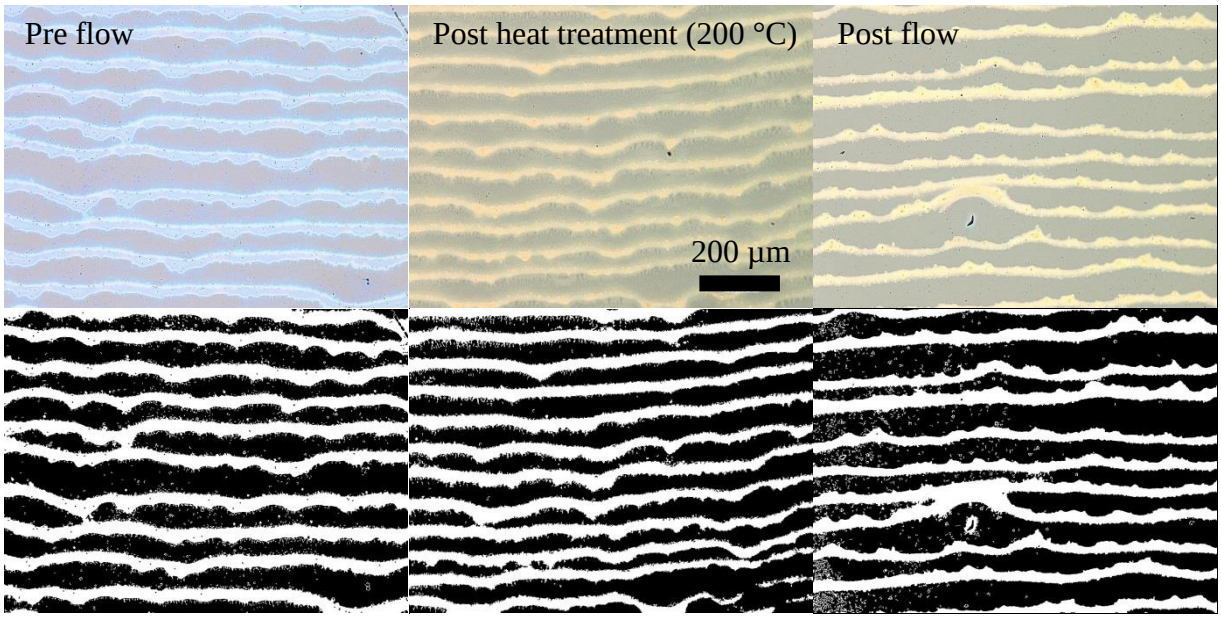

Figure 57: Effect of flow on heat treated AgNP coating. ~50% areal coverage. Lower images are binary threshold of optical images above.

Images from all five deposition conditions were used to calculate areal coverage before and after flow for both 200 °C and 500 °C heat treatments. The full results are plotted in Figure 58 and Figure 59. In general, the areal coverage did not decline after heat treatment or did not decline as much. Comparing post heat treatment areal coverage to post flow coverage the highest density coating fell from 33.2% to 26.6%.

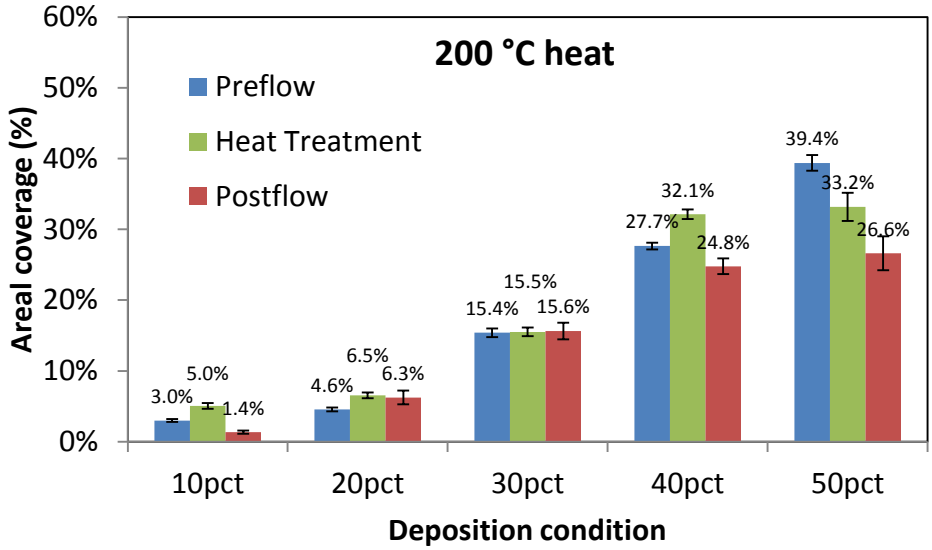

Figure 58: Areal coverage before and after flow cell with 200 °C heat treatment for various deposition conditions

Measurement of areal coverage from samples heated to 500 °C was complicated by the fact that AgNP lines formed during deposition shifted in color and were thus more difficult to threshold using common algorithms. Nonetheless, the data in Figure 59 indicate a significant increase in AgNP coating durability over non heated samples. The reasons for increased durability will be discussed below.

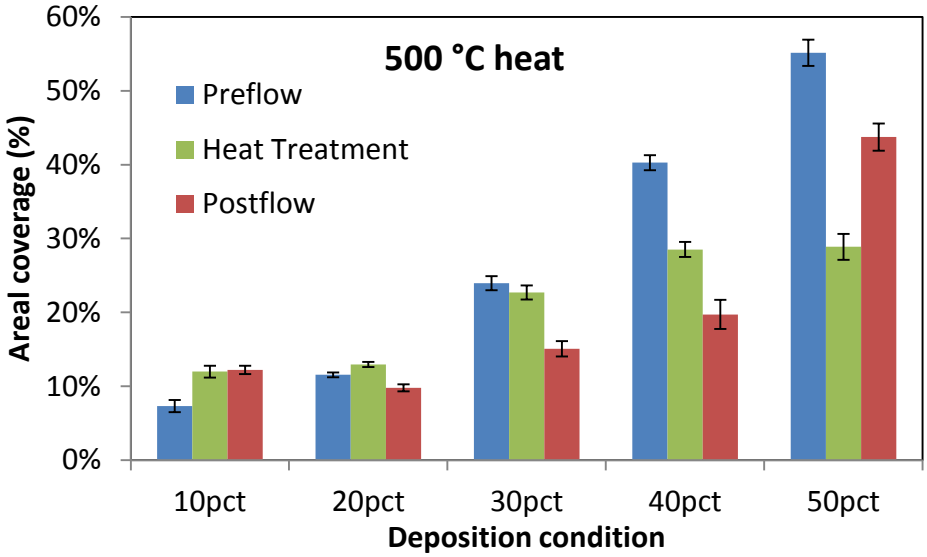

Figure 59: Areal coverage before and after flow cell with 500 °C heat treatment for various deposition conditions

7.5.2 Durability measured by coating thickness from AFM

In the previous section, optical microscope images were used to show a decline in areal coverage AgNPs as a result of liquid flow. As discussed above, the deposition lines created during VCD area likely composed of multiple layers of AgNPs. When submerged in water the upper particle layers are most likely to desorb. However, a monolayer or thin multilayer of AgNPs may remain. Thus, durability of AgNP coatings may be affected, even when there is no apparent loss of areal coverage.

Images and depth profile data were acquired for select samples of AgNP coated Si wafers that were subject to flow in a flow cell. Data was collected for samples of ~10%, ~30% and ~50% areal coverage that had undergone 200 °C and 500 °C heat treatments as well as control samples that were not heated. All data were compared to samples that were coated with AgNP but not subjected to flow. Durability of AgNP coatings was evaluated qualitatively by comparing the thickness of deposited lines in AFM images. In addition, thickness profile data was generated from the images using functions of Gwyddion software. That profile data was compiled and analyzed in Excel. A Matlab script was used to determine the width of deposited lines by pinpointing the leading and trailing edges of deposited lines.

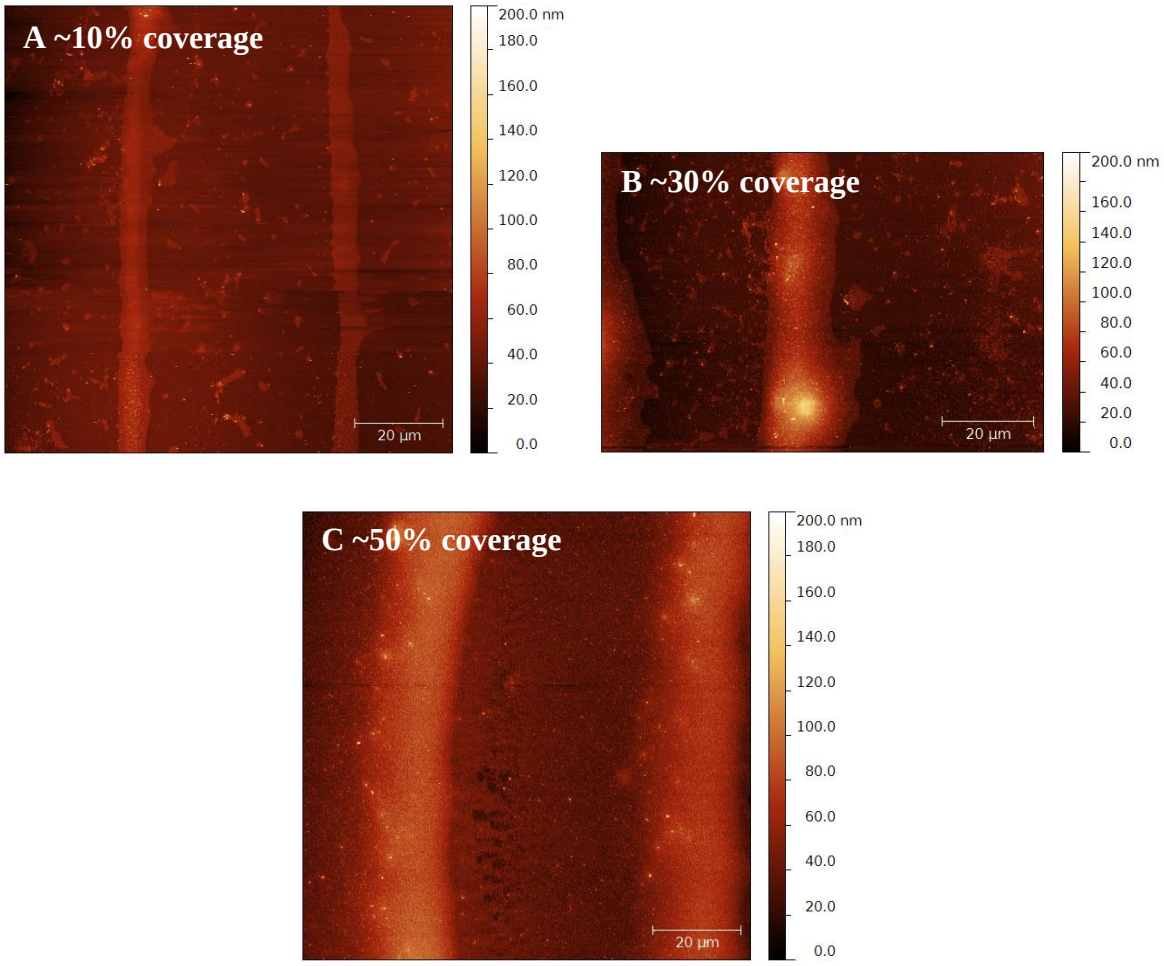

Figure 60: Pre-flow AFM thickness profile images for AgNP coatings made from three deposition conditions before flow cell: 10% (A), 30% (B), 50% (C)

In Figure 60 depth-based color maps from three deposition conditions show the thickness of the lines of deposited AgNPs created during VCD. Brighter color correlates to thicker AgNP coating. The images were taken from samples that had not been subjected to liquid flow and were not heat treated. The lowest density coating (A) has two thin deposition lines of AgNP. In the space between the lines particles appear to be more finely dispersed but not individually separated. Multiple layers can be seen in the deposition lines. Medium (B) and high (C) density AgNP coatings are thicker as indicated by brighter maxima in deposition lines. Groups of AgNPs are also more densely packed in the space between the lines, especially for the high density

deposition (C). In addition to an increase in line width as was seen before, the images show an increase in coating thickness as areal coverage increases.

However, when subject to flow of water in a flow cell, the thickness of deposited AgNP coatings declined significantly as seen in Figure 61. The image on the left shows a deposition line with maximum thickness of at least 150 µm. The post-flow image (right) has maximum thickness of approximately half (75 µm). Both images are from medium density AgNP coatings with approximately 30% areal coverage of silver. There is no apparent loss of areal coverage in the post-flow image, despite the significant decline in thickness.

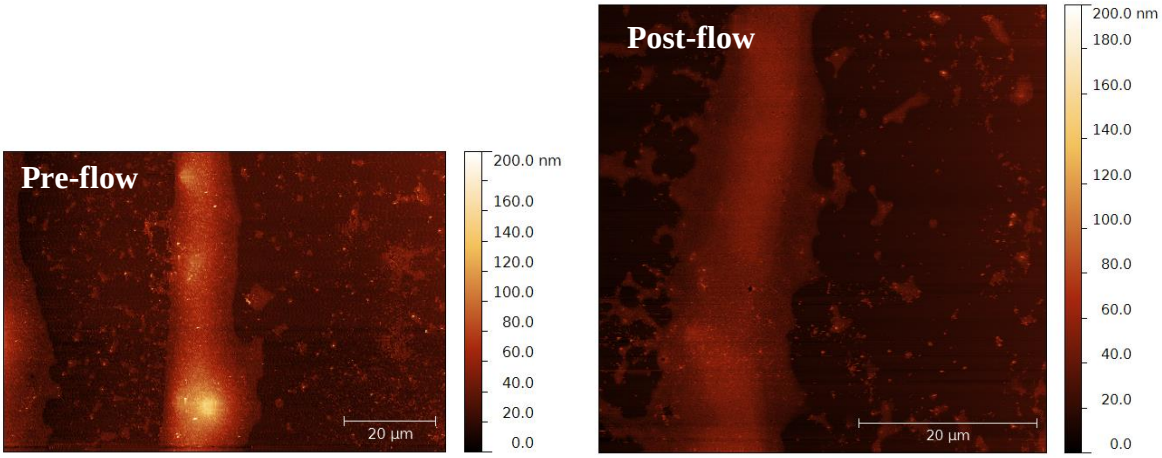

Figure 61: AFM images pre-flow (left) and post-flow (right) illustrate the loss of AgNPs from surface coatings. The thickness of deposited AgNP line is lower after flow. ~30% coverage.

As described above, heat treatment was used to improve durability of AgNP coatings. Figure 62 and Figure 63 compare post-flow images of untreated (left) and heat treated (right) samples with medium density AgNP coatings for 200 °C and 500 °C. There is a clear difference in the thickness of heat-treated AgNP coatings. Both heat treated samples have granular spots of high intensity that are larger than the size of individual particles (12.9 nm) and micellular agglomerates (64 nm). This perhaps indicates that high temperature annealing led to particle aggregation.

Also, at both temperatures it is likely that casein, the micellular protein that aids nanoparticle dispersion, has partially or completely decomposed. Studies in the literature indicate that casein in milk does not decompose when autoclaved to 121 °C [150]. Thermal analysis of casein decomposition has shown that the protein is fully pyrolyzed at 550 °C and produces ash, pitch, hard residue and gases [151]. Casein is decomposed at temperatures as low as 200 °C and the proportion of decomposition products is temperature dependent. At low temperature decomposition produces primarily hard residue (>80%) and above 500 °C the most common products are pitch (~40%), and hard residue (~35%) [152]. These products will remain on the surface and may contribute to increased attachment durability of AgNPs. The question of whether heat treatment and these decomposition products lowers antibacterial efficacy will be addressed below.

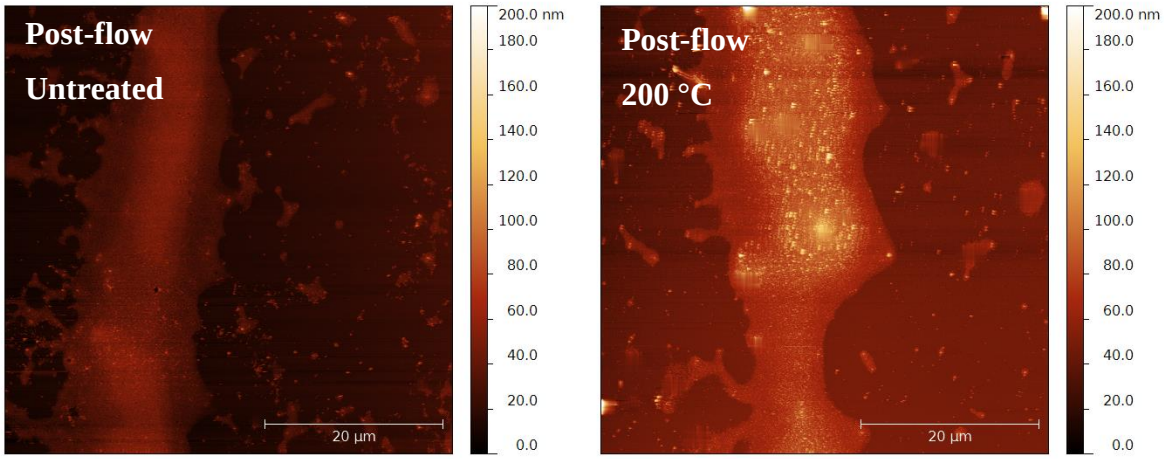

Figure 62: Comparison of AgNP coatings after flow cell when processed without heat treatment (left) and with 200 °C heat treatment (right). The heat treated sample maintained a thicker coating. ~30% coverage.

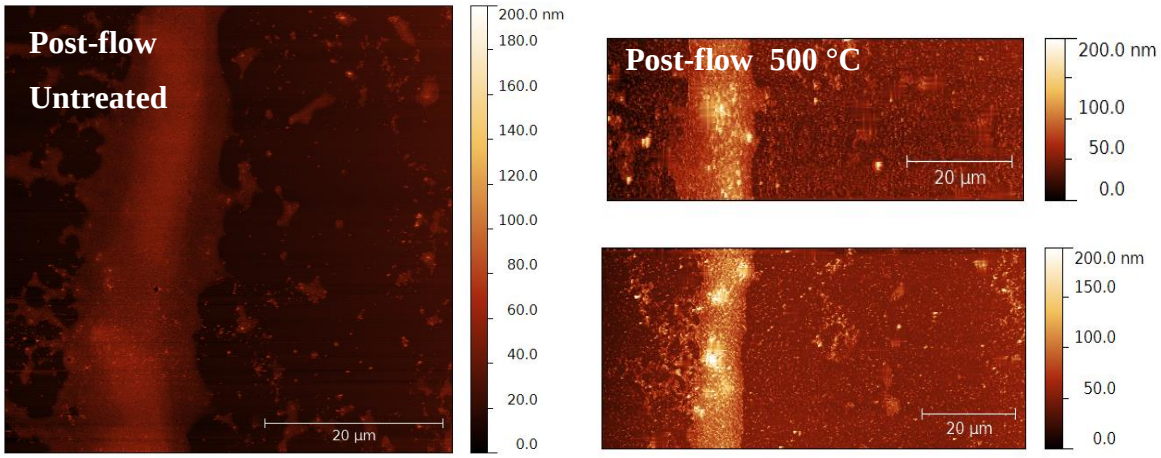

Figure 63: Comparison of AgNP coatings after flow cell when processed without heat treatment (left) and with 200 °C heat treatment (right). The heat treated sample maintained a thicker coating. ~30% coverage.

Profile data from AFM images were collected by averaging the thickness in each pixel column across the horizontal axis. An example of this profile data is shown in Figure 64. Thickness data is plotted on the y-axis and horizontal position on the x-axis. The plot has been aligned so that the data match the horizontal position in the AFM image above it. The local maxima that correspond to deposition lines were recorded. This was done at least 5 times for each sample and the thickness was averaged.

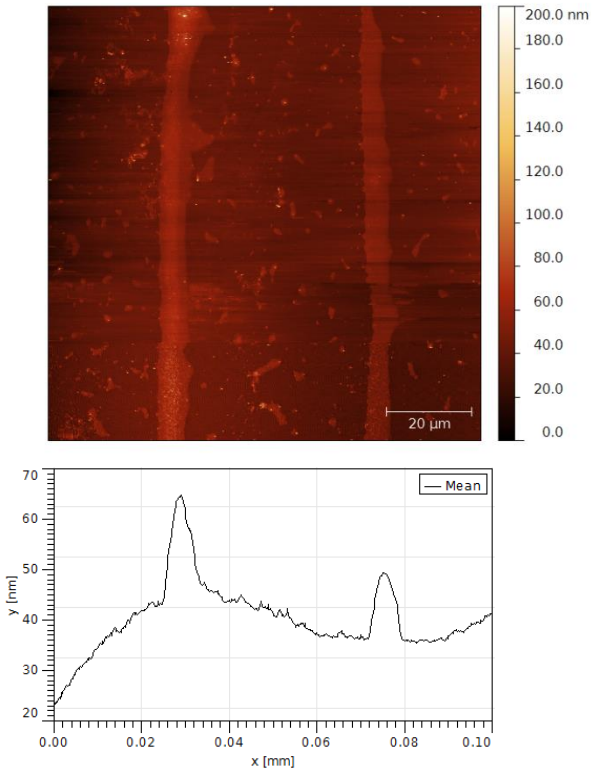

Figure 64: Example profile data (bottom) from AFM image (top) of AgNP coating. Data like this was used to calculate peak thickness and line width.

Data in Figure 65 show average thickness of AgNP coatings for three deposition conditions with no heat treatment before and after flow. At all three conditions there is a significant decline in line thickness. Thickness in the low density deposition declined from 57.3 to 39.8 nm. Likewise, the medium density AgNP deposition decline from 90.2 to 47.4 nm and the high density deposition declined from 87.3 to 57.2 nm. Recall that particle size measured by DLS was 64±6nm and that this is likely the diameter of smaller particles agglomerated on casein micelles. This would suggest that the low density deposition condition results in monolayers of AgNP groups. Both the medium and high density depositions have multilayers that are 1.4 times thicker than monolayers on average. It is unlikely that VCD results in deposition of more than 3-4 layers in any given area. In all cases, thickness was reduced by 30-50%, a significant decline in after just 72 hours of liquid flow. It is important to remember that line thickness could only be

measured where lines remained on the surface. High density AgNP coatings were reduced from 45.2% to 8.0% areal coverage. The data for line thickness only represents the 8.0% that remained on the surface and also became thinner. Taking both areal coverage and line thickness into account approximately 88.4% of silver deposited in the high density sample was removed from the surface.

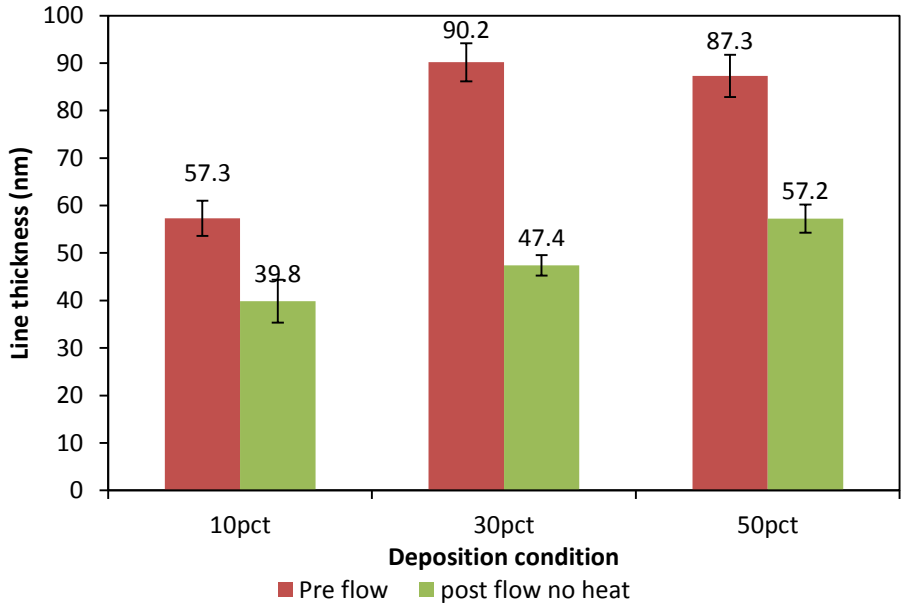

Figure 65: Line thickness of AgNP coatings before and after flow in a flow cell. SEM error bars, N=5.

Line thickness was also measured after flow for heat treated samples and the data are shown in Figure 66. As was clear from AFM, heat treatment prevents loss of nanoparticles from the surface of deposited lines. Heating to 200 °C resulted in no significant decline in line thickness for the low and high density coatings. There was a decline, from 90.2 to 68.9 nm, that was less severe than when left untreated. Heating to 500 °C eliminated loss of AgNPs during flow. In the high density deposition, the high temperature treatment resulted in a significant increase in average line thickness. This could result from agglomeration of particles or formation of pyrolysis products during decomposition of casein.

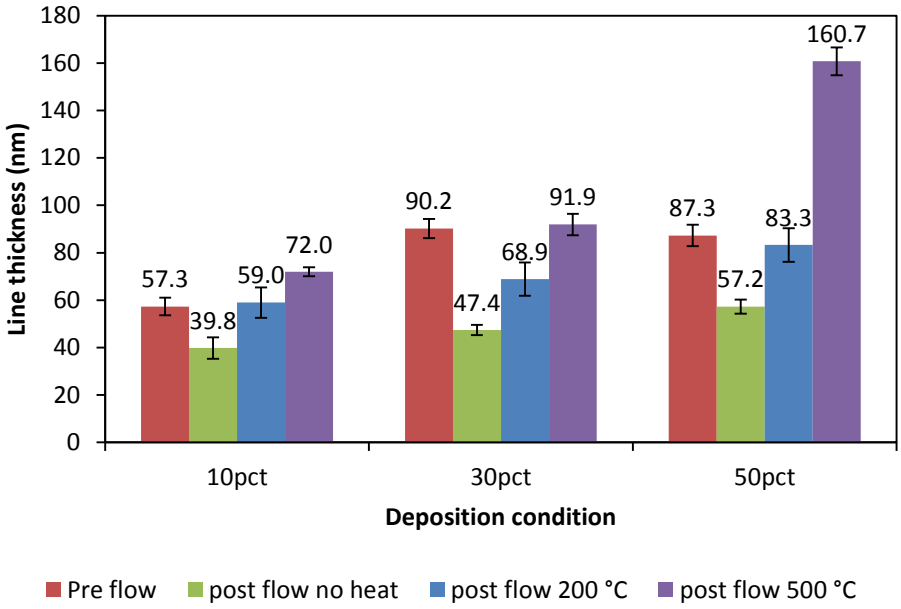

Figure 66: Line thickness of AgNP coatings before and after flow for heat treated samples as compared to untreated samples. Thickness is maintained or enhanced as a result of heat treatment. SEM error bars, N=5.

Line width was also measured from AFM profile data. In Figure 67 line widths are shown pre-flow and post-flow for three heat conditions and three deposition conditions. As was seen before, line width increases from low to high density deposition. In fact, line widths measured by AFM were compared to those measured by SEM in Figure 68. The data were well matched, an indication that measuring line width in AFM is at least as accurate as the SEM method used above.

Post-flow samples that were not heat treated showed a decline in line width, especially for high density AgNP coating. Heat treatment essentially eliminates this reduction. Taking the high density deposition condition as an example line width is 28.5 µm pre-flow, it declines to 23.7 µm after flow, but when heat treated to 200 °C or 500 °C line width is 33.5 µm and 28.5 µm, respectively.

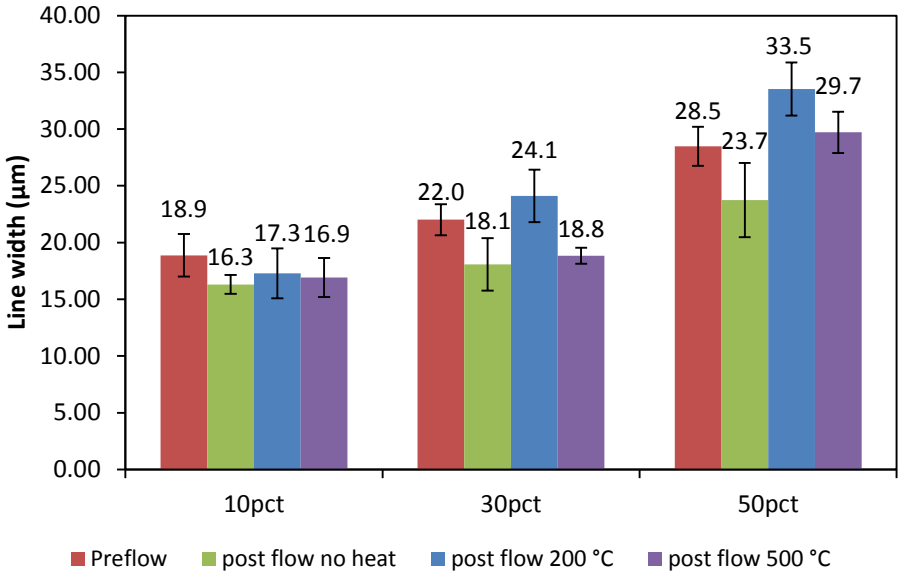

Figure 67: Line width of AgNP coatings before and after flow for heat treated samples as compared to untreated samples. Line width decreases for samples with no heat treatment. It is unaffected on heat treated samples. SEM error bars, N=5.

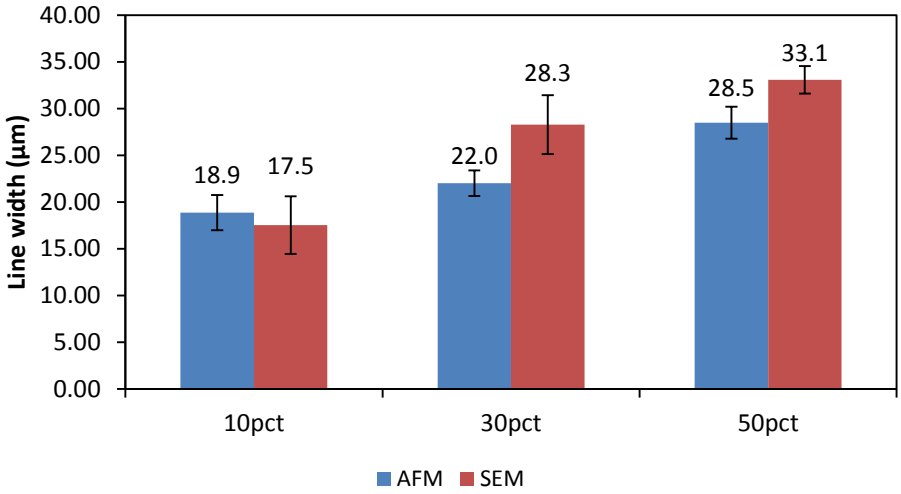

Figure 68: Comparison of line width measured in AFM and SEM.

7.5.3 Implications of durability experiments

As discussed above durability of AgNP coatings is important both to extend antibacterial properties and to limit proliferation of AgNPs into the environment. The results presented above demonstrate that AgNP coatings are highly susceptible to losses during flow. One deposition

condition resulted in loss of 88.2% of silver after 72 hours. Although this is an extreme case, it highlights the need to improve durability through processing. To that end, one post deposition processing technique was investigated. Heat treatment at 200 °C and 500 °C dramatically improved AgNP coating durability. The lower temperature was at least as effective as the higher temperature, while avoiding possible silver oxidation. To improve durability surfaces and filters coated with antibacterial AgNPs should be heated to at least 200 °C.

7.5.4 Effect on theoretical calculation of areal coverage

As a result of line thickness data, the factors that contribute to areal coverage can be re-evaluated. Recall that in section 7.4.5 the functional dependencies of line width W_l and line density D_l were determined by expressing areal coverage N as the product of the two. See equation (10). However, one assumption made in order to perform theoretical calculations of areal was that AgNPs were deposited in close-packed monolayers. Figure 65 proves this was not the case experimentally. Only the lowest density depositions had line thickness comparable to the diameter of AgNPs micelle groups (~60nm). Multilayer deposition within lines should be included in theoretical calculations. Empirically, the data show that areal density would be approximately 35% lower than previously predicted. Areal density is

$$N = W_l \cdot D_l \cdot \frac{1}{M_l} \tag{11}$$

where M_l is a multilayer factor that determined empirically as line thickness divided by monolayer thickness. For experimental conditions described here this factor is approximately 1.5. Using this modified equation theoretical areal coverage was adjusted and is shown in Figure 69 for a range of deposition conditions. The adjustments have brought theoretical predictions

more in line with experimental results, especially for depositions with 4.4 and 8.8 g/l AgNP concentrations.

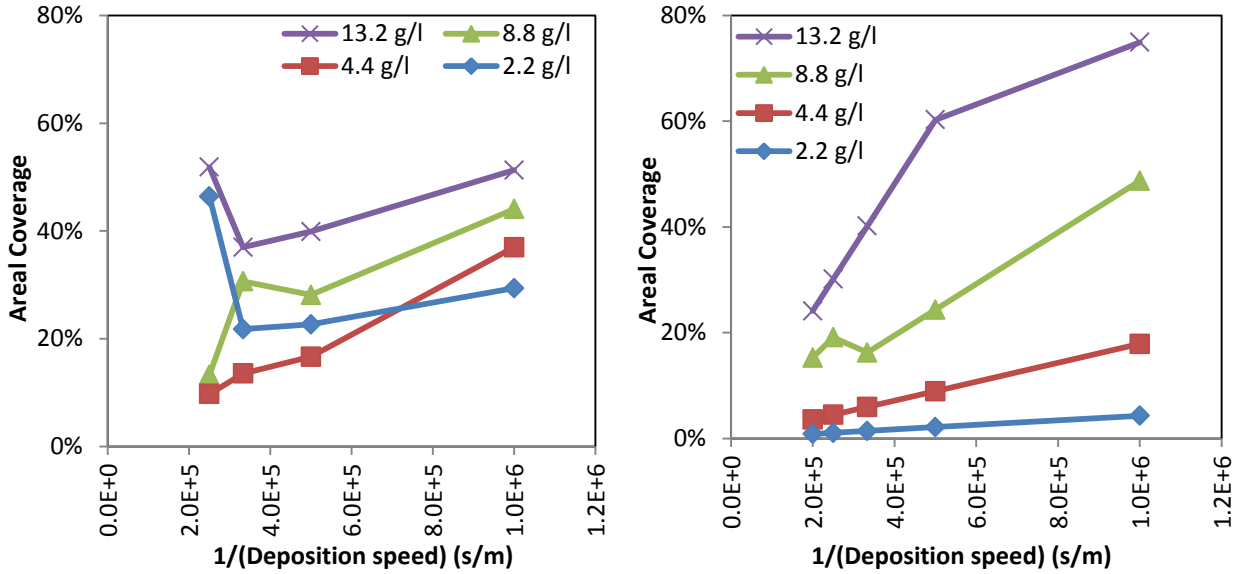

Figure 69: Comparison of experimental (left) and theoretically calculated (right) areal coverage

7.6 INHIBITION OF BIOFILM FORMATION IN A FLOW CELL

The antibacterial efficacy of silver nanoparticles was demonstrated against three species of environmental mycobacteria. The susceptibility of the different species was varied. *M. marinum*, an aquatic species, may have developed a higher resistance to silver as a result of exposure to toxic metals ions in the environment. Proliferation of silver nanoparticles in the environment may cause other species to develop resistance. Indeed, *M. smegmatis* cultured in a silver enriched environment developed a stronger resistance to silver than an unmodified strain.

Deposition by drying is a simple method that allows the same nanoparticles used in planktonic susceptibility studies to be used on biofilms. In this research vertical colloidal deposition (VCD), a technique that deposits particles on a surface as they become trapped by the

movement of a receding meniscus, was used to deposit silver nanoparticles on etched silicon substrates. The areal density and morphology of the deposited silver was controlled by varying nanofluid concentration and deposition speed.

The final objective of this research is to culture biofilm *in vitro* on AgNP coated samples and measure the effects of varying areal coverage on biofilm growth. Biofilm was cultured on membrane filters and in a parallel channel flow cell, protocols designed specifically for these experiments.

7.6.1 Incorporation of silver on membrane filters

Figure 70 shows the incorporation of AgNP on a membrane filter. In backscatter electron (BSE) mode the pores in the AgNP coated region (left) of the membrane filter in the SEM micrograph in Figure 70a are filled with AgNP. Because of the higher atomic number of silver (47) compared to the predominantly carbon-based (6) membrane the AgNP coated region is spotted with white rings. In the uncoated region (right) the pores are comparatively dark. Figure 70b and Figure 70c are high magnification micrographs of the AgNP coated and uncoated regions, respectively. In secondary electron (SE) mode nanoparticles and aggregates of nanoparticles are visible both in the pores and across the membrane surface. Nanoparticles are not visible in the uncoated region shown in Figure 70c.

EDS was performed at various locations on the membrane surfaces. A representative spectrum from the AgNP coated region (Figure 70d) show two clear peaks at 2.99 keV and 3.15 keV, which correspond with the characteristic x-ray energies for Ag-$L_{\alpha 1,2}$ and Ag-$L_{\beta 1}$, respectively. In Figure 70e there was no silver detected in the EDS spectrum. The incorporation of silver in the membrane was confirmed analytically by BSE imaging and EDS and visually in

secondary electron SEM. Additional SEM micrographs illustrating the incorporation of AgNPs on the membrane surface are shown in Figure 71.

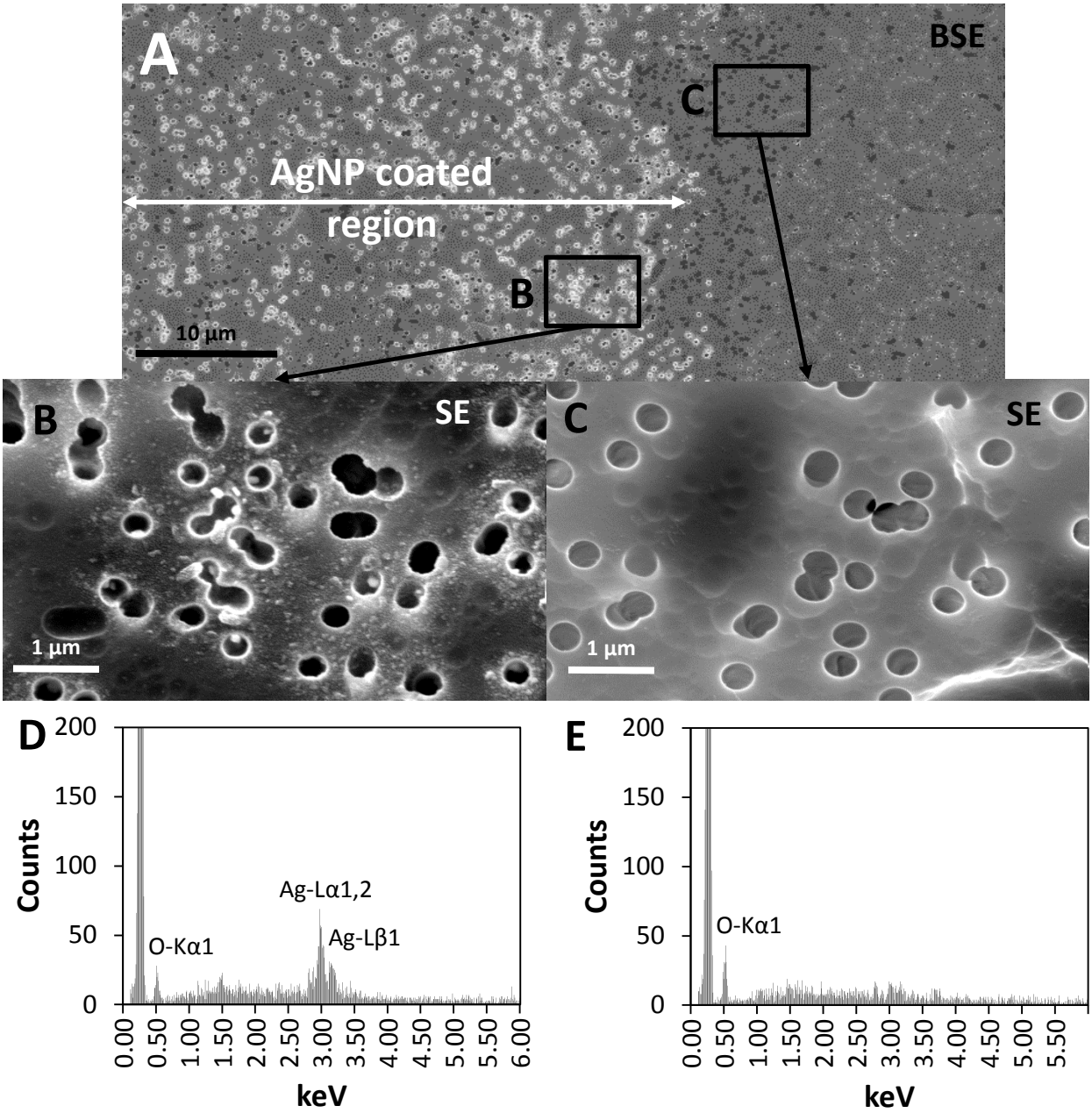

Figure 70: (A) SEM of Polycarbonate track etched membrane in BSE mode showing AgNP coated region (left) with bright pores where silver is deposited (B) SEM of PC membrane in SE mode with deposited AgNP (2.2 g/l) in pores and on membrane surface. (C) SEM of PC membrane in SE mode in uncoated region. Location of (B) and (C) are outlined in black in (A). (D) EDS spectrum from AgNP coated region. Peaks at 2.99 keV and 3.15 keV for Ag-Lα1,2 and Ag-Lβ1, respectively. (E) EDS spectrum from uncoated region (C) does not indicate presence of silver.

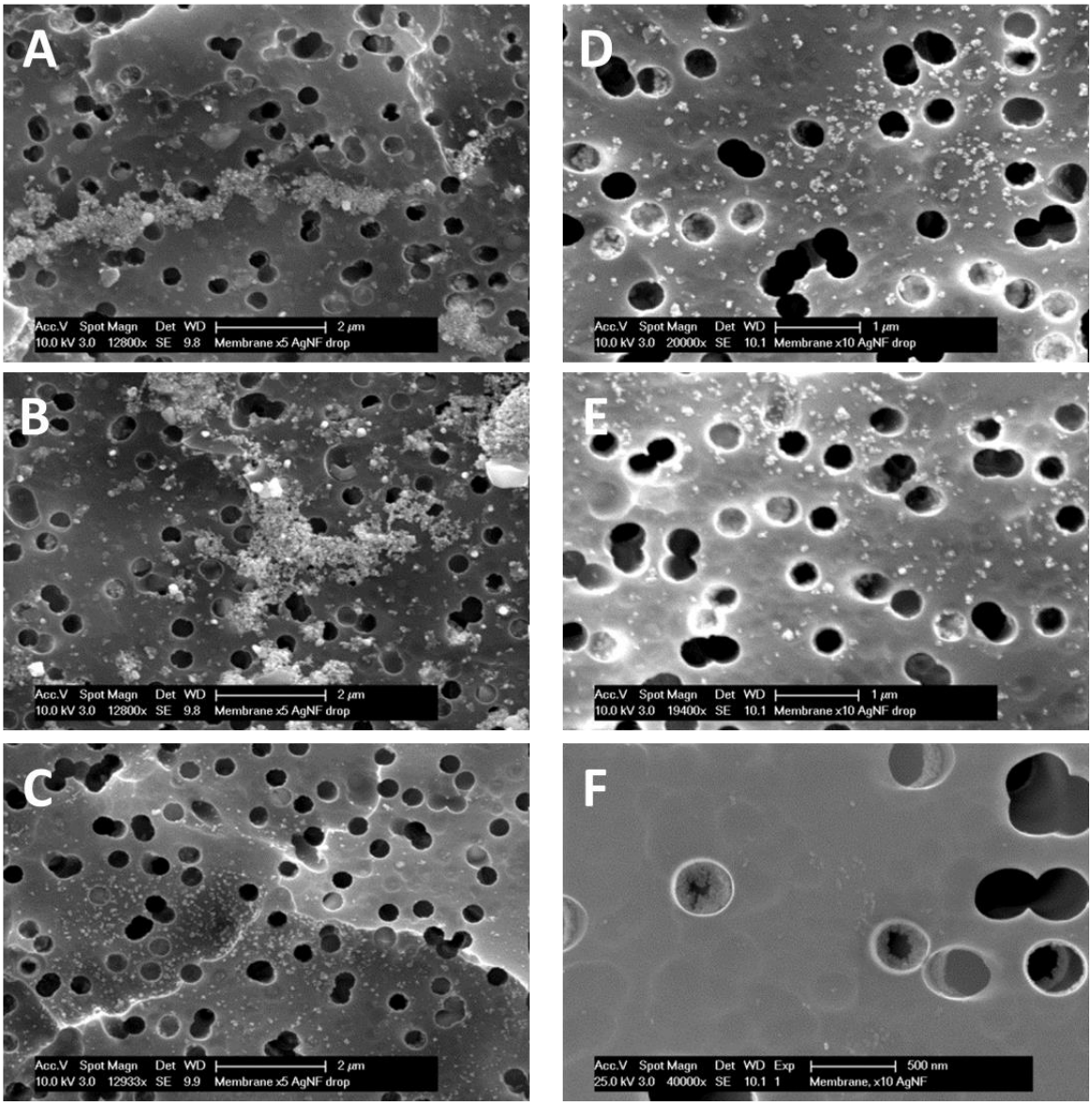

Figure 71: SEM micrographs of AgNP coated membrane filters. A, B, and C were coated with 1.1 g/l AgNP nanofluid. D, E, and F were coated with 2.2 g/l nanofluid. The images show the three main ways that AgNPs were deposited – as aggregates in A and B – across the membrane surface in C, D and E – and in pores as shown in F.

7.6.2 Efficacy of AgNP coated membrane filters

When cultured on porous membranes coated with AgNPs growth of *M. smegmatis* was inhibited when compared to growth on an uncoated control membrane. Figure 72 shows images at three scales of bacterial growth on control membrane filters (Figure 72a,b,c) and on

membranes coated with 2.2 g/l AgNP (Figure 72d,e,f). Bacterial colonies are clearly visible in the image in Figure 72a and in the SEM micrograph in Figure 72b. The diameter of colonies is hundreds of microns. Some colonies have grown so large that they have merged with other nearby growths. Figure 72c shows bacterial growth near the edge of one colony. The biofilm is dense and covers the pores of the membrane thereby fouling the filter. Corresponding images for the AgNP coated membrane show no visible colonies. Discoloration from the AgNP deposition is visible in Figure 72d. In Figure 72e it is difficult to discern the low number of small bacterial colonies. One such colony with diameter 30μm is shown in Figure 72f.

Bacteria were removed from the membranes by sonication and CFUs were counted. Figure 73(left) shows CFUs of *M. smegmatis* from membranes coated with two AgNP concentrations and a control. On the control membranes bacteria multiplied by 1000% ± 200%. On the other hand, only 0.03% ± 0.01% of the seeded bacteria survived on membranes coated with 1.1 g/l nanofluid. Doubling the concentration of silver reduced surviving bacteria by another factor of 10, a 0.003% ± 0.001% survival. Standard error from triplicate experiments is shown on the plot.

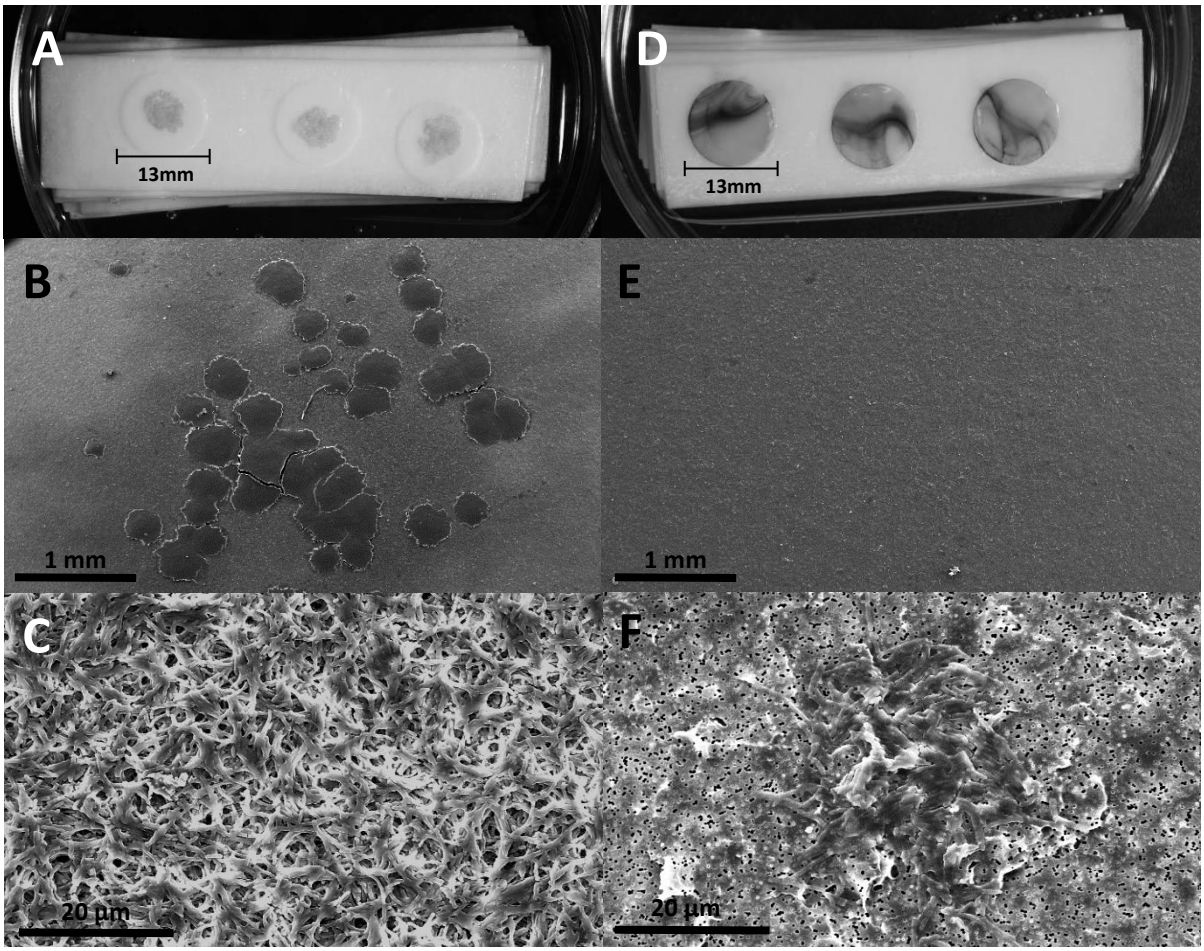

Figure 72: Growth of *M. smegmatis* on control membranes is shown at three scales in a photo (A) and two SEM micrographs (B) and (C). Strong bacterial growth is seen in each image. D, E, and F membranes coated with AgNP (2.2 g/l). Dark streaks on the membranes in (D) come from silver. An isolated colony of ~30 µm diameter is shown in (F).

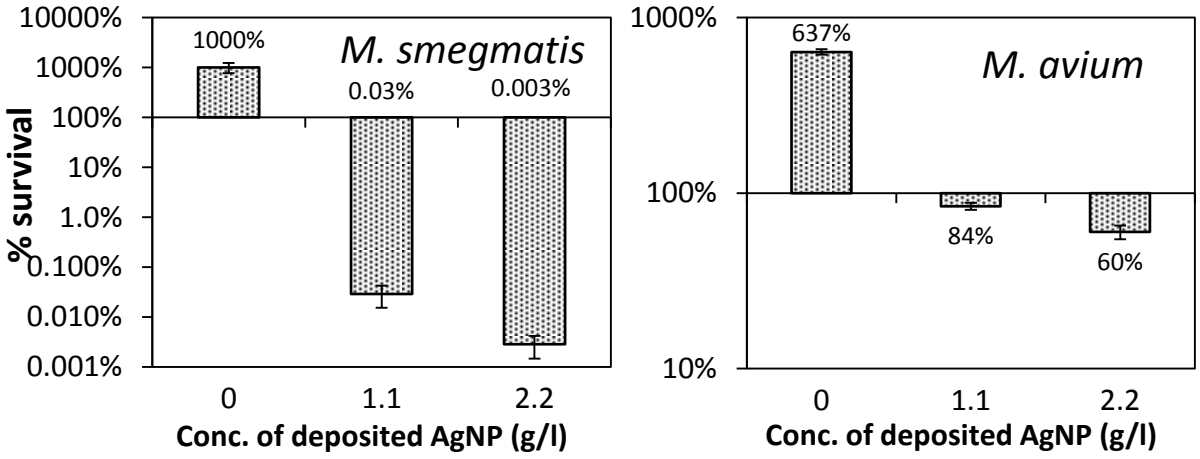

Figure 73: (left) Percent survival of *M. smegmatis* on porous membrane with varying concentrations of deposited AgNP. (right) Percent survival of *M. avium* under the same conditions. Error bars show standard error. N=3.

Similarly, *M. avium* growth was inhibited on silver coated membranes. Figure 73(right) shows a plot of percent survival of seeded bacteria for the two AgNP deposition conditions and a control. Like with *M. smegmatis*, the negative control membranes had large colonies of biofilm. The lower concentration silver coated membranes (1.1 g/l) had smaller colonies and there were no macroscopically visible colonies on the high concentration silver coated membranes (2.2 g/l). When CFUs were counted from the membranes *M. avium* growth was clearly inhibited. Bacteria on the control grew by 637% ± 22% over the seeded amount. There was a 15.8% ± 3.9% reduction from 1.1 g/l coating and 40.0% ± 5.3% reduction from 2.2 g/l. As in the planktonic exposure, *M. avium* was less susceptible to surface deposited AgNPs than *M. smegmatis*. Standard error was calculated from triplicate measurements and error bars are shown in the figures.

The time series growth of *M. smegmatis* is shown in Figure 74. Bacterial colonies on the control membranes are visible at 41 hours and grow as expected through 72 hours. Nearby colonies merge and then continue to grow horizontally across the membrane surface in a biofilm. AgNP coated membranes did not have visible colonies at the given magnification until 63 hours. There is a stark difference in the extent of biofilm growth at 72 hours in terms of the areal coverage. This difference is a result of both slower bacterial growth and fewer colonies on the AgNP coated membranes.

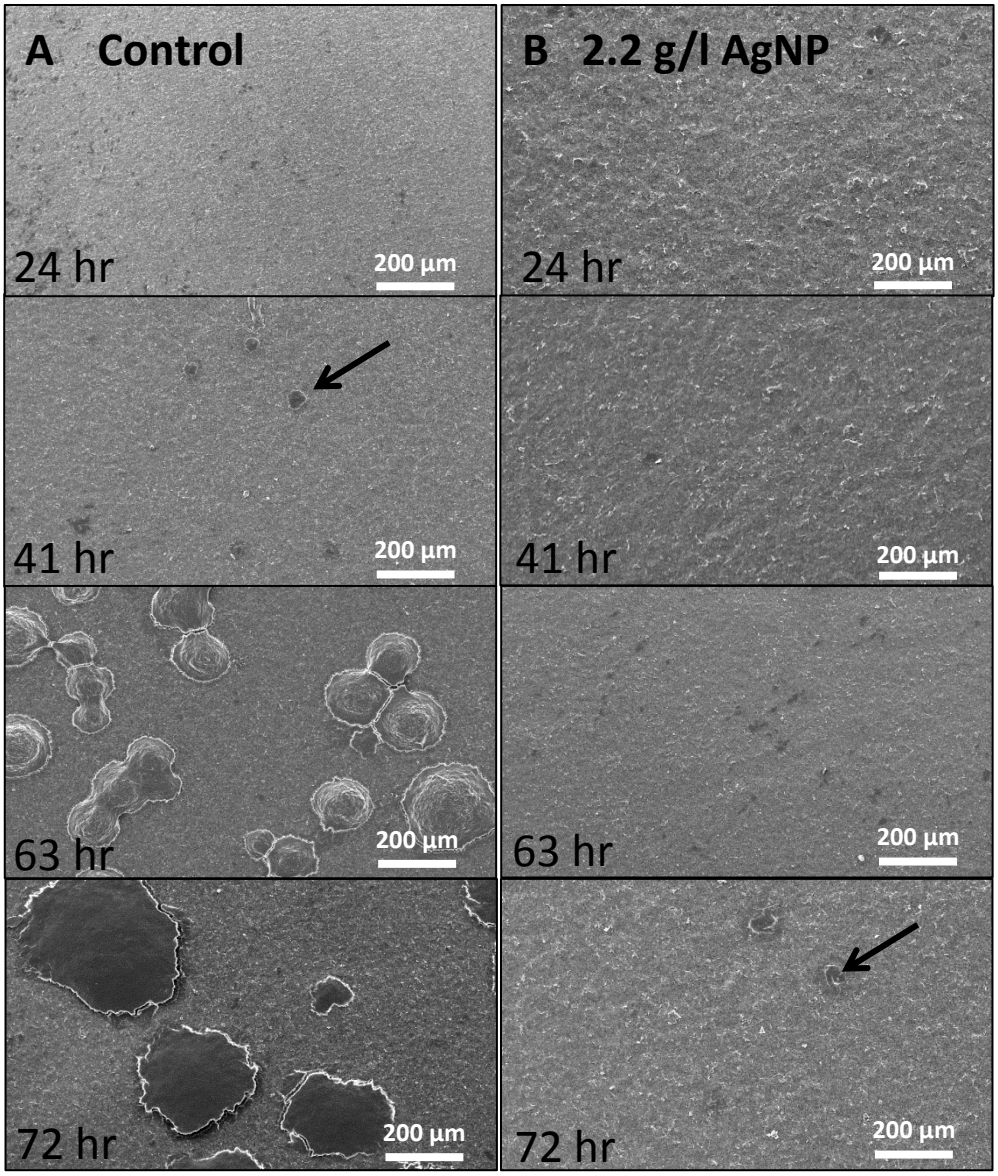

Figure 74: Time series SEM of *M. smegmatis* growth on (A) control and (B) AgNP coated (2.2 g/l) membrane filters from 24 -72 hours. Growth is inhibited on the AgNP coated membrane. Colonies of diameter ~50 µm are annotated at 41 hours for the control and 72 hours for the AgNP coated membrane.

Similarly, *M. smegmatis* bacteria were cultured on membranes with a range of concentrations of AgNPs deposited by drying AgNP fluid from drops. Concentration of AgNP ranged from 2200 to 0.5 mg/l. SEM images from membrane are shown in Figure 75, which is spread over two pages. Next to each SEM image is a black and white mask showing only the size and shape of bacterial colonies. This mask was created in ImageJ. The software was then used to calculate colony size and morphology.

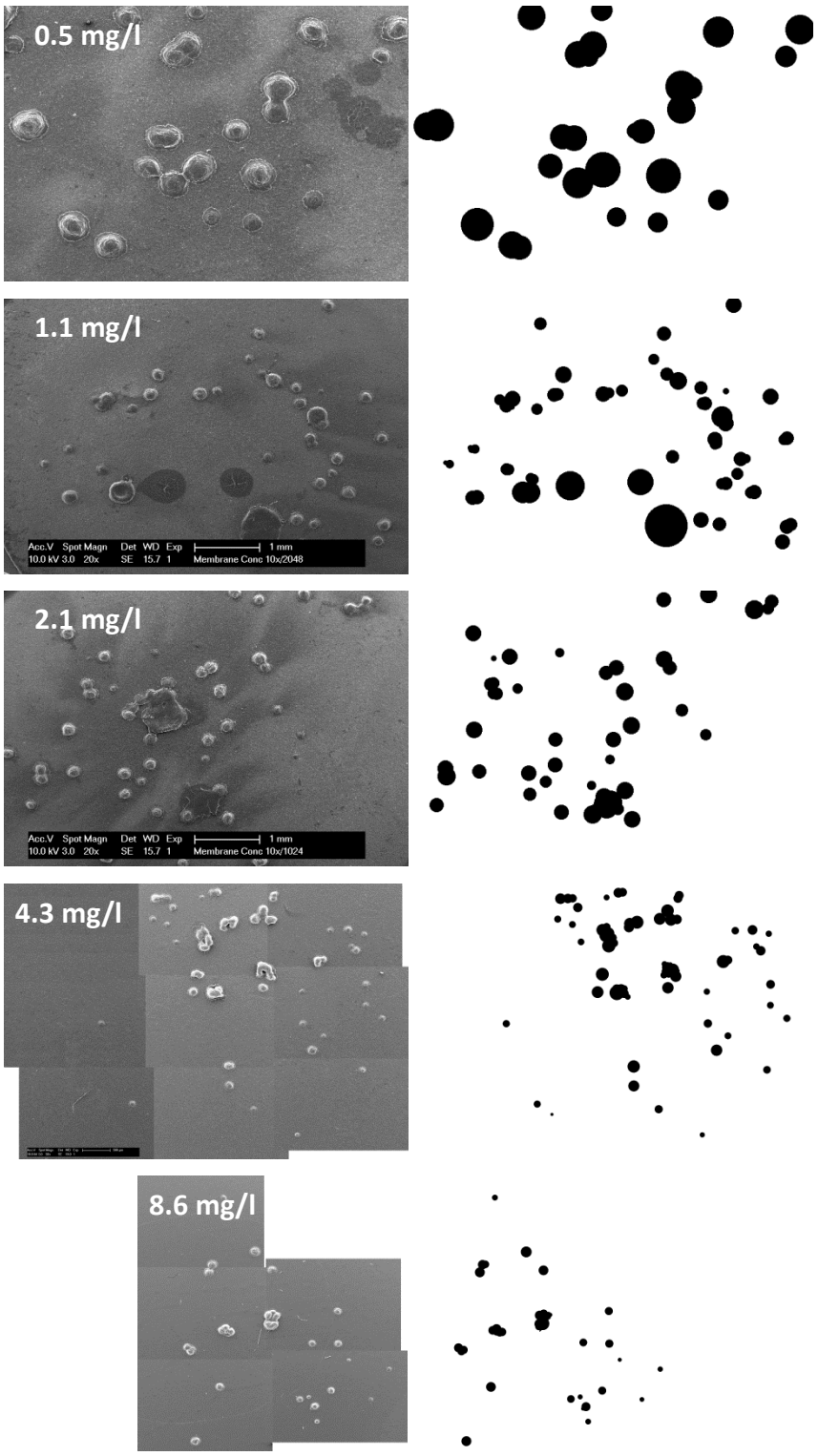

Figure 75: Bacterial colonies on membrane filters with various concentrations of AgNP (page 1)

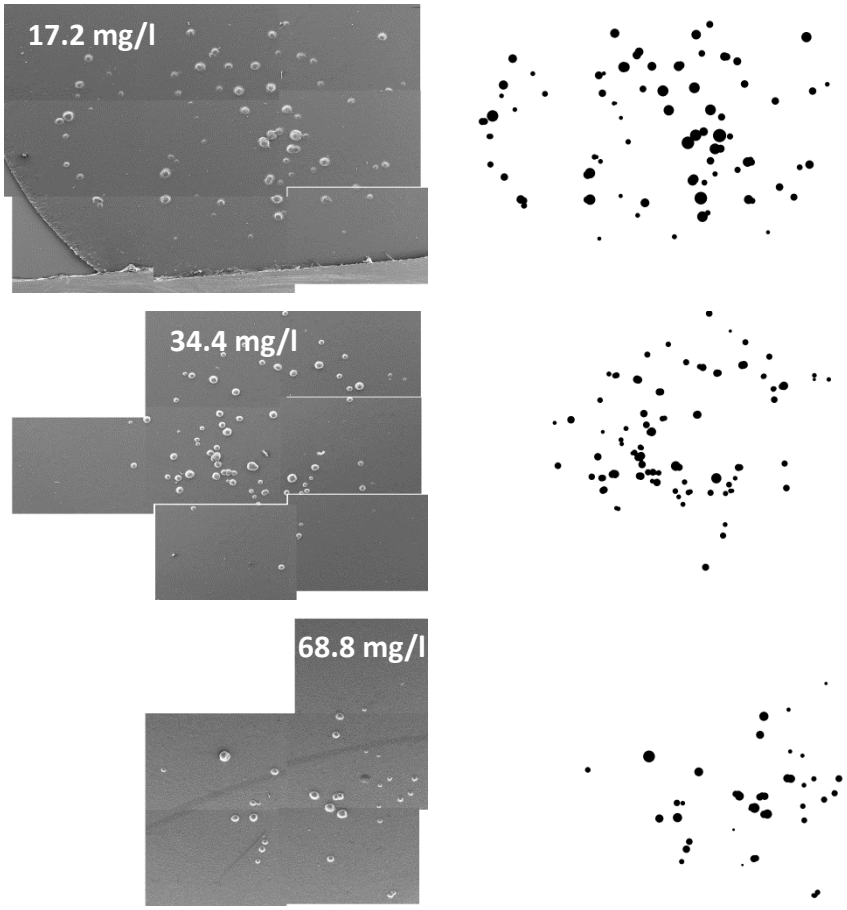

Figure 75: Bacterial colonies on membrane filters with various concentrations of AgNP (page 2)

Images in Figure 75 are ordered from lowest to highest concentration. At the lowest concentration there is no apparent effect on the growth of bacterial colonies. However, when concentration of AgNP is 2.1 mg/l or higher bacterial colonies appear smaller. Above 68.8 mg/l no visible colonies formed after 72 hours incubation. From the black and white images of each sample the areal coverage of bacteria was calculated. Also, the number of colonies was counted and average colony size was calculated. Finally, several morphological shape factors were measured using a standard ImageJ algorithm. The shape factors measured were roundness and perimeter.

Figure 76 and Figure 77 show the decline in areal coverage and average colony size with increasing concentration of deposited AgNP. The number of bacterial colonies was not

consistent and was likely more influenced by the quantity of bacteria in the inoculum. From Figure 77 there appears to be little or no effect of AgNPs on colony size below 4.3 mg/l. This value can be thought of as the minimum inhibitory surface concentration (MISC), a surface specific quantity analogous to MIC in planktonic culture. Then the minimum bactericidal surface concentration (MBSC) was 68.8 mg/l.

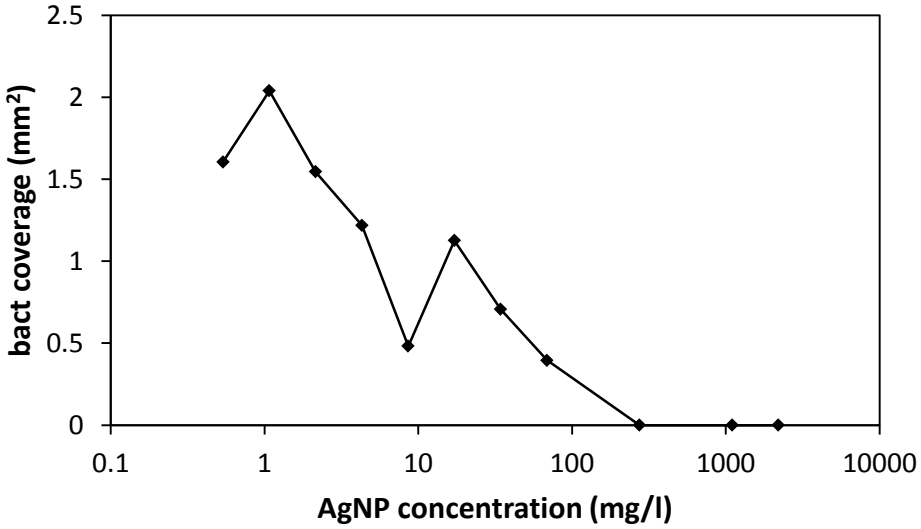

Figure 76: Areal coverage of bacteria on porous membrane filters with increasing concentration of AgNP

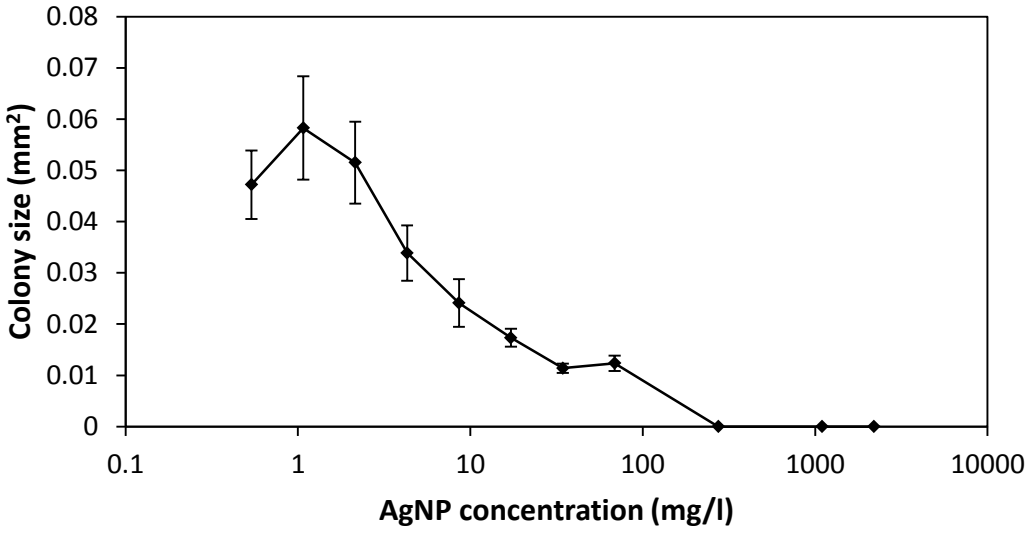

Figure 77: Average colony size on membrane filters with deposited AgNP

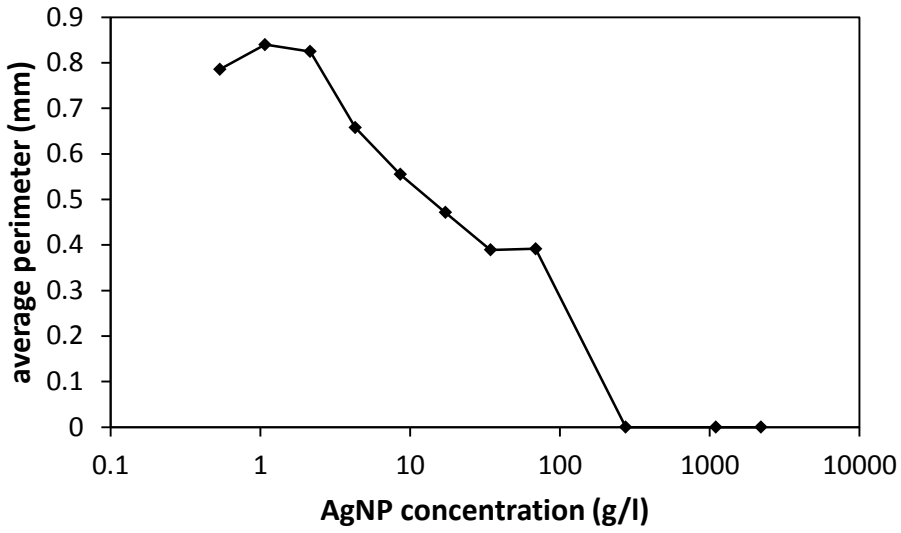

Figure 78: Average perimeter of bacterial colonies on membrane filters with deposited AgNP

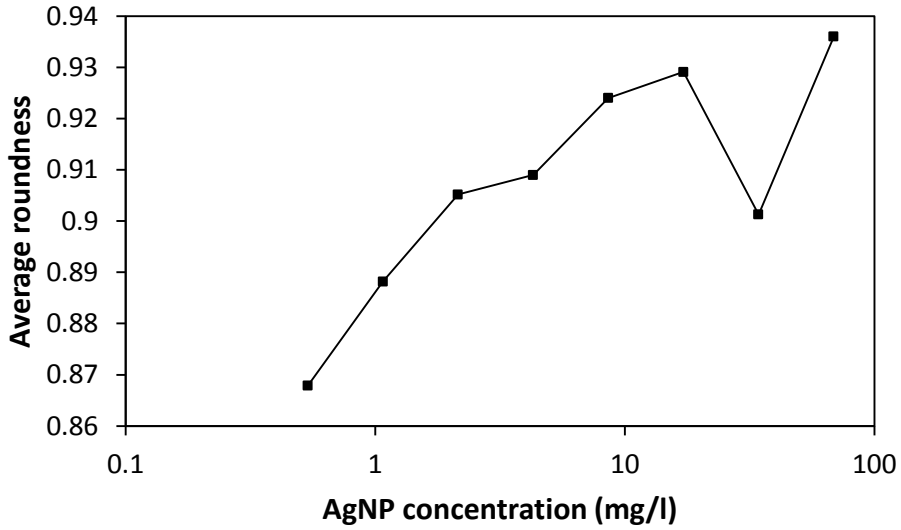

Figure 79: Average roundness of bacterial colonies on membrane filters with deposited AgNP

Figure 78 and Figure 79 show the effect of AgNP concentration on two shape factors of bacterial colonies, perimeter and average roundness. Generally, perimeter declined and roundness increased with increasing AgNP concentration. The decline in perimeter would be expected, due to the dropping colony size. The increase in roundness is because the small colonies present at high AgNP concentration are more likely to be individually separated rather

than coalesced with other nearby colonies. When colonies merged they form distinctly non-round shapes, as can be seen in the images in Figure 74 and Figure 75.

Surface deposited AgNPs could lead to declines in bacterial coverage and average bacterial colony size by reducing the number of colonies or the size of individual colonies. It is more likely the latter. Growth rate of bacterial colonies is the difference between the reproduction rate and the death rate of individual bacteria. The expansion of bacterial colonies on AgNP coated membranes is probably limited by an elevated death rate.

7.6.3 Bacterial culture under flow conditions

The efficacy of deposited AgNP coatings was also measured in a flow cell. The flow cell was used to emulate the natural conditions in which biofilm form. First, AgNPs were deposited on a silicon wafer and a control substrate was prepared without silver. The samples were preloaded into the experimental chambers of a flow cell. Then an inoculum of *M. smegmatis* (MC^2 155) was injected into both experimental chambers. Flow of sterile media was started (0.06 ml/min) and left for 72 hours at 37 °C. After this time the samples were removed and examined by optical microscopy and SEM. Biofilm was successfully cultured in the flow cell. However, some data were contaminated by leaks and other interruptions in flow. The data collected below are from three independently run experiments that did not suffer systematic errors or biasing due to these effects.

7.6.4 High magnification optical imaging

Wafer samples with biofilm were imaged on a digital optical microscope using a high magnification lens. In these images the substrate wafer is pale green, biofilm is dark grey or

black and silver, which is only seen in the high density coating is orange and brown. Figure 80 has images from four samples: A) control with no silver B) 6.0% areal coverage of AgNP C) 24.2% coverage and D) 45.2% coverage. There is a clear decline in the growth of biofilm as the areal coverage of deposited AgNP increases.

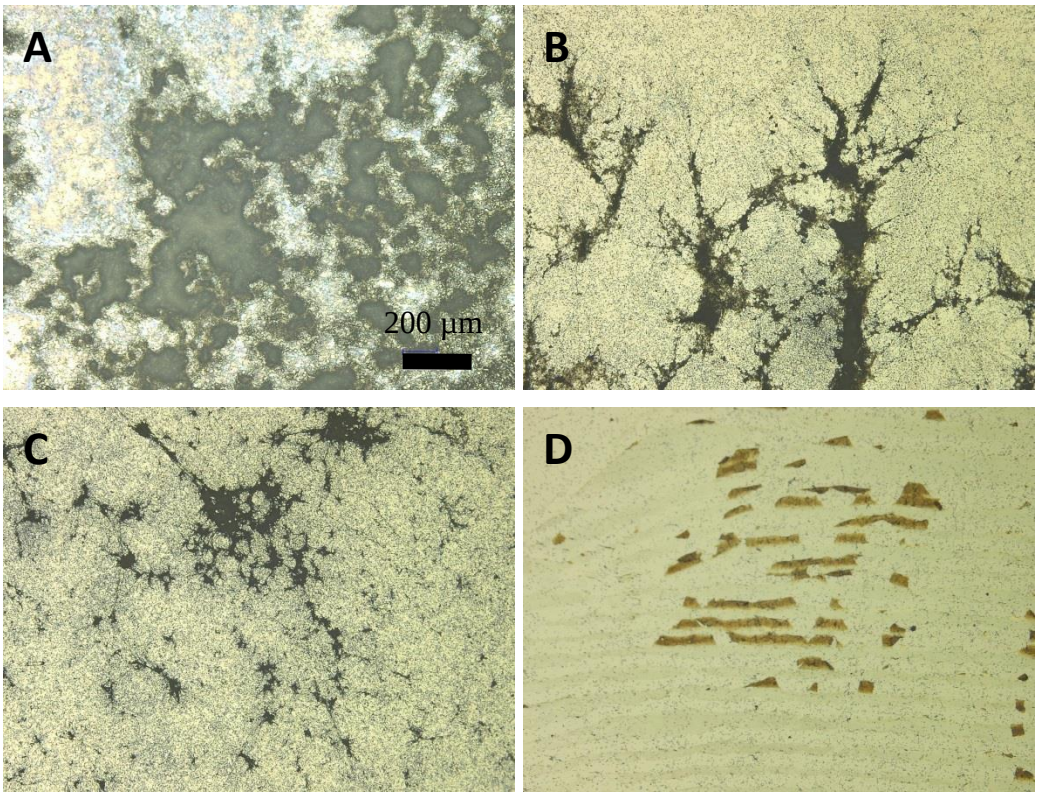

Figure 80: Optical microscopy images of biofilm (dark) growth on Si wafer samples with four areal coverage percentages A) 0% control B) 6.0% C) 24.2% D) 45.2%.

7.6.5 Morphology of biofilm in SEM

To further understand the formation of biofilm samples were imaged in SEM. As described above bacteria form complex hierarchical structures. In biofilm bacteria excrete an extracellular polymer substance (EPS) that can aid surface attachment and biofilm coherence. The bacteria in Figure 81 formed densely packed groups that formed an open structure that allows for the flow of nutrients throughout. This is the kind of structures that are characteristic of

robust and healthy biofilm. Colonies of bacteria from static culture, like those seen in the previous section are extremely dense and do not have an open structure as seen below. Additionally, static cultured tend to grow radially outward from the growth origin. Biofilm in flow conditions spreads more sporadically according to availability of nutrients and fluid dynamics.

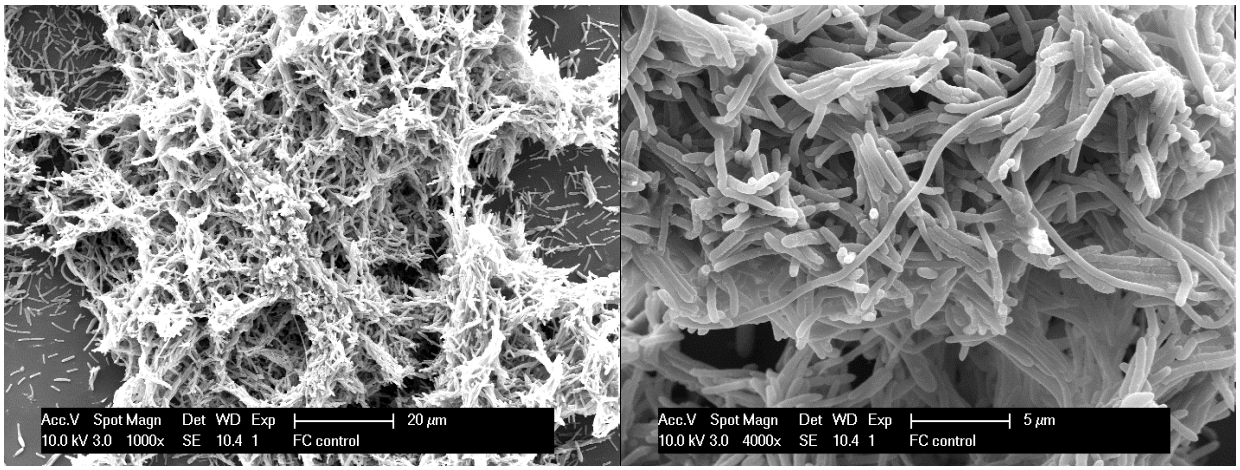

Figure 81: Biofilm growth on control sample

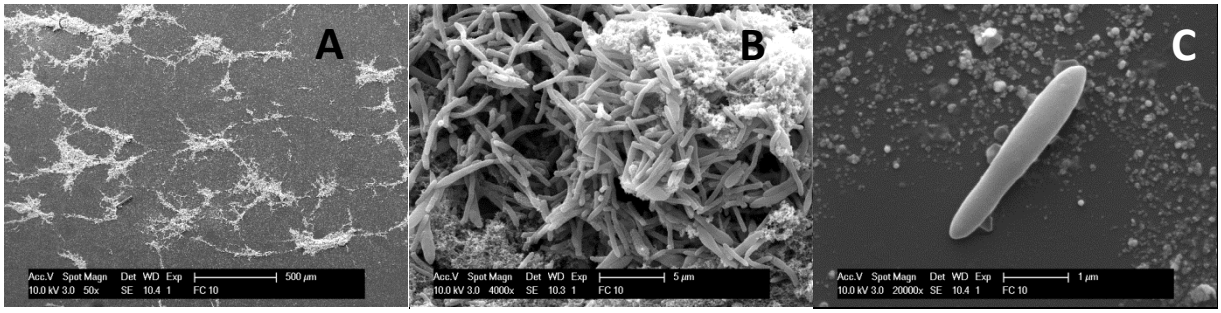

Figure 82: Biofilm growth on low AgNP coverage sample (6.0%). Biofilm forms in interconnected features over length scales greater than 1mm (A). Bacteria create EPS (B). A single bacterium attached to the surface in the presence of nanoparticles (C).

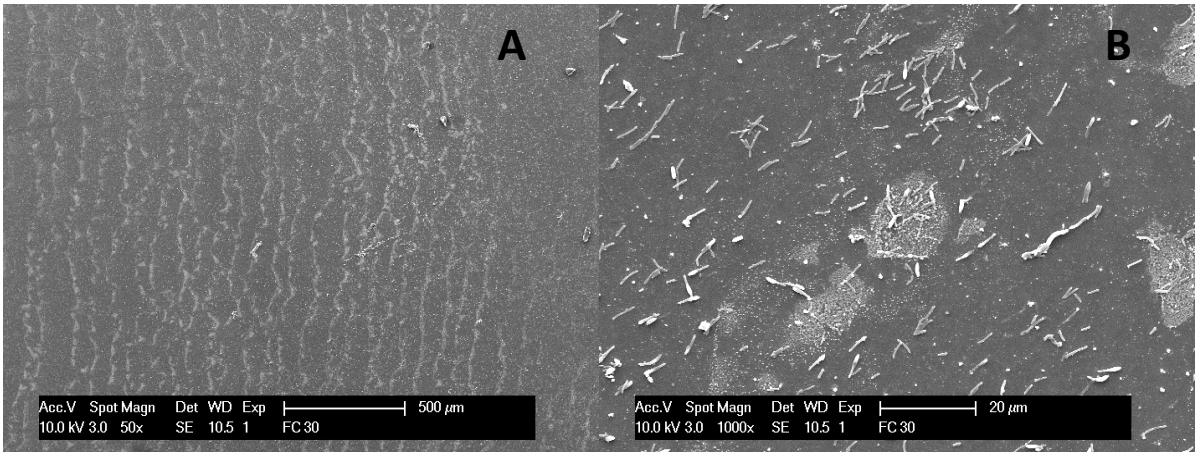

Figure 83: When areal coverage of silver is high (24.2% here) biofilm growth is inhibited. AgNP lines visible (A). Bacteria attached but did not form biofilm (B)

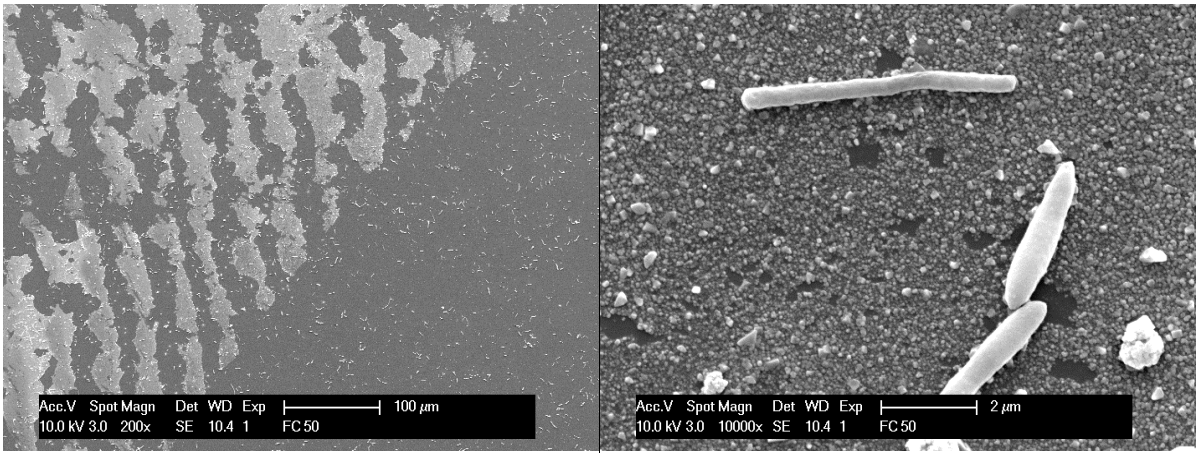

Figure 84: On samples with the highest areal coverage of AgNP (45.2%) bacteria were spread across the surface (left), including directly on AgNP coating (right).

Figure 82, Figure 83 and Figure 84 demonstrate the evolution of biofilm with increasing amounts of silver coverage. Starting with the lowest density AgNP coating (6.0% in Figure 82) biofilm is spread over the surface but concentrated in groups of less than 500 µm that are interconnected. Bacteria in areas of dense biofilm growth have formed the same kind of structures seen in the control, with the presence of EPS. Finally, a single bacterium is shown at high magnification in Figure 82b with AgNPs visible on the substrate below. Despite clear interaction with surface deposited AgNPs bacteria attached and formed biofilm. Biofilm has grown over areas of the surface that are certainly coated with AgNP. It is not clear if bacteria

attached directly on the nanoparticles or if they attached where silver was not present and then overgrew the silver, using defense mechanisms described above to resist toxicity of the surface coating. This low density AgNP coating did not significantly inhibit biofilm growth.

However, when areal density of AgNPs increased to 24.2% the growth of biofilm in some samples was significantly reduced, as seen in Figure 83. At low magnification the characteristic deposition lines were visible across the sample. Bacteria were also spread evenly over the sample. However, they were individually separated and did not form the complex structures associated with healthy biofilm growth. It is possible that the bacteria are planktonic and are visible here because they were fixed to the surface during drying and processing but the evidence in Figure 83b suggests that bacteria attached to the surface but failed to form biofilm. The bacteria in the image are nearly all oriented with the long axis parallel to other nearby bacteria. This could be because bacteria orient themselves parallel to the direction of liquid flow to reduce shear force. Despite the evidence that bacteria successfully attached they clearly did not form biofilm. One of the possible mechanisms of toxicity of silver is that ions cause cytogenetic damage to the DNA that do not kill bacteria but effectively inactivate them by eliminating the ability to reproduce. In this case, silver could cause genetic damage that prevents bacteria from activating the genes needed to excrete EPS and form biofilm.

Biofilm was similarly inhibited in samples with high density AgNP coating (45.2% coverage). Figure 84 shows both a low magnification image of the surface with thick AgNP lines and a high resolution of several bacteria resting on AgNPs. Using SEM it is impossible to determine if bacteria are viable or if they have been killed or inactivated as described above.

One sample with 24.4% silver coverage provided a clear demonstration of the ability of AgNP coating to inhibit biofilm growth. Recall that when Si wafer samples are coated using

VCD they are held by a clip and lowered into a nanofluid containing AgNPs. The sample is then slowly removed from the liquid by a dip coater. The small portion (~2-3 mm) of the sample hidden under the clip is not coated in silver. Figure 85 shows the interface where AgNP coating stops and the uncoated region begins. Interestingly, while no biofilm formed on the AgNP coating (left) there was strong biofilm growth in the uncoated region (right). The leading edge of AgNP deposition is the brighter white line that cuts the image vertically. This also implies that biofilm can grow in the near vicinity of AgNP coating even when it is inhibited from growth directly on the covered area.

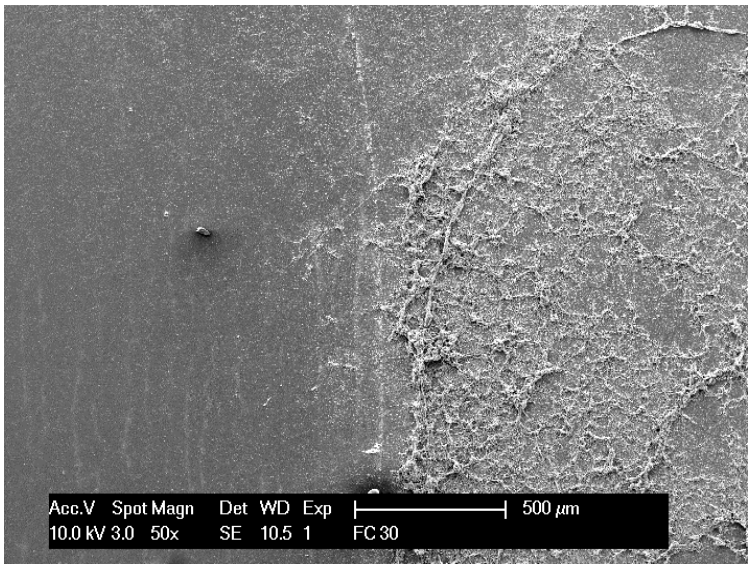

Figure 85: In this sample biofilm grew robustly on the portion of the sample that did not have deposited AgNP (right) where a clip held the sample during deposition. Biofilm did not grow on the portion with AgNP coating (left).

7.6.6 Biofilm growth intensity

Results from the prior section convincingly demonstrate that biofilm is inhibited by AgNPs deposited on surfaces by VCD. To quantify this effect a new quantity named biofilm growth intensity (BGI) was developed. As described above the calculation of BGI for a sample uses grayscale intensities in an image of the sample surface. Images were collected using a low

magnification lens on a digital optical microscope. The optics of this lens produce an image such that biofilm appear white against the mostly black background of the Si wafer substrate. Areas of dense biofilm are brighter than where growth is sparse. The example images in Figure 86 show the decline in biofilm from the control (A) to the sample with the highest concentration of AgNPs (D). BGI is calculated from each of the images using a Matlab script that was described above and can be found in Appendix B. During this process intensities of distinct blocks of each images are separated into bins. Histograms in Figure 87 show the distribution of intensities for two samples – the control with no silver and the high density AgNP sample.

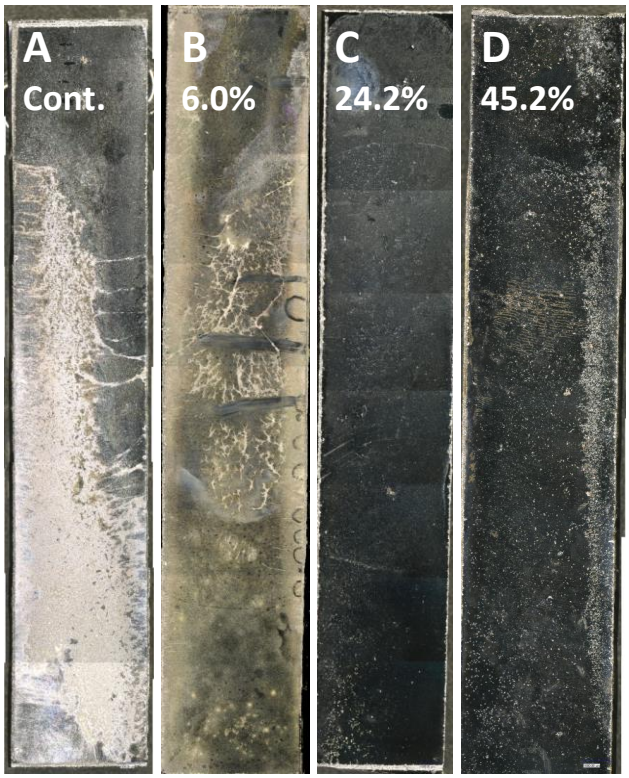

Figure 86: AgNP coated Si wafer samples after biofilm culture in a flow cell. Biofilm (white) grows strongly on the negative control. Percentage of AgNP in coating is shown for each sample.

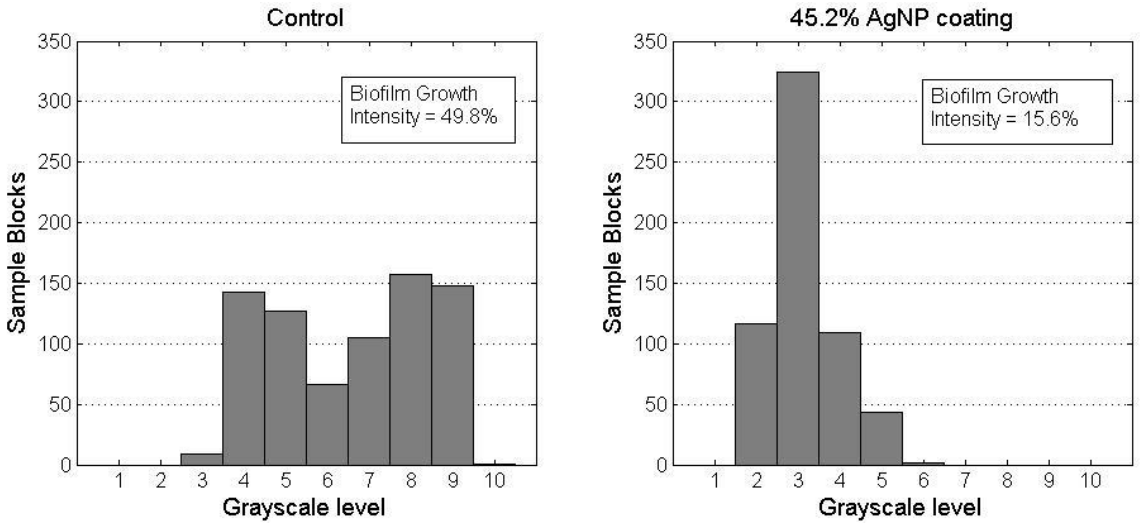

Figure 87: Histograms of block grayscale intensity data for control (left) and 50% AgNP coated (right). A broad range of gray levels in the control indicate of biofilm growth (BGI = 49.8%). The narrow plot for the AgNP coated sample indicates a dark surface and little bacterial growth (BGI = 15.6%).

Grayscale intensities in the control image that are shown in Figure 87 are spread out and include a significant amount of high intensity areas. BGI for that sample was 49.8%. By contrast the histogram for the sample with high density AgNP coating is heavily weighted to the low end of grayscale intensities, a result of the lack of biofilm and prevalence of exposed substrate, which is dark. The BGI for this sample was 15.6%. In all, BGI was calculated for 12 samples in three independent repeats comparing a control wafer to three AgNP coated samples. A background was also subtracted to control for the brightness contributed by the substrate and deposited silver.

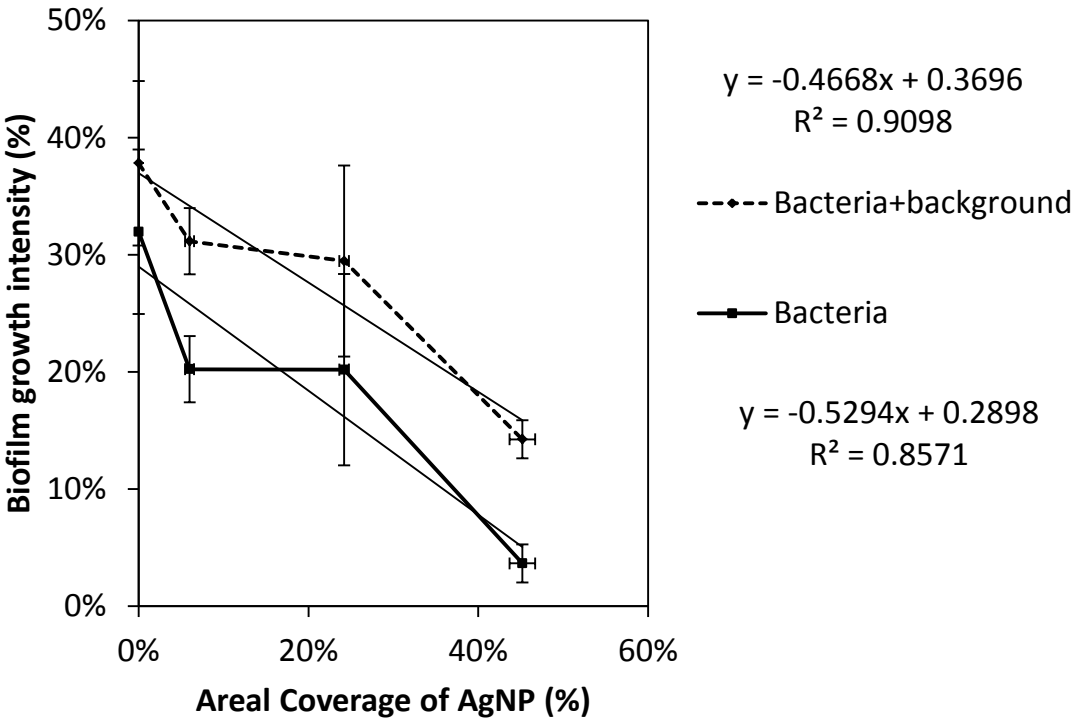

Figure 88: Biofilm growth intensity of *M. smegmatis* cultured in a flow cell as a function of areal coverage of AgNP. Dashed line shows raw BGI. Solid line shows adjusted BGI with background removed. Linear regression lines included for both series. Trends are significant negative slope ($p<0.05$). Error bars show SEM N=3. Horizontal error bars show SEM of areal coverage measurement.

Figure 88 shows average biofilm growth intensities plotted against areal coverage of AgNP. The raw BGI calculated from each image is shown as a dashed line and the BGI with background removed is shown with a solid line. With background removed BGI should represent only the growth of biofilm. Linear regression lines are shown both series. The data are linear with negative slope and R^2=0.9098. Statistical analysis showed that the slope is significantly different from zero ($p<0.05$). This statistical analysis proves that AgNP coatings have a negative effect on biofilm growth intensity. Also, the effect is greater for higher areal coverage of silver.

Recall that in the previous section heat treatment was applied to some samples to improved durability. However, whether or not this heat treatment would affect antibacterial efficacy was not known. One flow cell experiment was performed with samples that had been heated to 200 °C. BGIs were calculated and compared to the BGIs measured for non-heated

AgNP coatings. The results are shown in Figure 89. Again, linear regression was used and the data was linear with R^2=0.8896. The slope was negative and was actually higher magnitude than the slope from non-heated samples, -0.8896 versus -0.4668. This implies that the heat treated samples were more effective at inhibiting biofilm. However, there is not enough data to conclusively state this. Statistical analysis of covariance was used to show that the linear regression of the heat-treated data is not significantly different from the untreated data ($p<0.05$). Heat treated samples are likely just as effective at inhibiting surface formation of biofilm.

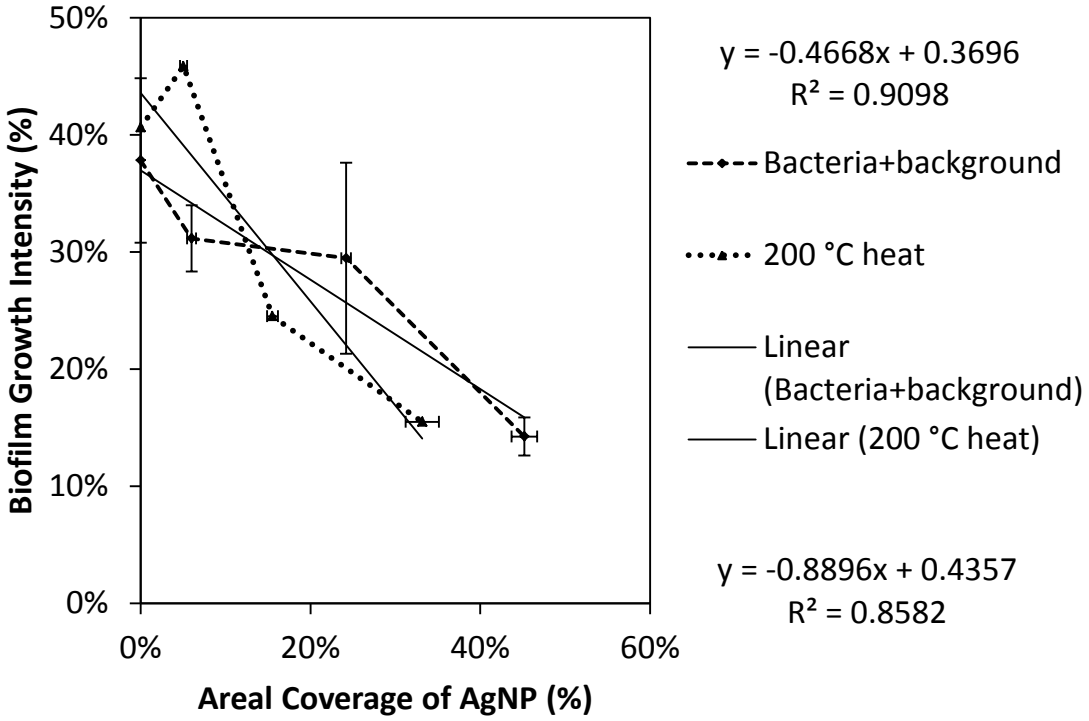

Figure 89: Biofilm growth intensity of *M. smegmatis* cultured in a flow cell as a function of areal coverage of AgNP for heat treated (dotted line) and untreated (dashed line) samples. Linear regression lines for both series included. Slope of regression lines is not significantly different ($p>0.05$). Heat treatment did not decrease antibiofilm efficacy of AgNP coatings.

7.6.7 Discussion

Deposited AgNPs prevented colonization and growth of mycobacterial biofilms of *M. smegmatis* and *M. avium* on porous membrane filters. However, *M. avium*, the significant human

pathogen, was significantly more resistant to this antibacterial strategy. This underscores the importance of testing new antibacterial technologies with actual pathogens rather than substituting laboratory-friendly species like *M. smegmatis* or *E. coli*. The size of *M. smegmatis* colonies was reduced with increasing concentration of AgNP.

The membrane culture method described in this study has shown promise as a protocol for the evaluation of antibacterial surface coatings. Future research may also benefit from this method as a simpler first evaluation of new antibacterial techniques, including advanced deposition methods. Such future work may include more directed deposition of silver nanoparticles to evaluate the efficacy of a variety of spatial distributions of particles on surfaces.

Similarly, the antibacterial and antibiofilm efficacy of surface deposited AgNPs was measured under natural conditions in a flow cell. The flow cell was used to emulate the conditions in which biofilms grow in the environment. A statistically significant negative trend was measured for biofilm growth intensity when measured across a series of samples with varying areal coverage of AgNP. Biofilm growth was not inhibited by low density AgNP coating (<10% areal coverage) but was significantly reduced and almost completely eliminated by high density coating (>40% areal coverage). Bacteria appear to have attached to the surface successfully but were prevented from developing into biofilm by the presence of silver.

Silver nanoparticle coatings could play an important role in combating mycobacterial infections in medical settings, especially in showerheads, where they could be used to prevent or slow the growth of biofilms. The anti-mycobacterial activity of AgNP presented here is a first step to implementing such antibacterial coatings to prevent mycobacterial contamination in water filters for medical applications and elsewhere.

8.0 CONCLUSIONS

1. The morphology and distribution of AgNPs in a low-cost water filter material was determined to be controlled by drying dynamics.

AgNPs were deposited by soaking the filter material in a nanofluid containing the nanoparticle and then drying in air. During drying, AgNPs were segregated preferentially to the surfaces from which drying occurred. Analysis of a drying curve showed that as much as 90.3% of AgNPs could be returned to the surface during drying, a condition that is not optimal for antibacterial efficacy.

2. In planktonic culture *M. smegmatis* population was reduced by 98.7% by 100 µM AgNP concentration. By comparison, *M. avium* and *M. marinum* were reduced by 97.4% and 85%, respectively, in planktonic culture with 860 µM AgNP.

The higher resistance of *M. avium* and *M. marinum* could be explained by the hypothesis that these two aquatic bacteria have evolved natural resistance as a result of exposure to ionic silver in the natural environment. Indeed, a significant risk of employing AgNPs as an antibacterial strategy is the risk of proliferating AgNPs into the environment and inducing silver resistance in environmental bacteria.

3. Resistant mutation was observed in *M. smegmatis* that were cultured in agar plates enriched with AgNPs.

A group of resistant colonies was extracted and independently cultured. One of these resistant mutant strains, Ag-r[1], was re-exposed to AgNP alongside the unmodified strain of *M. smegmatis*, which is called MC[2] 155. Over a range of concentrations of AgNP from 6.25 to 50 µM Ag-r[1] was much less susceptible to the toxic effects of silver than MC[2] 155. In one case, Ag-r[1] grew by more than 10,000 percent while MC[2] 155 was reduced by 50%. Also, the Ag-r[1] strain was resistant to silver ions from 2.5 to 20 µM. That exposure to AgNP induced resistance to Ag^+ is interesting because it implies that the mechanism of AgNPs is governed by the release of Ag^+ into the local environment, at least partially.

Ag-r[1] grew as quickly as MC[2] 155 with a doubling time of 7.7 hours as compared to 7.4 hours. Ag-r[1] was also resistant to isoniazid, a typical first line antibiotic used for mycobacterial infections. On the other hand, Ag-r[1] was more susceptible to high concentrations of $CuSO_4$ and $ZnSO_4$. Silver resistant mutation was easily and quickly induced in a population of environmental mycobacteria by merely exposing it to AgNPs. Such resistance could occur in the natural environment as silver is increasingly used in antibacterial technologies. The release of silver into the environment or into localized environments like water distribution systems could increase the prevalence of silver resistant mutants. Steps should be taken to mitigate these risks.

4. The areal coverage of nanoparticles deposited by vertical colloidal deposition on oxidized silicon substrates did not agree well with existing theory

Diao's theory for VCD was used to predict the areal coverage based on the deposition conditions of speed and AgNP concentration, as well as a number of controlled experimental conditions that were either calculated or measured. Areal coverage results were compared to the

predictions made by the theory and they did not match well overall, though general trends, such as the direct relationship of areal coverage to concentration and inverse relationship to deposition speed, were found in the experimental data. VCD coatings were characterized morphologically by lines of AgNPs perpendicular to the motion of the meniscus during deposition. The lines could be the result of a stick-slip mechanism that is common in the classic coffee stain deposition but not accounted for in Diao's theory.

VCD was used to control the morphology of deposited AgNPs. The width, density and thickness of deposited lines, as well as the overall areal coverage could be manipulated by varying just deposition speed and AgNP concentration. Areal coverage was varied between 5 and 50%. Both AgNP line width and density were influenced by speed and concentration in a way predicted by the functional dependencies in Diao's theory. Applying the VCD deposition techniques presented here could allow one to manipulate a AgNP coating and optimize it for antibacterial efficacy.

5. Low temperature heat treatment improved the durability of silver nanoparticle coatings

Durability was measured by coating samples with AgNP by VCD and then subjecting those samples to liquid flow in a flow cell. Losses in both areal coverage and coating thickness were documented. With no post-deposition processing AgNP coatings were highly susceptible to leaching from the surface during liquid flow, especially for high areal density coatings. In the most extreme case a coating of 45.2% areal coverage was reduced to just 8.0% after 72 hours. Likewise, coating thickness was reduced significantly across all depositions implying that AgNP was leached from the surface even when there was no evidence of loss of areal coverage. However, a simple heat treatment at 200 °C was usually sufficient to reduce or eliminate

leaching of AgNPs from coatings. This important AgNP coating property was dramatically improved by a simple change in processing.

6. Silver nanoparticles inhibited biofilm growth in static and flow cell conditions but did not entirely prevent it

AgNP was deposited on membrane filters, which then inhibited the growth of *M. smegmatis* and *M. avium*. As also seen in planktonic culture *M. smegmatis* was more susceptible to AgNPs than *M. avium*, which were reduced by 99.99% and 40%, respectively, when cultured on membranes with 2.2 g/l AgNP coating. Growth of bacterial colonies was delayed by the presence of AgNP and the size of colonies was reduced with increasing AgNP concentration.

The growth of biofilm was also inhibited on AgNP coated samples in a flow cell. In a parallel channel flow cell, biofilm of *M. smegmatis* grew robustly on control samples. With increasing areal coverage of AgNP from 6.0% to 45.2% the viability of biofilm was reduced. A new measure, biofilm growth intensity, was introduced to quantify the extent of biofilm growth. Average BGI was reduced from 32% in the control to 4% for the highest density AgNP coating. There was a statistically significant negative trend for BGI with relation to AgNP areal coverage. Using heat treatment to improve durability of AgNP coatings did not negatively impact the ability to inhibit biofilm.

Each of the conclusions of this research has contributed to improving water treatment technologies that use AgNPs. This research resulted in three concrete recommendations that could improve the performance of AgNP coated low-cost ceramic water filters. First, filters should be dried such that the surface of the filter dries evenly to improve the distribution of AgNPs. Second, filters should be reheated to at least 200 °C after deposition of AgNP to improve durability and extend lifetime. Finally, since AgNPs are preferentially deposited at the

surface, cleaning practices should be modified to reduce scrubbing of the surface, which would result in loss of AgNPs.

Also, this research highlighted the risks of disseminating AgNPs into natural or enclosed environments. Simply through exposure a species of environmental mycobacteria mutated to resist AgNP toxicity. The modified strain was also resistant to a common antibiotic. Using silver to kill bacteria is highly effective and shows great potential for new technologies. However, such an approach does not come without risks. Desorption of nanoparticles from the surface may cause them to proliferate in the local environment. The full extent of these risks is not known and must be more thoroughly investigated for AgNPs and other nanomaterials. Results from this study proved that simple processing techniques like heat treatment can be used to improve durability.

Two novel techniques for measuring the effect of deposited AgNP on biofilm growth were demonstrated. The porous membrane protocol is a well-controlled alternative that strikes a balance between overly simplified planktonic exposure experiments and overly complex flow cell or experiments in natural conditions. It could be used as a protocol to screen new antibacterial coatings against a wide variety of bacterial species. When the complexity of the flow cell is necessary, this research presented a method to quantify the growth and intensity of biofilm. In summary, the principal hypothesis of this research was confirmed. AgNPs were demonstrated to enhance water treatment technologies by inhibiting growth of planktonic bacteria and biofilms.

9.0 FUTURE WORK

There are numerous questions and objective that were beyond the scope of this research. However, they are important to extend understanding and should be explored in future research. For example, the precise nature of the genetic mutation that induced silver resistance in the Ag-r[1] strain of *M. smegmatis* is not known. This could be determined by sequencing the genomes of Ag-r[1] and MC[2] 155 and comparing them. After isolating the mutation, the final step to confirm that mutation caused resistance would be to splice the non-mutated gene back into Ag-r[1] and measure for silver resistance to see if it has been removed. This work could also confirm hypotheses about the mechanism of AgNP toxicity that assume AgNPs release Ag^+ ions that must pass through the cell membrane to kill bacteria.

VCD has been demonstrated with nano-sized particles, but the theoretical basis of the model has not been verified in this regime. An extension of Diao's theory that accounts for the stick-slip mechanism would be a welcome extension. Also, lowering the pH of the nanofluid will theoretically lower the barrier to attachment and more nanoparticles will be firmly deposited. The pH could be modified by adding citric or carbonic acid to the nanofluid. Preliminary experiments have shown that reducing the pH of the nanofluid to 6 or 5 does not adversely affect the stability of the colloid.

Deposition could also be studied by varying other variables that contribute to areal coverage in VCD. Examples are contact angle, particle size, temperature and viscosity of fluid.

In particular, reducing particle size would increase surface area to volume ratio, which could enhance antibacterial activity. However, lowering particle size might also lead to a short antibacterial lifetime as silver ions leech. VCD is favored below ~60 ° contact angle. Increasing the contact angle during VCD may reduce the prevalence of deposition lines and result in more uniform AgNP coatings.

VCD is only one possible deposition method. Others include spray coating and spin coating. There are also techniques that can be used to pattern particles on surfaces. Any of these methods are good candidates for deposition techniques that could be used to achieve a more even AgNP distribution, higher AgNP durability, and even increased antibiofilm efficacy. Further studies could investigate the effects of AgNP size or shape, both of which have been shown to change antibacterial efficacy in planktonic culture.

In this research a quantity was proposed to measure biofilm growth intensity (BGI). The measurement of this quantity should be tested for robustness. For example, this could be performed with biofilm of other bacterial species and with other substrate materials. Also, the choice of scale should be optimized. In this research, images were divided into 500 x 500 μm blocks. Stereological techniques could be used to determine appropriate block size for various biofilm growth conditions.

Biofilms are robust and will grow in virtually any environment, including on silver coated surfaces. Often, new biofilm is seeded by sloughed off parts of another biofilm. The viability of such downstream biofilms should be investigated to see if silver resistance is imparted or if viability is affected.

Finally, the effect of a deposited silver nanoparticle coating on planktonic bacteria could be measured. The purpose of this experiment would be to show that contact with a deposited film

of silver can affect the viability of planktonic bacteria even if it does not become attached to the surface. This is an important consideration in flow applications like showerheads and water filters where inactivation or killing of planktonic bacteria is the goal.

10.0 ACKNOWLEDGEMENTS

I would like to acknowledge Dr. Ian Nettleship for his guidance. I would like to thank Dr. Anil Ojha and Dr. Islam Mohammad. Their collaboration, instruction, and expertise in microbiology have been instrumental. Kathy Kulka was helpful for all biological experiments. Ziye Xiong was extremely helpful for AFM. I would also like to thank the undergraduates who have worked on various aspects of this project: Nicole Ostrowski, Jacquelyn Speakman, Danielle Pooler, Joe Landry, Michael Melia, Doug Knopp, Andrew Beck, Nick Drake and Khaled Abdelrahman. Also, the Materials Micro characterization laboratory at the University of Pittsburgh was instrumental in this work, especially the assistance of Al Stewart and Cole van Ormer.

APPENDIX A

RECIPE FOR BIOFILM MEDIA

In 900 ml Millipore water add

13.6 g KH_2PO_4

2 g Ammonium Sulfate

Adjust pH to 7.2 with KOH pellet

Add 0.5 mg $FeSO_4.7H_2O$

5g casamino acid

Autoclave at 121 °C for 20 min on liquid cycle

Store at room temperature

Just before assay reconstitute 100 ml of biofilm media with

94 ml biofilm media base from above

5 ml 40% glucose

1 ml 0.1M $CaCL_2$ (anhydrous)

100 µl 1M $MgSO_4$ (anhydrous)

APPENDIX B

MATLAB PROGRAMS

```
% SEMthresholderbatch.m by Curtis Larimer
inputfile = input('What is the first file name in the batch(including
extension)?', 's');
p = which(inputfile);
inputstem = input('What is the filename stem?', 's');
stem = strcat(inputstem,'*.tif');
filelist = dir([fileparts(p) filesep stem]);
fileNames = {filelist.name;
nImages = length(fileNames);
Coveragetable = zeros(nImages,1);
for k = 1:nImages
    SilverCoverage = SEMthreshfunc(fileNames{k);
    Coveragetable(k,1) = SilverCoverage;
end
Coveragetable

%SEMthreshfunc.m

function [SilverCoverage] = SEMthreshfunc(inputfile)
I = imread(inputfile); %reads the input file
[height width] = size(I);
otsu = graythresh(I);
K = im2bw(I,otsu);
se = strel('disk',1);
L = imclose(K,se);
M = bwareaopen(L, 10);
BX=M;  % Assign image matrix
d=size(BX);   % calculate size of image - it should be variable
SilverCoverage = sum(sum(BX))/(d(1)*d(2)); % porosity = total_void
pixels/total_pixels

%biofc.m
clear all
[FileName,PathName] = uigetfile('C:\*.tif','Select the image file');
addpath(PathName);
I = imread(FileName);
J = rgb2gray(I);
[height width] = size(J);
```

```
rows = floor(height/131);
columns = floor(width/131);
blockmat = zeros(rows,columns);
mx = max(max(J));
for i = 1:rows
    for j = 1:columns
        blocksum = sum(sum(J((1+131*(i-1)):131*i, (1+131*(j-1)):131*j)));
        blockmean = blocksum/131^2;
        blockmat(i,j) = blockmean;
    end
end
binsize = floor(mx/10);
edges =
[0,binsize*1,binsize*2,binsize*3,binsize*4,binsize*5,binsize*6,binsize*7,bins
ize*8,binsize*9,binsize*10];
bct = floor(binsize/2);
bctr = [bct,bct,bct,bct,bct,bct,bct,bct,bct,bct];
bincenters = single(edges(1,1:10)+bctr);
% figure;
% hist(blockmat,bincenters);
[n,bin] = histc(blockmat,edges);
bin;
n = transpose(sum(transpose(n)));
intensities = [0; .1; .2; .3; .4; .5; .6; .7; .8; .9; 1];
BinBGI = n.*intensities;
BinBGItot = sum(BinBGI);
Blocktot = rows*columns;
BGI = BinBGItot/Blocktot
```

APPENDIX C

PROTOCOL AND TIMELINE FOR FLOW CELL EXPERIMENTS

Prepared in advance: Silver nanoparticle suspension

1. Add desired volume or mass of silver nanoparticles to DI water.
2. Mix well. Sonicate for 30 minutes with ultrasonic horn.
3. Dilute as necessary
4. Re sonicate in water bath just before deposition

Preparation of Si wafer samples:

1. Cut 4 inch Si wafer to 6x35mm rectangular samples using diamond tipped scribe
2. Clean samples with compressed air
3. Place samples in shallow bath of RCA etch solution and heat to 100 ^{o}C for 15 minutes
    a. RCA etch: Hydrogen peroxide:Ammonium Hydroxide:Water in 1:1:5 ratio
4. Remove samples and placed immediately into a bath of DI water
5. Remove samples one by one and rinse with Isopropyl Alcohol
6. Place rinsed sample on a folded Kimwipe with polished side up
7. Dry excess alcohol from the surface by evenly blowing compressed air from one end to the other
8. Repeat rinse and dry with each sample
9. Cover the samples with a plastic weigh boat, do not place in a sealed container like a petri dish
10. Wait 48 hours to begin VCD
11. Use dip coater to deposit nanoparticles on the sample
12. Place the sample in the clip, cover with the shroud, set parameters for deposition
13. Deposition may take 1-8 hours and can be done several weeks in advance of flow cell experiments
14. (optional) heat deposited samples on hot plate to anneal deposited silver

Preparation of bacterial culture:

1. Remove one vial of stock bacterial culture from frozen storage (-80 ^{o}C freezer in room 621).
    a. Common strains: *M. smegmatis* – MC^{2}155, Ag resistant mutant (+)
2. Let vial thaw and add to 45ml 7H9 culture media with 5ml ADC and 125 µl 20% tween in Erlenmeyer flask under sterile hood
3. Incubate on shaker at 37 ^{o}C for 2-3 days
4. Prepared culture can be kept at room temperature for 2-3 weeks and used for multiple experiments

Preparation of sterile media:

The following components are assembled to complete the portion of the flow cell that will be in the media jar:

1. 40 cm silicone tubing (1/32" ID)
2. Connecter – Female Luer lock to 1/16" ID
3. Male Luer cap
4. Place the tubing into the hole in a rubber stopper
5. Fill other holes in the stopper loosely with rolled kimwipe and secure in place with tape
6. Place the tube and stopper into a 1 l jar containing the biofilm media base as described in the first 8 steps of "Preparation of biofilm media" below
7. Secure the stopper with autoclave tape
8. Leave a ~10 cm section of tubing out of the top of the stopper
9. Enclose this section in an autoclave bag
10. Autoclave 121 ^{o}C liquid cycle
11. Continue with step 10 of "Preparation of biofilm media" below to finish biofilm media just before assay

Preparation of biofilm media

1. In a 1.5-2 l beaker add 900 ml Millipore water
2. Add stir bar and place on mixing plate
3. Add 13.6 g KH2PO4
4. Add 2 g ammonium sulfate
5. Adjust pH to 7.2 using KOH pellet
6. Add Trace (0.5mg) FeSO4.7H2O
7. Add 5 g casamino acid
8. Use funnel to move media to 1 l jar, including stir bar
9. Autoclave 121 ^{o}C 20 minutes liquid cycle
10. Allow to cool before beginning experiment. Can be stored at room temperature
11. Just before assay add 50 ml 40% glucose
12. Add 10 ml CaCl2 (anhydrous)

13. Add 1 ml $MgSO_4$ (anhydrous)
14. Stir well

Assembly of flow cell:

The following components are assembled in roughly the order that they can be added. See illustrations for details

1. Female luer cap
2. Connecter: Male Luer to 1/16” ID
3. 80 cm 1/32”ID silicone tubing
4. Connecter: 1/16” ID to 1/8” ID
5. Black tubing clamp
6. 7 cm 1/8” ID silicone tubing
7. Glass Flow Break
8. 25 cm 1/8” ID silicone tubing
9. White tubing clamp
10. Connecter: 1/8” ID to 3/32” ID
11. Black tubing clamp
12. 7.5 cm ¼” ID Clear PVC tubing
13. Two stainless steel tubing clamps
14. Connecter: 1/8” ID to 3/32” ID
15. Black tubing clamp
16. 25 cm 1/8” ID silicone tubing
17. White tubing clamp
18. Glass flow break
19. 40 cm 1/8” ID silicone tubing

Further Flow cell assembly

With tubing and connecters assembled in the order given above continue as follows:

1. Tighten black tubing clamps, leave white clamps open
2. Tighten one stainless steel clamp
3. Insert sample in the ¼”ID tubing
4. Tighten the other stainless steel clamp to enclose the sample
5. Label the flow cell with the sample details
6. Mark the ¼”ID tubing so it is clear which side of the sample is polished from outside the tubing
7. Fold the tubing carefully and place in an autoclave bag
8. Autoclave 121 ^{o}C 20 min dry cycle at the same time as the media prepared above

Inoculation and final preparation of flow cell (to be done in a sterile hood with gloves and standard measures to prevent contamination and infection)

1. Gather cooled flow cell and media from autoclave
2. Open autoclave bag
3. Tighten the stainless steel tubing clamps as the tubing may shrink in the autoclave
4. Secure tubing containing the sample with tape so polished side is facing up
5. Wipe the tubing above the sample with isopropanol using a cotton swab
6. Mix bacterial culture well on vortex mixer
7. Transfer ~0.3 ml bacterial culture to syringe fitted with 25G needle
8. Inject through the wall and leave three ~20 µl drops on the sample's polished surface
9. Wipe the tubing with alcohol again
10. Leave the flow cell for 2 hours so bacteria can begin to colonize the surface
11. Meanwhile steps 10-14 of biofilm media preparation can be completed
12. Remove luer caps from both the tubing in the media jar and the flow cell assembly
13. Connect the flow cell to the media jar
14. Transfer the fully assembled flow cell to warm room to begin flow

Starting flow cell (to be done in warm room)

1. Place sterile media jar next to peristaltic pump
2. Thread 80 cm section of 1/32" ID tubing through pump leaving enough excess tubing on either side to secure the tubing with tape
3. Using tape and fasteners secure the flow cell in a loop such that media will flow down through the first flow break, up through the tube containing the sample and down through the second flow break (see the image below for detail)
4. Lower the last piece of tubing into a 1 l waste jar containing ~50-100 ml TB coverage spray disinfectant
5. Cover the waste jar with foil
6. Turn on the peristaltic pump and raise rpm to 10-25. Using a higher flow rate initially will fill the flow cell quickly so it can be checked for leaks and trapped bubbles in the tubing
7. When media has fully covered the sample turn the flow rate down to 1 rpm
8. Observe periodically for 72-84 hours, watching for signs of infection or leaks. Cloudiness in the media, bad smell, excess growth in the tubes may indicate infection

Stopping the flow cell and removing samples

1. Check system for continuous flow and no infection
2. Close white tubing clamps on either side of the sample chamber
3. Turn off pump
4. Remove tubes from pump and begin to remove tape or fasteners from flow cell
5. Transfer flow cell, media jar and waste jar to a tray

6. Remove the flow cell from the warm room and take the sample to a sink where media can be safely disposed of.
7. Prepare a petri dish with ~10-15 ml formalin (5% formaldehyde)
8. Cut ¼" ID tubing just above the sample, taking safety precautions as highly infected liquid inside the chamber will spill out.
9. Remove the sample with a tweezers and immediately place in the formalin with the polished side up. Some bacteria will float away from the sample. These are not well attached biofilm.
10. Lightly swish the sample back and forth in the formalin for 5 seconds to remove any poorly attached bacteria.
11. Place a lid over the petri dish containing the sample and transfer to a sterile hood.
12. Leave the sample in formalin for 90-120 min.
13. While waiting the remaining media, waste liquid, jars and flow cell components can be cleaning and disposed of. Tubing and many components are disposable. The following components should be disinfected, cleaned and reused: White, black and stainless steel tubing clamps, glass flow break, rubber stopper, jars.
14. After 90-120 min prepare small baths of Millipore water and isopropanol.
15. Remove sample from formalin and rinse gently first in water and then in alcohol. Be careful not to scrape or remove biofilm from the wafer surface.
16. Finally, place the sample in an empty petri dish to dry overnight.

REFERENCES

1. Hippocrates. *On Airs, Waters, and Places*. 400 BCE; Available from: http://classics.mit.edu/Hippocrates/airwatpl.html.

2. S. Hempel, *The Strange Case of the Broad Street Pump: John Snow and the Mystery of Cholera*. 2007, Berkeley: University of California Press.

3. *Fact Sheet No. 107: Cholera*. 2011 [cited 2011 18 Nov]; Available from: http://www.who.int/mediacentre/factsheets/fs107/en/index.html.

4. H. Lara, N. Ayala-Nunez, L. Ixtepan-Turrent, and C. Rodriguez-Padilla, *Mode of antiviral action of silver nanoparticles against HIV-1*. Journal of Nanobiotechnology, 2010. **8**(1): p. 1.

5. C. Baker, A. Pradhan, L. Pakstis, D.J. Pochan, and S.I. Shah, *Synthesis and antibacterial properties of silver nanoparticles.* Journal of Nanoscience and Nanotechnology, 2005. **5**(2): p. 244-249.

6. W.R. Hill and D.M. Pillsbury, *Argyria: the pharmacology of silver*. 1939: The Williams & Wilkins company.

7. M.J. Sweet and I. Singleton, *Silver Nanoparticles. A Microbial Perspective*. 2011. p. 115-133.

8. J. Theron, J.A. Walker, and T.E. Cloete, *Nanotechnology and Water Treatment: Applications and Emerging Opportunities.* Critical Reviews in Microbiology, 2008. **34**(1): p. 43-69.

9. K.A. Dunphy Guzman, M.R. Taylor, and J.F. Banfield, *Environmental Risks of Nanotechnology: National Nanotechnology Initiative Funding, 2000−2004.* Environmental Science & Technology, 2006. **40**(5): p. 1401-1407.

10. *Combating Waterborne Disease at the Household Level*. 2007, Geneva, Switzerland: WHO Press. 36.

11. *Meeting the MDG Drinking warer and sanitation target: A mid-term assessment of Progress*, WHO/UNICEF, Editor. 2004, WHO and UN Children's Fund: Geneva.

12. *Progress on drinking water and sanitation: Special focus on sanitation*, WHO/UNICEF, Editor. 2008, UNICEF and World Health Organization: Geneva.

13. C.J. Vorosmarty, P. Green, J. Salisbury, and R.B. Lammers, *Global Water Resources: Vulnerability from Climate Change and Population Growth.* Science, 2000. **289**(5477): p. 284-288.

14. O. Varis and L. Somlyody, *Global urbanization and urban water: Can sustainability be afforded?* Water Science and Technology, 1997. **35**(9): p. 21-32.

15. M.D. Sobsey, C.E. Stauber, L.M. Casanova, J.M. Brown, and M.A. Elliott, *Point of Use Household Drinking Water Filtration: A Practical, Effective Solution for Providing Sustained Access to Safe Drinking Water in the Developing World.* Environmental Science & Technology, 2008. **42**(12): p. 4261-4267.

16. PottersforPeace.org. *Potters For Peace*. [Online] 2009 [cited 2009 12/6/2009]; Available from: http://www.pottersforpeace.org.

17. D. van Halem, *Ceramic silver impregnated pot filters for household drinking water treatment in developing countries*, in *Department of Water Management*. 2006, Delft University of Technology. p. 144.

18. V.A. Oyanedel-Craver and J.A. Smith, *Sustainable Colloidal-Silver-Impregnated Ceramic Filter for Point-of-Use Water Treatment.* Environmental Science & Technology, 2007. **42**(3): p. 927-933.

19. J. Brown, M.D. Sobsey, and D. Loomis, *Local Drinking Water Filters Reduce Diarrheal Disease in Cambodia: A Randomized, Controlled Trial of the Ceramic Water Purifier.* Am J Trop Med Hyg, 2008. **79**(3): p. 394-400.

20. L.G. Donowitz, R.P. Wenzel, and J.W. Hoyt, *High risk of hospital-acquired infection in the ICU patient.* Critical care medicine, 1982. **10**(6): p. 355-7.

21. M. Sabria and V.L. Yu, *Hospital-acquired legionellosis: solutions for a preventable infection.* The Lancet Infectious Diseases, 2002. **2**(6): p. 368-373.

22. D.L. Julia, *Candida biofilms and their role in infection.* Trends in Microbiology, 2003. **11**(1): p. 30-36.

23. A.G. Gristina, P. Naylor, and Q. Myrvik, *Infections from biomaterials and implants: a race for the surface.* Medical progress through technology, 1988. **14**(3-4): p. 205-24.

24. *Guidelines for Drinking-water Quality*. 3rd ed. ed. Vol. 1. 2008, Geneva: WHO Press.

25. J.M. Schierholz, L.J. Lucas, A. Rump, and G. Pulverer, *Efficacy of silver-coated medical devices.* Journal of Hospital Infection, 1998. **40**(4): p. 257-262.

26. J.A. Smith, V. Oyandel-Craver, E.N. Kallman, K. Kline, R. Massey, and D. Restivo, *Mechanistic laboratory and field evaluation of sustainable point-of-use water treatment technologies to remove turbidity and deactivate coliform bacteria*, in *Trip report presented at the NSF IREE 2008 Grantees Conference*. 2008.

27. C. Larimer, N. Ostrowski, J. Speakman, and I. Nettleship, *The segregation of silver nanoparticles in low-cost ceramic water filters.* Materials Characterization, 2010. **61**(4): p. 408-412.

28. G. Bhabra, A. Sood, B. Fisher, L. Cartwright, M. Saunders, W.H. Evans, A. Surprenant, G. Lopez-Castejon, S. Mann, S.A. Davis, L.A. Hails, E. Ingham, P. Verkade, J. Lane, K. Heesom, R. Newson, and C.P. Case, *Nanoparticles can cause DNA damage across a cellular barrier.* Nat Nano, 2009. **4**(12): p. 876-883.

29. D.H. Nies, *Microbial heavy-metal resistance.* Applied Microbiology and Biotechnology, 1999. **51**(6): p. 730-750.

30. J.J. Harrison, H. Ceri, and R.J. Turner, *Multimetal resistance and tolerance in microbial biofilms.* Nat Rev Micro, 2007. **5**(12): p. 928-938.

31. J.R. Morones-Ramirez, J.A. Winkler, C.S. Spina, and J.J. Collins, *Silver Enhances Antibiotic Activity Against Gram-Negative Bacteria.* Science Translational Medicine, 2013. **5**(190): p. 190ra81.

32. I. Sondi and B. Salopek-Sondi, *Silver nanoparticles as antimicrobial agent: a case study on E. coli as a model for Gram-negative bacteria.* Journal of Colloid and Interface Science, 2004. **275**(1): p. 177-182.

33. S. Pal, Y.K. Tak, and J.M. Song, *Does the Antibacterial Activity of Silver Nanoparticles Depend on the Shape of the Nanoparticle? A Study of the Gram-Negative Bacterium Escherichia coli.* Appl. Environ. Microbiol., 2007. **73**(6): p. 1712-1720.

34. Q. Li, S. Mahendra, D.Y. Lyon, L. Brunet, M.V. Liga, D. Li, and P.J.J. Alvarez, *Antimicrobial nanomaterials for water disinfection and microbial control: Potential applications and implications.* Water Research, 2008. **42**(18): p. 4591-4602.

35. J.R. Morones, J.L. Elechiguerra, A. Camacho, K. Holt, J.B. Kouri, J.T. Ramirez, and M.J. Yacaman, *The bactericidal effect of silver nanoparticles.* Nanotechnology, 2005. **16**(10): p. 2346-2353.

36. S. Shrivastava, T. Bera, A. Roy, G. Singh, P. Ramachandrarao, and D. Dash, *Characterization of enhanced antibacterial effects of novel silver nanoparticles.* Nanotechnology, 2007. **18**(22): p. 9.

37. D.W. Hatchett and H.S. White, *Electrochemistry of sulfur adlayers on the low-index faces of silver.* Journal of Physical Chemistry, 1996. **100**(23): p. 9854-9859.

38. K.B. Holt and A.J. Bard, *Interaction of silver(I) ions with the respiratory chain of Escherichia coli: An electrochemical and scanning electrochemical microscopy study of the antimicrobial mechanism of micromolar Ag.* Biochemistry, 2005. **44**(39): p. 13214-13223.

39. C.N. Lok, C.M. Ho, R. Chen, Q.Y. He, W.Y. Yu, H.Z. Sun, P.K.H. Tam, J.F. Chiu, and C.M. Che, *Proteomic analysis of the mode of antibacterial action of silver nanoparticles.* Journal of Proteome Research, 2006. **5**(4): p. 916-924.

40. Q.L. Feng, J. Wu, G.Q. Chen, F.Z. Cui, T.N. Kim, and J.O. Kim, *A mechanistic study of the antibacterial effect of silver ions on <I>Escherichia coli</I> and <I>Staphylococcus aureus</I>*. Journal of Biomedical Materials Research, 2000. **52**(4): p. 662-668.

41. M. Yamanaka, K. Hara, and J. Kudo, *Bactericidal actions of a silver ion solution on Escherichia coli, studied by energy-filtering transmission electron microscopy and proteomic analysis.* Applied and Environmental Microbiology, 2005. **71**(11): p. 7589-7593.

42. H.D. Kim and M.H. Kim, *Effect of nanoparticle deposition on capillary wicking that influences the critical heat flux in nanofluids.* Applied Physics Letters, 2007. **91**(1): p. 014104-3.

43. I. Sondi, D.V. Goia, and E. Matijevic, *Preparation of highly concentrated stable dispersions of uniform silver nanoparticles.* Journal of Colloid and Interface Science, 2003. **260**(1): p. 75-81.

44. C.N. Lok, C.M. Ho, R. Chen, Q.Y. He, W.Y. Yu, H. Sun, P.K.H. Tam, J.F. Chiu, and C.M. Che, *Silver nanoparticles: partial oxidation and antibacterial activities.* Journal of Biological Inorganic Chemistry, 2007. **12**(4): p. 527-534.

45. K.Y. Yoon, J.H. Byeon, J.H. Park, and J. Hwang, *Susceptibility constants of Escherichia coli and Bacillus subtilis to silver and copper nanoparticles.* Science of the Total Environment, 2007. **373**(2-3): p. 572-575.

46. P. Li, J. Li, C.Z. Wu, and Q.S. Wu, *Synergistic antibacterial effects of beta-lactam antibiotic combined with silver nanoparticles.* Nanotechnology, 2005. **16**(9): p. 1912-1917.

47. T. Abbott Chalew and K. Schwab, *Toxicity of commercially available engineered nanoparticles to Caco-2 and SW480 human intestinal epithelial cells.* Cell Biology and Toxicology, 2013. **29**(2): p. 101-116.

48. J. Balbus, K. Florini, R. Denison, and S. Walsh, *Protecting workers and the environment: An environmental NGO's perspective on nanotechnology.* Journal of Nanoparticle Research, 2007. **9**(1): p. 11-22.

49. K.L. Dreher, *Health and Environmental Impact of Nanotechnology: Toxicological Assessment of Manufactured Nanoparticles.* Toxicol. Sci., 2004. **77**(1): p. 3-5.

50. S.M. Hussain, L.K. Braydich-Stolle, A.M. Schrand, R.C. Murdock, K.O. Yu, D.M. Mattie, J.J. Schlager, and M. Terrones, *Toxicity Evaluation for Safe Use of Nanomaterials: Recent Achievements and Technical Challenges.* Advanced Materials, 2009. **21**(16): p. 1549-1559.

51. B. Jansen, M. Rinck, P. Wolbring, A. Strohmeier, and T. Jahns, *In vitro Evaluation of the Antimicrobial Efficacy and Biocompatibility of a Silver-Coated Central Venous Catheter.* J Biomater Appl, 1994. **9**(1): p. 55-70.

52. A. Nel, T. Xia, L. Madler, and N. Li, *Toxic potential of materials at the nanolevel.* Science, 2006. **311**(5761): p. 622-627.

53. L.K. Adams, D.Y. Lyon, and P.J.J. Alvarez, *Comparative eco-toxicity of nanoscale TiO2, SiO2, and ZnO water suspensions.* Water Research, 2006. **40**(19): p. 3527-3532.

54. G. Gosheger, J. Hardes, H. Ahrens, A. Streitburger, H. Buerger, M. Erren, A. Gunsel, F.H. Kemper, W. Winkelmann, and C. von Eiff, *Silver-coated megaendoprostheses in a rabbit model--an analysis of the infection rate and toxicological side effects.* Biomaterials, 2004. **25**(24): p. 5547-5556.

55. R. Handy, F. von der Kammer, J. Lead, M. Hassellöv, R. Owen, and M. Crane, *The ecotoxicology and chemistry of manufactured nanoparticles.* Ecotoxicology, 2008. **17**(4): p. 287-314.

56. P.J.A. Borm and D. Berube, *A tale of opportunities, uncertainties, and risks.* Nano Today. **3**(1-2): p. 56-59.

57. M.F. Hochella, Jr., S.K. Lower, P.A. Maurice, R.L. Penn, N. Sahai, D.L. Sparks, and B.S. Twining, *Nanominerals, Mineral Nanoparticles, and Earth Systems.* Science, 2008. **319**(5870): p. 1631-1635.

58. E. Hood, *Nanotechnology: Looking as we leap.* Environmental Health Perspectives, 2004. **112**(13): p. A740-A749.

59. K. Keller, *Nanotechnology and society.* Journal of Nanoparticle Research, 2007. **9**(1): p. 5-10.

60. I. Raskin, P.B.A.N. Kumar, S. Dushenkov, and D.E. Salt, *Bioconcentration of heavy metals by plants.* Current Opinion in Biotechnology, 1994. **5**(3): p. 285-290.

61. H.T. Ratte, *Bioaccumulation and toxicity of silver compounds: A review.* Environmental Toxicology and Chemistry, 1999. **18**(1): p. 89-108.

62. J.L. Barriada, A.D. Tappin, E.H. Evans, and E.P. Achterberg, *Dissolved silver measurements in seawater.* TrAC Trends in Analytical Chemistry, 2007. **26**(8): p. 809-817.

63. P.V. AshaRani, G.L.K. Mun, M.P. Hande, and S. Valiyaveettil, *Cytotoxicity and Genotoxicity of Silver Nanoparticles in Human Cells.* Acs Nano, 2009. **3**(2): p. 279-290.

64. M. Ahamed, M.S. AlSalhi, and M.K.J. Siddiqui, *Silver nanoparticle applications and human health.* Clinica Chimica Acta, 2010. **411**(23–24): p. 1841-1848.

65. R. Foldbjerg, D. Dang, and H. Autrup, *Cytotoxicity and genotoxicity of silver nanoparticles in the human lung cancer cell line, A549.* Archives of Toxicology, 2011. **85**(7): p. 743-750.

66. K. Kawata, M. Osawa, and S. Okabe, *In Vitro Toxicity of Silver Nanoparticles at Noncytotoxic Doses to HepG2 Human Hepatoma Cells.* Environmental Science & Technology, 2009. **43**(15): p. 6046-6051.

67. T.J. Beveridge, S.A. Makin, J.L. Kadurugamuwa, and Z. Li, *Interactions between biofilms and the environment.* FEMS Microbiology Reviews, 1997. **20**(3-4): p. 291-303.

68. L. Hall-Stoodley, J.W. Costerton, and P. Stoodley, *Bacterial biofilms: from the Natural environment to infectious diseases.* Nat Rev Micro, 2004. **2**(2): p. 95-108.

69. L. Hall-Stoodley and P. Stoodley, *Biofilm formation and dispersal and the transmission of human pathogens.* Trends in Microbiology, 2005. **13**(1): p. 7-10.

70. S.S. Socransky and A.D. Haffajee, *Dental biofilms: difficult therapeutic targets.* Periodontology 2000, 2002. **28**(1): p. 12-55.

71. J.M. ten Cate, *Biofilms, a new approach to the microbiology of dental plaque.* Odontology, 2006. **94**(1): p. 1-9.

72. R.B. Simmons, L.J. Rose, S.A. Crow, and D.G. Ahearn, *The Occurrence and Persistence of Mixed Biofilms in Automobile Air Conditioning Systems.* Current Microbiology, 1999. **39**(3): p. 141-145.

73. H. Beyenal, C. Donovan, Z. Lewandowski, and G. Harkin, *Three-dimensional biofilm structure quantification.* Journal of Microbiological Methods, 2004. **59**(3): p. 395-413.

74. R.H. Veeh, M.E. Shirtliff, J.R. Petik, J.A. Flood, C.C. Davis, J.L. Seymour, M.A. Hansmann, K.M. Kerr, M.E. Pasmore, and J.W. Costerton, *Detection of Staphylococcus aureus Biofilm on Tampons and Menses Components.* Journal of Infectious Diseases, 2003. **188**(4): p. 519-530.

75. M.J. O'Donnell, C.M. Tuttlebee, F.R. Falkiner, and D.C. Coleman, *Bacterial contamination of dental chair units in a modern dental hospital caused by leakage from suction system hoses containing extensive biofilm.* Journal of Hospital Infection, 2005. **59**(4): p. 348-360.

76. A. Molina, R. Del Campo, L. Máiz, M.-I. Morosini, A. Lamas, F. Baquero, and R. Cantón, *High prevalence in cystic fibrosis patients of multiresistant hospital-acquired methicillin-resistant Staphylococcus aureus ST228-SCCmecI capable of biofilm formation.* Journal of Antimicrobial Chemotherapy, 2008. **62**(5): p. 961-967.

77. L.M. Feazel, L.K. Baumgartner, K.L. Peterson, D.N. Frank, J.K. Harris, and N.R. Pace, *Opportunistic pathogens enriched in showerhead biofilms.* Proceedings of the National Academy of Sciences, 2009. **106**(38): p. 16393-16399.

78. K. Kierek and P.I. Watnick, *Environmental Determinants of Vibrio cholerae Biofilm Development.* Applied and Environmental Microbiology, 2003. **69**(9): p. 5079-5088.

79. P.S. Stewart and J. William Costerton, *Antibiotic resistance of bacteria in biofilms.* The Lancet, 2001. **358**(9276): p. 135-138.

80. T.M. Benn and P. Westerhoff, *Nanoparticle Silver Released into Water from Commercially Available Sock Fabrics.* Environmental Science & Technology, 2008. **42**(11): p. 4133-4139.

81. S. Silver, L. Phung, and G. Silver, *Silver as biocides in burn and wound dressings and bacterial resistance to silver compounds.* Journal of Industrial Microbiology & Biotechnology, 2006. **33**(7): p. 627-634.

82. E. Bardouniotis, H. Ceri, and M.E. Olson, *Biofilm Formation and Biocide Susceptibility Testing of Mycobacterium fortuitum and Mycobacterium marinum.* Current Microbiology, 2003. **46**(1): p. 0028-0032.

83. C.-T. Huang, S. Peretti, and J. Bryers, *Use of flow cell reactors to quantify biofilm formation kinetics.* Biotechnology Techniques, 1992. **6**(3): p. 193-198.

84. J. Kim, B. Pitts, P.S. Stewart, A. Camper, and J. Yoon, *Comparison of antimicrobial effect on biofilm of chlorine, silver ion and tobramycin.* Antimicrob. Agents Chemother., 2008: p. AAC.00054-07.

85. P. Lens, P. Stoodley, and T. Mahony, *Biofilms in medicine, industry and environmental biotechnology: characteristics, analysis and control*. 2003: IWA Publishing.

86. Z. Lewandowski and H. Beyenal, *Fundamentals of biofilm research*. 2007: CRC Press.

87. G.G. Geesey and A.C. Mitchell, *Need for Direct Measurements of Coupled Microbiological and Hydrological Processes at Different Scales in Porous Media Systems.* Journal of Hydrologic Engineering, 2008. **13**(1): p. 28-36.

88. A. Mollica and P. Cristiani, *On-line biofilm monitoring by "BIOX" electrochemical probe.* Water science and technology : a journal of the International Association on Water Pollution Research, 2003. **47**(5): p. 45-49.

89. G.A. Wistreich, *Microbiology laboratory: fundamentals and applications*. 2003: Prentice Hall.

90. P. Gangadharam and P. Jenkins, *Mycobacteria: Basic aspects*. 1998: Chapman & Hall.

91. C. Ratledge and J. Dale, *Mycobacteria: molecular biology and virulence*. 1999: Blackwell Science.

92. C.B. Inderlied, C.A. Kemper, and L.E. Bermudez, *The Mycobacterium avium complex.* Clin. Microbiol. Rev., 1993. **6**(3): p. 266-310.

93. C.-t. Chang, L.-y. Wang, C.-y. Liao, and S.-p. Huang, *Identification of Nontuberculous Mycobacteria Existing in Tap Water by PCR-Restriction Fragment Length Polymorphism.* Applied and Environmental Microbiology, 2002. **68**(6): p. 3159-3161.

94. T. Aronson, A. Holtzman, N. Glover, M. Boian, S. Froman, O.G.W. Berlin, H. Hill, and G. Stelma, *Comparison of Large Restriction Fragments of Mycobacterium avium Isolates Recovered from AIDS and Non-AIDS Patients with Those of Isolates from Potable Water.* Journal of Clinical Microbiology, 1999. **37**(4): p. 1008-1012.

95. T.P. Primm, C.A. Lucero, and J.O. Falkinham, III, *Health Impacts of Environmental Mycobacteria.* Clin. Microbiol. Rev., 2004. **17**(1): p. 98-106.

96. B. Petrini, *<i>Mycobacterium marinum</i>: ubiquitous agent of waterborne granulomatous skin infections.* European Journal of Clinical Microbiology & Infectious Diseases, 2006. **25**(10): p. 609-613.

97. T.P. Stinear, T. Seemann, P.F. Harrison, G.A. Jenkin, J.K. Davies, P.D.R. Johnson, Z. Abdellah, C. Arrowsmith, T. Chillingworth, C. Churcher, K. Clarke, A. Cronin, P. Davis, I. Goodhead, N. Holroyd, K. Jagels, A. Lord, S. Moule, K. Mungall, H. Norbertczak, M.A. Quail, E. Rabbinowitsch, D. Walker, B. White, S. Whitehead, P.L.C. Small, R. Brosch, L. Ramakrishnan, M.A. Fischbach, J. Parkhill, and S.T. Cole, *Insights from the complete genome sequence of Mycobacterium marinum on the evolution of Mycobacterium tuberculosis.* Genome Research, 2008. **18**(5): p. 729-741.

98. J. Kusnetsov, E. Iivanainen, N. Elomaa, O. Zacheus, and P.J. Martikainen, *Copper and silver ions more effective against Legionellae than against mycobacteria in a hospital warm water system.* Water Research, 2001. **35**(17): p. 4217-4225.

99. M.R. Rodgers, B.J. Blackstone, A.L. Reyes, and T.C. Covert, *Colonisation of point of use water filters by silver resistant non-tuberculous mycobacteria.* Journal of Clinical Pathology, 1999. **52**: p. 629.

100. A.R. Bielefeldt, M.W. Stewart, E. Mansfield, R. Scott Summers, and J.N. Ryan, *Effects of chlorine and other water quality parameters on the release of silver nanoparticles from a ceramic surface.* Water Research, (0).

101. M.C. Chen, S.D. Tsai, M.R. Chen, S.Y. Ou, W.H. Li, and K.C. Lee, *Effect of silver-nanoparticle aggregation on surface-enhanced Raman scattering from benzoic acid.* Physical Review B, 1995. **51**(7): p. 4507-4515.

102. M. Esmaili, S.M. Ghaffari, Z. Moosavi-Movahedi, M.S. Atri, A. Sharifizadeh, M. Farhadi, R. Yousefi, J.-M. Chobert, T. Haertlé, and A.A. Moosavi-Movahedi, *Beta casein-micelle as a nano vehicle for solubility enhancement of curcumin; food industry application.* LWT - Food Science and Technology, 2011. **44**(10): p. 2166-2172.

103. Y. Liu and R. Guo, *The interaction between casein micelles and gold nanoparticles.* Journal of Colloid and Interface Science, 2009. **332**(1): p. 265-269.

104. D. Lee, M.F. Rubner, and R.E. Cohen, *All-Nanoparticle Thin-Film Coatings.* Nano Letters, 2006. **6**(10): p. 2305-2312.

105. Z. Gemici, H. Shimomura, R.E. Cohen, and M.F. Rubner, *Hydrothermal Treatment of Nanoparticle Thin Films for Enhanced Mechanical Durability.* Langmuir, 2008. **24**(5): p. 2168-2177.

106. Y. Zhao, Z. Xu, X. Wang, and T. Lin, *Photoreactive Azido-Containing Silica Nanoparticle/Polycation Multilayers: Durable Superhydrophobic Coating on Cotton Fabrics.* Langmuir, 2012. **28**(15): p. 6328-6335.

107. A. Iwakoshi, T. Nanke, and T. Kobayashi, *Coating Materials Containing Gold Nanoparticles.* Gold Bulletin, 2005. **38**(3): p. 107-112.

108. DOE/Lawrence Berkely Laboratory (2009) *New Route to Nano Self-assembly Found*. ScienceDaily.

109. C.P. Martin, *Pattern Formation in Self-Organised Nanoparticle Assemblies*, in *School of Physics and Astronomy*. 2007, University of Nottingham: Nottingham. p. 174.

110. C.J. Brinker, Y. Lu, A. Sellinger, and H. Fan, *Evaporation-Induced Self-Assembly: Nanostructures Made Easy.* Advanced Materials, 1999. **11**(7): p. 579-585.

111. C.N.R. Rao and A.K. Cheetham, *Science and technology of nanomaterials: current status and future prospects.* Journal of Materials Chemistry, 2001. **11**: p. 2887-2894.

112. G.A. Ozin, K. Hou, B.V. Lotsch, L. Cademartiri, D.P. Puzzo, F. Scotognella, A. Ghadimi, and J. Thomson, *Nanofabrication by self-assembly.* Materials Today, 2009. **12**(5): p. 12-23.

113. J. Tang, G. Ge, and L.E. Brus, *Gas−Liquid−Solid Phase Transition Model for Two-Dimensional Nanocrystal Self-Assembly on Graphite.* The Journal of Physical Chemistry B, 2002. **106**(22): p. 5653-5658.

114. E. Rabani, D.R. Reichman, P.L. Geissler, and L.E. Brus, *Drying-mediated self-assembly of nanoparticles.* Nature, 2003. **426**(6964): p. 271-274.

115. J.J. Diao, J.B. Hutchison, G. Luo, and M.E. Reeves, *Theoretical analysis of vertical colloidal deposition.* The Journal of Chemical Physics, 2005. **122**(18): p. 184710-5.

116. J.J. Diao, F.S. Qiu, G.D. Chen, and M.E. Reeves, *Surface vertical deposition for gold nanoparticle film.* Journal of Physics D: Applied Physics, 2003. **36**(3): p. L25-L27.

117. J.J. Diao, J. Sun, J.B. Hutchison, and M.E. Reeves, *Self assembled nanoparticle wires by discontinuous vertical colloidal deposition.* Applied Physics Letters, 2005. **87**(10): p. 103113-3.

118. J.J. Diao and M.G. Xia, *A particle transport study of vertical evaporation-driven colloidal deposition by the coffee-ring theory.* Colloids and Surfaces A: Physicochemical and Engineering Aspects, 2009. **338**(1-3): p. 167-170.

119. L.M. Goldenberg, J. Wagner, J. Stumpe, B.-R. Paulke, and E. Gornitz, *Ordered Arrays of Large Latex Particles Organized by Vertical Deposition.* Langmuir, 2002. **18**(8): p. 3319-3323.

120. P. Jiang, J.F. Bertone, K.S. Hwang, and V.L. Colvin, *Single-Crystal Colloidal Multilayers of Controlled Thickness.* Chemistry of Materials, 1999. **11**(8): p. 2132-2140.

121. R.G. Shimmin, A.J. DiMauro, and P.V. Braun, *Slow Vertical Deposition of Colloidal Crystals: A Langmuir−Blodgett Process?* Langmuir, 2006. **22**(15): p. 6507-6513.

122. L. Wang and X.S. Zhao, *Fabrication of Crack-Free Colloidal Crystals Using a Modified Vertical Deposition Method.* The Journal of Physical Chemistry C, 2007. **111**(24): p. 8538-8542.

123. C. Larimer and I. Nettleship, *Deposition of silver nanoparticles by VCD.* Unpublished, 2009.

124. X.M. Lin, H.M. Jaeger, C.M. Sorensen, and K.J. Klabunde, *Formation of Long-Range-Ordered Nanocrystal Superlattices on Silicon Nitride Substrates.* The Journal of Physical Chemistry B, 2001. **105**(17): p. 3353-3357.

125. B.G. Prevo and O.D. Velev, *Controlled, Rapid Deposition of Structured Coatings from Micro- and Nanoparticle Suspensions.* Langmuir, 2004. **20**(6): p. 2099-2107.

126. R.D. Deegan, O. Bakajin, T.F. Dupont, G. Huber, S.R. Nagel, and T.A. Witten, *Capillary flow as the cause of ring stains from dried liquid drops.* Nature, 1997. **389**(6653): p. 827-829.

127. J.C. Loudet, A.M. Alsayed, J. Zhang, and A.G. Yodh, *Capillary Interactions Between Anisotropic Colloidal Particles.* Physical Review Letters, 2005. **94**(Copyright (C) 2009 The American Physical Society): p. 018301.

128. N.D. Denkov, O.D. Velev, P.A. Kralchevsky, I.B. Ivanov, H. Yoshimura, and K. Nagayama, *Two-dimensional crystallization.* Nature, 1993. **361**(6407): p. 26-26.

129. D. Stamou, C. Duschl, and D. Johannsmann, *Long-range attraction between colloidal spheres at the air-water interface: The consequence of an irregular meniscus.* Physical Review E, 2000. **62**(Copyright (C) 2009 The American Physical Society): p. 5263.

130. J. Huang, F. Kim, A.R. Tao, S. Connor, and P. Yang, *Spontaneous formation of nanoparticle stripe patterns through dewetting.* Nat Mater, 2005. **4**(12): p. 896-900.

131. E. Adachi, A.S. Dimitrov, and K. Nagayama, *Stripe Patterns Formed on a Glass Surface during Droplet Evaporation.* Langmuir, 1995. **11**(4): p. 1057-1060.

132. M. Islam, A. Ojha, C. Larimer, and I. Nettleship, *Antimycobacterial efficacy of silver nanoparticles as deposited on porous membrane filters.* Materials Science and Engineering: C, 2013.

133. G.M. Teitzel and M.R. Parsek, *Heavy Metal Resistance of Biofilm and Planktonic Pseudomonas aeruginosa.* Applied and Environmental Microbiology, 2003. **69**(4): p. 2313-2320.

134. H. Zhang, J.A. Smith, and V. Oyanedel-Craver, *The effect of natural water conditions on the anti-bacterial performance and stability of silver nanoparticles capped with different polymers.* Water Research, 2012. **46**(3): p. 691-699.

135. A.M. El Badawy, R.G. Silva, B. Morris, K.G. Scheckel, M.T. Suidan, and T.M. Tolaymat, *Surface Charge-Dependent Toxicity of Silver Nanoparticles.* Environmental Science & Technology, 2010. **45**(1): p. 283-287.

136. F. Widdel, *Theory and measurement of bacterial growth.* Di dalam Grundpraktikum Mikrobiologie, 2007. **4**.

137. R. Teng and T. Dick, *Isoniazid resistance of exponentially growing Mycobacterium smegmatis biofilm culture.* FEMS Microbiology Letters, 2003. **227**(2): p. 171-174.

138. M. Rawat, M. Uppal, G. Newton, M. Steffek, R.C. Fahey, and Y. Av-Gay, *Targeted Mutagenesis of the Mycobacterium smegmatis mca Gene, Encoding a Mycothiol-Dependent Detoxification Protein.* Journal of Bacteriology, 2004. **186**(18): p. 6050-6058.

139. R. Prasher, D. Song, J. Wang, and P. Phelan, *Measurements of nanofluid viscosity and its implications for thermal applications.* Applied Physics Letters, 2006. **89**(13): p. 133108-3.

140. N. Otsu, *A threshold selection method from gray-level histograms.* IEEE Transactions on Systems, Man and Cybernetics, 1979. **9**(1): p. 62-66.

141. G.W. Scherer, *Theory of Drying.* Journal of the American Ceramic Society, 1990. **73**(1): p. 3-14.

142. S. Whitaker, *Simultaneous Heat, Mass, and Momentum Transfer in Porous Media: A Theory of Drying*, in *Advances in heat transfer*, J.P. Hartnett and T.F. Irvine, Editors. 1977, Academic Press: New York. p. 119-203.

143. M.N. Rahaman, *Ceramic processing*. 2007: CRC/Taylor & Francis.

144. E.-U. Schlünder, *Drying of Porous Material During the Constant and the Falling Rate Period: A Critical Review of Existing Hypotheses.* Drying Technology: An International Journal, 2004. **22**(6): p. 1517 - 1532.

145. A. Belhamri, *Characterization of the First Falling Rate Period During Drying of a Porous Material.* Drying Technology: An International Journal, 2003. **21**(7): p. 1235 - 1252.

146. E.U. Schlünder, *On the mechanism of the constant drying rate period and its relevance to diffusion controlled catalytic gas phase reactions.* Chemical Engineering Science, 1988. **43**(10): p. 2685-2688.

147. S. Vafaei, T. Borca-Tasciuc, M.Z. Podowski, A. Purkayastha, G. Ramanath, and P.M. Ajayan, *Effect of nanoparticles on sessile droplet contact angle.* Nanotechnology, 2006. **17**(10): p. 2523.

148. H. Yabu and M. Shimomura, *Preparation of Self-Organized Mesoscale Polymer Patterns on a Solid Substrate: Continuous Pattern Formation from a Receding Meniscus.* Advanced Functional Materials, 2005. **15**(4): p. 575-581.

149. J. Huang, R. Fan, S. Connor, and P. Yang, *One-Step Patterning of Aligned Nanowire Arrays by Programmed Dip Coating.* Angewandte Chemie, 2007. **119**(14): p. 2466-2469.

150. R. Samel, R.W.V. Weaver, and D.B. Gammack, *Changes on storage in milk processed by ultra-high-temperature sterilization.* Journal of Dairy Research, 1971. **38**(03): p. 323-332.

151. B. Purevsuren and Y. Davaajav, *Investigation on Pyrolysis of Casein.* Journal of Thermal Analysis and Calorimetry, 2001. **66**(3): p. 743-748.

152. B. Purevsuren and Y. Davaajav, *Thermal Analysis of Casein.* Journal of Thermal Analysis and Calorimetry, 2001. **65**(1): p. 147-152.